AIAA Journal
Vol. 62, No. 10, October 2024

Analytical Linearization of Aerodynamic Loads in Unsteady Vortex-Lattice Method for Nonlinear Aeroelastic Applications

Christian Hente*
Leibniz University Hannover, 30167 Hannover, Germany
Bruno A. Roccia†
University of Bergen, 5007 Bergen, Norway
Raimund Rolfes‡
Leibniz University Hannover, 30167 Hannover, Germany
and
Cristian G. Gebhardt§
University of Bergen, 5007 Bergen, Norway

https://doi.org/10.2514/1.J063693

This paper presents the analytical linearization of aerodynamic loads (computed with the unsteady vortex-lattice method), which is formulated as tangent matrices with respect to the kinematic states of the aerodynamic grid. The loads and their linearization are then mapped to a nonlinear structural model by means of radial-basis functions, allowing for a two-way strong interaction scheme. The structural model comprises geometrically exact beams formulated in a director-based total Lagrangian description, circumventing the need for rotational degrees of freedom. The structural model is spatially discretized into finite elements and temporally discretized with the help of an implicit scheme that identically preserves momenta and energy. The resulting nonlinear discrete equations are solved by applying Newton's method, requiring calculating the Jacobians of the whole aeroelastic system. The correctness of the linearized loads is then shown by direct comparison with their numerical counterparts. In addition, we employ our strongly coupled aeroelastic model to investigate the nonlinear static and dynamic behavior of a suspension bridge. With this approach, we successfully investigate the numerical features of the aeroelastic system under divergence and flutter conditions.

I. Introduction

THERE is an ever-growing interest in characterizing the aerodynamic and aeroelastic behavior of highly flexible aeronautical/mechanical structures, undergoing large displacements/rotations in space and immersed in low-subsonic flows. The diversity of such systems is large, and to illustrate its enormous variety, we can mention some examples such as high-altitude long-endurance (HALE) aircraft involving unconventional configurations (joined wings and strut-braced wings) [1,2], helicopter rotors [3], high-aspect-ratio wings [4,5], horizontal- and vertical-axis wind turbines [6,7], and some constructions like suspension bridges [8,9]. As for those physical systems, the flow separation mainly occurs on highly flexible structural members, the aeroelastic behavior is untreatable through closed-analytic approaches. The involved intrinsic features make it necessary to describe them by a fully unsteady three-dimensional flow strongly coupled with the structure under consideration. Structural and flow solvers are the two main subdomains of any staggered (or partitioned) framework intended for aeroelastic simulations [10].

High-fidelity solvers, such as those based on computational fluid dynamics (CFD) techniques, have been successfully used and are possibly the best option from the point of view of accuracy. However, solving the full Navier–Stokes equations for three-dimensional unsteady flows with highly deformable boundaries remains challenging and time-consuming. An interesting alternative is the unsteady vortex-lattice method (UVLM), which has been gaining ground in the study of unsteady problems, in which free-wake methods become a necessity due to the geometric complexity of the systems under analysis [11–15]. Although this method has been implemented in different flavors, all its variants are based on the same theoretical principles, and, therefore, those codes with similar capabilities should show very good agreement [16]. Due to the excellent tradeoff between computational cost and accuracy, UVLM-based solvers have also been successfully integrated into aeroelastic simulation frameworks. In such an aeroelastic context, we can distinguish between two different approaches depending on the numerical time integration scheme selected to integrate the governing equations: explicit formulas or predictor–corrector schemes and implicit algorithms. The former group relies almost entirely on multistep predictor–corrector pairs such as Euler methods, Adams-Bashforth/Moulton methods, and Hamming's fourth-order predictor–corrector method. These procedures have been successfully implemented into UVLM-based aeroelastic frameworks to study a large number of engineering applications [17–22]. They are simple to implement and do not require any linearization of the equations of motion, but at the expenses of some restrictions and numerical issues. First, they are limited to structural models, where elastic displacements are small and disaggregated from rigid body motions [18,19,21,23]. Second, they do not preserve energy or momenta, so the solution may degrade over time. Third, predictor–corrector formulas are multistep methods requiring starting schemes, i.e., first-order formulas at t_1, second-order formulas at t_2, and so on until reaching the desired order of accuracy. Such a procedure severely compromises the order of accuracy of the solution, i.e., the order of the entire numerical scheme will be conditioned by the lowest-order formula present in the method [24].

As mechanical/aeronautical systems become increasingly complex, linear and standard multibody approaches (e.g., floating frames of reference or corotational formulations) are no longer suitable for treating highly flexible slender structures. Consequently, advanced

Received 27 October 2023; revision received 6 May 2024; accepted for publication 19 May 2024; published online Open Access 16 August 2024.

*Ph.D. Student, Institute of Structural Analysis—ForWind Hannover, Appelstraße 9A; c.hente@isd.uni-hannover.de.

†Postdoctoral Fellow, Geophysical Institute and Bergen Offshore Wind Centre (BOW), Allégaten 70; bruno.roccia@uib.no.

‡Full Professor, Institute of Structural Analysis–ForWind Hannover, Appelstraße 9A; r.rolfes@isd.uni-hannover.de.

§Full Professor, Geophysical Institute and Bergen Offshore Wind Centre (BOW), Allégaten 70; cristian.gebhardt@uib.no.

aeroelastic environments depend on more sophisticated structural models such as ANCFs [25,26], geometrically exact beam formulations [27,28], and their variants [29,30]. This is when using the second group of integration schemes, the implicit methods, becomes mandatory. These integrators generally have very good stability properties; some of them identically preserve energy as well as linear and angular momenta [31]. Essentially, when dealing with nonlinear systems, implicit schemes require gradient-based solution methods, which require *linearization* of the governing equations, i.e., linearizing the structural and aerodynamic equations. Although this is a standard procedure in computational mechanics, the linearization of the UVLM poses several challenges. Mauermann [32] developed a linearized form of the UVLM, focusing on obtaining a formulation based on aerodynamic states to study the dynamic behavior of aircraft under wake vortex encounters. Later, Murua et al. [33] introduced a linearized version of the UVLM, which is based on a frozen free-vortex sheet geometry. The linearization accounts for the velocity and spatial changes in the normal vector of bound-vortex surfaces, yet it assumes a fixed geometry when linearizing the aerodynamic loads and influence matrices of the discretized bounded geometry. Their work aimed to solve nonlinear aeroelastic problems through the formulation of a linear state-space UVLM. On this basis, Hesse et al. [34] and Hesse and Palacios [35] introduced a reduced-order aeroelastic strategy to study the dynamics of flexible aircraft, and Hilger and Ritter [36] developed a linearized aerodynamic model intended for monolithic-based aeroelastic state-space formulations. Lately, Maraniello and Palacios [37,38] developed a general linear UVLM-state-space framework along with a model-order reduction technique and a parametric reduced-order modeling for the UVLM. Although both works are based on [33], they considered a more general linearization process where the change in the bounded-vortex geometry is considered fully, but the assumption of a frozen wake is still retained. Regarding the aerodynamic loads, their linearizations are computed from a combination of the Joukowski method (steady component) and the unsteady Bernoulli equation (unsteady component). To some extent, Stanford and Beran [11] resemble a linearization procedure to perform sensitivity analyses within a UVLM-optimization approach for maximizing the propulsive efficiency of flapping wings under lift and thrust constraints.

Despite all these relevant works and efforts made in the context of linearization, reduced-order models, and linear state-space formulations of the UVLM, to the best of our knowledge, there is no contribution regarding a linearization methodology intended for a general nonlinear aeroelastic framework based on UVLM flow solvers. Our methodology differs from those already published in several aspects: i) the solution procedure for the nonlinear aeroelastic equations, ii) the time integration method, iii) the linearized aerodynamic loads, iv) the aeroelastic approach, and v) the structural mechanical model. We solve the nonlinear equations directly using an implicit integration scheme based on discrete-time derivatives, specifically the "average vector field" method, and employing the gradient-based Newton method within a strong coupled fluid–structure interaction. In this sense, our approach improves the accuracy, numerical convergence, and global robustness for investigating highly nonlinear aeroelastic scenarios, especially those characterized by highly nonlinear geometric effects (e.g., large displacements, large rotations, large velocity gradients). The integration scheme adopted in this work naturally ensures the preservation of physically important features, such as the linear and angular momenta and the total energy. Here, we propose a procedure to take into account the contribution of the surrounding flow to the tangent matrices by performing a full linearization of the unsteady Bernoulli equation with respect to generalized structural coordinates and velocities. Like Maraniello and Palacios [37,38], our approach generally assumes a frozen wake. However, using Newton's method to solve the nonlinear aeroelastic governing equations necessitates an additive update of the bounded-vortex geometry during each iteration step. This alteration in geometry yields a gap between the bounded-vortex geometry and the frozen wake, which can lead to nondesired numerical effects influencing the convergence behavior negatively. To improve the physical free-wake representation and mitigate these numerical effects, we update the connection between the bounded geometry and the wakes at the separation zones during each iteration. Consequently, a linearization of these wake segments with respect to the displaced separation edge is required. While most of the works reported in the literature combine the aerodynamic and structural models monolithically, our aeroelastic approach is based on a strong bidirectional fluid–structure interaction derived with respect to the structural model's state variables (generalized coordinates and generalized velocities). In this way, our approach provides high versatility when coupling an aerodynamic model with our structural model. Furthermore, the resulting system's Jacobian provides reliable information on the behavior of aeroelastic stability and can be used to predict, to a good extent, flutter and/or divergence velocities without conducting full aeroelastic simulations.

The objective of our work and the final results constitute a first attempt to consistently integrate the UVLM into a nonlinear aeroelastic framework ruled by an implicit integrator based on discrete-time derivatives. Although there are more works addressing aeroelastic studies based on implicit integration schemes where the contributions to the tangent matrices coming from the UVLM are neglected [39,40], it is not clear how such simplification affects the results, the robustness of the simulation framework, and/or the convergence properties of the integrator. In this sense, our work aims to shed some light on this issue by providing a systematic way of including the contribution of the UVLM during the linearization of the equations of motion, thus allowing us to evaluate some of the inherent effects of neglecting such contributions. To the best of our knowledge, such a development has not appeared in the existing literature yet.

The remainder of this work is organized as follows: In Sec. II, we present detailed aspects of the modeling process behind the UVLM. In addition, we fully describe a procedure to analytically linearize the aerodynamic loads obtained using a standard UVLM-based flow solver. We briefly review the nonlinear aeroelastic framework, including general aspects of the nonlinear structural model in Sec. III. In Sec. IV, we present showcases intended for verifying our approach for the analytical computation of tangent matrices associated with the UVLM. Finally, concluding remarks are collected in Sec. V to close the paper.

II. Aerodynamic Model

A. General Aspects

Let us consider a body $\mathcal{B}$ immersed in a low-subsonic flow. When the Reynolds number Re is sufficiently large, the viscous effects can be confined to those regions close to the solid surfaces; these vorticity-dominated regions are called boundary layers. Part of the vorticity contained in the boundary layers is shed downstream into the flowfield, where it can only be transported by the fluid particles but can neither be created nor destroyed. This transported vorticity forms the wakes behind the body. The thickness of the boundary layers and wakes tends to zero as the $Re \rightarrow \infty$. Thus, the boundary layers and wakes are continuous bound and free vorticity sheets. The absolute velocity of a fluid particle, which occupies the position $\boldsymbol{r}$ at instant t, is denoted by $\boldsymbol{V}(\boldsymbol{r}, t)$. The fluid surrounding $\mathcal{B}$ is assumed to be inviscid and irrotational over the entire flowfield, excluding the body's solid boundaries and its wakes. Under these assumptions, the unknown velocity, pressure, and density fields are governed by the well-known Euler equation [41].

Because of the low-subsonic flow condition, the Mach number is lower than 0.3; thus, the flow is considered incompressible. Such a condition allows us to add an extra pure kinematical relationship, which states that the velocity field is divergence-free. Such a relation is known as the *continuity equation for incompressible flows*, $\nabla \cdot \boldsymbol{V}(\boldsymbol{r}, t) = 0$. This equation gives rise to much simplification in the equations of fluid mechanics. Such an incompressibility assumption reduces the thermomechanical problem of the motion of an inviscid fluid to a purely mechanical problem [42]. In addition, the velocity field can be expressed by using Helmholtz's decomposition as the superposition of a contribution coming from a scalar potential $\varphi(\boldsymbol{r}, t)$ and another contribution from a vector potential $\boldsymbol{\Psi}(\boldsymbol{r}, t)$ [43]:

$$V(r,t) = \nabla\varphi(r,t) + \nabla\times\Psi(r,t) = V_\varphi(r,t) + V_\psi(r,t) \tag{1}$$

where the scalar potential component of the velocity is irrotational, and the vector potential component captures any vorticity effect. Introducing the velocity relationship Eq. (1) into the continuity equation allows us to obtain the following partial differential (PDE):

$$\nabla\cdot V(r,t) = \nabla\cdot\nabla\varphi(r,t) + \nabla\cdot(\nabla\times\Psi(r,t)) = \nabla^2\varphi(r,t) = 0 \tag{2}$$

which is the well-known Laplace equation for the scalar potential. Furthermore, the continuity equation, known from gauge theory as the Coulomb gauge condition [44], implies that the solenoidal field $V(r,t)$ can also be written as the curl of another vector potential $\Psi_1(r,t)$, that is to say,

$$V(r,t) = \nabla\times\Psi_1(r,t) = \nabla\varphi(r,t) + \nabla\times\Psi(r,t) \tag{3}$$

which shows that $\nabla\varphi(r,t) = \nabla\times[\Psi_1(r,t) - \Psi(r,t)] = \nabla\times\Psi_2(r,t)$. Such a relation allows us to determine the velocity field associated with $\nabla\varphi$ by solving either PDE Eq. (2) or the following equivalent Poisson's equation:

$$\begin{aligned}\nabla\times[\nabla\times\Psi_2(r,t)] &= \nabla(\nabla\cdot\Psi_2(r,t)) - \nabla^2\Psi_2(r,t)\\ &= \mathbf{0}, \text{then, } \nabla^2\Psi_2(r,t) = q(r,t)\end{aligned} \tag{4}$$

provided $q(r,t) = \nabla(\nabla\cdot\Psi_2(r,t))$ is known and then considered as a source term. On the other hand, by introducing Eq. (1) into the definition of the vorticity field $\Omega(r,t) = \nabla\times V(r,t)$ and stipulating that $\nabla\cdot\Psi(r,t) = 0$, we obtain the following PDE:

$$\nabla^2\Psi(r,t) = -\Omega(r,t) \tag{5}$$

which is a vector Poisson equation relating the vector potential to the vorticity. In addition, the velocity field in Eq. (1) can also be thought of as composed of three components: i) the freestream velocity, V_∞; ii) the velocity associated with the continuous bound-vortex sheets, $V_B(r,t)$; and iii) the velocity associated with the free-vortex sheets (or wakes) being shed from the sharp edges (separation zones, SZs) of $\mathcal{B}$, $V_W(r,t)$. Without loss of generality, in this work, we assume that the field V_B and the freestream component are absorbed by $\nabla\varphi$ while the field V_W is identified with $\nabla\times\Psi$. That is,

$$\nabla\varphi(r,t) = \nabla\varphi_1(r,t) + \nabla\varphi_2(r,t) = V_B + V_\infty, \text{ and, } \nabla\times\Psi(r,t) = V_W \tag{6}$$

Although Eqs. (1) and (2) do not directly include time-dependent terms, they can be introduced through the boundary conditions, e.g., the nonpenetration or permeability condition.

1. Boundary Conditions

The governing equations of the problem are completed with the following boundary conditions (BCs):

1) **Regularity at infinity:** This condition requires the velocity field associated with the flow disturbance, due to the motion of $\mathcal{B}$ through the fluid, to decay away from the body and its wakes. Mathematically, it is expressed as follows:

$$\lim_{\|r-r_B\|\to\infty} \|V_B(r,t) + V_W(r,t)\| = 0 \tag{7}$$

where $\|r - r_B\|$ is the distance between a point belonging to the body and an arbitrary point r.

2) **Nonpenetration condition:** It requires that, over the entire surface of $\mathcal{B}$, the normal component of the fluid velocity relative to the body's surface must be zero:

$$[V_\infty + V_B(r,t) + V_W(r,t) - V_S(r,t)]\cdot\hat{n} = 0 \tag{8}$$

where $V_S(r,t)$ is the velocity of the body (also called solid velocity), and $\hat{n}$ is a unitary normal vector to the boundary of $\mathcal{B}$. Next, Eq. (8) can be restated as

$$V_B(r,t)\cdot\hat{n} = [V_S(r,t) - V_W(r,t) - V_\infty]\cdot\hat{n} \tag{9}$$

Since V_∞ is the velocity of an incompressible flow, it satisfies $\nabla\cdot V_\infty = 0$, and by construction, V_W does too. As mentioned above, $V_B = \nabla\varphi_1$ and, finally, Eq. (8) takes the following form:

$$\nabla\varphi_1(r,t)\cdot\hat{n} = \frac{\partial\varphi_1}{\partial\hat{n}} = [V_S(r,t) - V_W(r,t) - V_\infty]\cdot\hat{n}, \quad \text{for } r\in\partial\mathcal{B} \tag{10}$$

which is known as a second-type or Neumann boundary condition.

In addition to the aforementioned boundary conditions, for unsteady flows, it is also required the Kelvin condition to be satisfied. In general, the Kelvin condition states that "In the potential flow region the angular momentum cannot change, and thus the circulation Γ around a closed curve remains constant for all times, i.e., $D\Gamma/Dt = 0\ \forall\ t$."

Another important condition to be imposed is the so-called Kutta's condition. The reader should be aware that it can be explicitly enforced, as reported by Lee [45]. However, for highly three-dimensional flows and/or unsteady flows characterized by highly reduced frequencies (e.g., rotors and flapping wings, among others), the classical steady Kutta condition may lead to a nonzero pressure jump at the separation zones [46]. In this regard, many approaches have been proposed over time to tackle down this problem. Among the most important ones, we can mention imposing the same speed on the upper and lower surfaces at the separation zones but with opposite tangential direction [47], imposing a jump velocity between the upper and lower surfaces at the SZ equal to the shed vorticity [48], imposing an infinite velocity jump at the SZ [49], and limiting the velocity at the separation zones to fix the rear stagnation point (i.e., $V < \infty$) [50]. Based on a large number of previous works [13,14,18,22,51,52], here we enforce the Kutta condition by requiring the pressures to be finite and the pressure jump to be zero along the separation edges. This forces the flow to leave the SZs smoothly, but with vorticity in general. In other words, the fluid particles located on the sharp edges where separation takes place are required to "move" away from $\mathcal{B}$ at the local velocity flow, the well-known *vorticity shedding* phenomenon (or wake convection).

2. Vortex Sheets

In nonuniform motions, the wake becomes more complex than in steady flows, and therefore, it needs to be properly accounted for [41]. In addition, it should be stressed that the integral representation of the velocity field in terms of the vorticity field is obtained by solving the Poisson PDE Eq. (5). The resulting expression for V is the well-known Biot–Savart (B-S) law. For three-dimensional flows, it takes the following form:

$$V(r,t) = \frac{\Gamma}{4\pi}\int_{\mathcal{C}(s,t)} \frac{\hat{T}(s,t)\times(r - r_0(s))}{\|r - r_0(s)\|_2^3}\,\mathrm{d}s(t) \tag{11}$$

where r_0 is a position vector of a point belonging to a curve $\mathcal{C}$, Γ is the circulation (or strength) around $\mathcal{C}$, $\hat{T}$ is the unit tangent vector to $\mathcal{C}$, and s is the arc-length coordinate along the curve. Vortex sheets and vortex lines (or filaments) of concentrated vorticity are not physically possible entities. However, they represent suitable analytical approximations when vorticity is confined to narrow spatial regions.

3. Wake Convection

Over time, more fluid particles are convected from the sharp edges of $\mathcal{B}$ into the wakes, which in turn can deform into force-free configurations. The vorticity in the near wake can substantially affect the flowfield surrounding $\mathcal{B}$, the vorticity distribution on $\partial\mathcal{B}$, and, therefore, the loads on the body. Because the wake at the present time was generated on, and shed from, the body at an earlier time, the flowfield is said to be *history-dependent*, i.e., the history of the motion is stored in the wake. As time passes and the wake moves far downstream, its influence on the flow around the body decreases; such an assertion is equivalent to saying that the *wake has a fading memory.* It should be noted that the vorticity distribution and the shape of the wakes are obtained as part of the problem's solution.

After an infinitesimal period of time, the shape of the wakes will be different, and new fluid particles will be convected from the SZs into the wakes. Then, the position of each fluid particle, $\boldsymbol{r}_F$, at an arbitrary time t can be determined based on the local velocity of the fluid using the following integral:

$$\boldsymbol{r}_F(t) = \int_0^t \boldsymbol{V}(\boldsymbol{r}_F(\tau), \tau)\,\mathrm{d}\tau, \quad \text{where,}$$
$$\boldsymbol{V}(\boldsymbol{r}_F, t) = \boldsymbol{V}_B(\boldsymbol{r}_F, t) + \boldsymbol{V}_W(\boldsymbol{r}_F, t) + \boldsymbol{V}_\infty \tag{12}$$

4. Aerodynamic Loads

On this topic, two approaches can be followed to compute the aerodynamic loads on lifting surfaces embedded in vorticity-dominated flows. One of them, widely used in classical aircraft/rotor applications, relies on the computation of the pressure jump across airfoils using the well-known unsteady Bernoulli equation [51], hereafter called the *Bernoulli method* (BM). The second approach is based on the vector form of the Kutta–Joukowski lift theorem [41]. It should be stressed that both the BM and Joukowski methods yield very good estimations of the lift coefficient. However, contrary to Joukowski, BM-like approaches do not take into account the leading-edge suction effect, which results in an overestimation of the induced drag.

Recalling that $\nabla \times \boldsymbol{V} = \boldsymbol{0}$ outside the boundary layers of $\mathcal{B}$ and its wakes and assuming irrotational body forces, Euler's equation can be integrated along a streamline once and for all, thus resulting in the Bernoulli equation for unsteady flows:

$$\int_{C(s)} \partial_t(\nabla \times \boldsymbol{\Psi}) \cdot \hat{\boldsymbol{T}}(s)\,\mathrm{d}s + \partial_t\varphi + \frac{1}{2}[\nabla\varphi + \nabla \times \boldsymbol{\Psi}] \cdot [\nabla\varphi + \nabla \times \boldsymbol{\Psi}] + \frac{1}{\rho_F} p(\boldsymbol{r}, t) = E(t) \tag{13}$$

where $E(t)$ is a spatially uniform function of time. Integrating Eq. (13) along a streamline from a point P_x on the surface of $\mathcal{B}$ to a far-field reference point ∞, i.e., as $\|\boldsymbol{r}\| \to \infty$, $\varphi \to \varphi_\infty =$ constant, $p = p_\infty =$ constant, $\nabla \times \boldsymbol{\Psi} \to \boldsymbol{0}$, and $\nabla\varphi \to \boldsymbol{V}_\infty$, the freestream velocity. Therefore, $E(t) \to (1/2)\boldsymbol{V}_\infty \cdot \boldsymbol{V}_\infty + (p_\infty/\rho_F)$, and Eq. (13) is rewritten as follows:

$$\frac{p_\infty - p(\boldsymbol{r}, t)}{\rho_F} = \int_\infty^{P_x} \partial_t(\nabla \times \boldsymbol{\Psi}) \cdot \hat{\boldsymbol{T}}(s)\,\mathrm{d}s + \partial_t\varphi|_{P_x} + \frac{1}{2}[\nabla\varphi + \nabla \times \boldsymbol{\Psi}] \cdot [\nabla\varphi + \nabla \times \boldsymbol{\Psi}]|_{P_x} - \boldsymbol{V}_\infty \cdot \boldsymbol{V}_\infty \tag{14}$$

Then, the pressure jump across the lifting surface at a point is defined as the difference between the pressure below the vortex sheet (point L) and the pressure above the vortex sheet (point U), i.e., $Dp = (p)_L - (p)_U$. After some algebraic manipulations, Dp is given by

$$\frac{Dp}{\rho_F} = \int_L^U \partial_t(\nabla \times \boldsymbol{\Psi}) \cdot \hat{\boldsymbol{T}}(s)\,\mathrm{d}s + [\partial_t\varphi|_U - \partial_t\varphi|_L] + \frac{1}{2}[\nabla\varphi + \nabla \times \boldsymbol{\Psi}] \cdot [\nabla\varphi + \nabla \times \boldsymbol{\Psi}]|_U - \frac{1}{2}[\nabla\varphi + \nabla \times \boldsymbol{\Psi}] \cdot [\nabla\varphi + \nabla \times \boldsymbol{\Psi}]|_L \tag{15}$$

On the other hand, Joukowski's method requires splitting the force vector into two parts: a quasi-steady $\boldsymbol{F}^s$ and an unsteady component $\boldsymbol{F}^u$. The steady and unsteady contribution of a differential vortex filament $d\beta$ of circulation $\Gamma(t)$ is computed from the Kutta–Joukowski theorem [53] as

$$\boldsymbol{F}^s = \rho_F \Gamma(t)[\boldsymbol{V}(\boldsymbol{r}, t) \times \hat{\boldsymbol{T}}(s)ds] \quad \text{and}$$
$$\boldsymbol{F}^u = \rho_F c d_t \Gamma(t)[\hat{\boldsymbol{V}}(\boldsymbol{r}, t) \times \hat{\boldsymbol{T}}(s)ds] \tag{16}$$

where $d_t(\cdot)$ stands for total derivative with respect to time, $\boldsymbol{V}(\boldsymbol{r}, t)$ is the local flow velocity evaluated at the center of the vortex filament, $\hat{\boldsymbol{V}}(\boldsymbol{r}, t) = \boldsymbol{V}(\boldsymbol{r}, t)/\|\boldsymbol{V}(\boldsymbol{r}, t)\|$ is a unit vector along the direction of the local flow velocity, c is the airfoil chord, and, as before, $\hat{\boldsymbol{T}}(s)$ and s are the unit tangent vector and arc-length coordinate along the vortex filament.

Although we have introduced two different approaches to compute aerodynamic loads, the sections dedicated to calculating aerodynamic loads on a discrete setting and their linearization will only deal with the method based on the unsteady Bernoulli equation.

B. Unsteady Vortex-Lattice Method

In the nonlinear UVLM, originally developed by researchers at Virginia Tech [51,54,55] and at Israel Institute of Technology [41,50,56], the continuous bound-vortex sheets representing the boundary layers are discretized into a lattice of short straight-vortex segments of circulation $\Gamma(t)$. These segments divide the surface of $\mathcal{B}$ into a finite number of area elements (or panels), hereafter denoted by B_k. The model is completed by joining free vortex lines, representing the wakes, to the bound-vortex lattice along the sharp edges where the separation phenomenon occurs, such as trailing edges, wing or blade tips, and leading edges (LEs) eventually. Whereas the locations where separation occurs are considered user-input data, the distribution and position of vorticity in all free-force wakes are determined as part of the solution. In Fig. 1, we present an example of a mesh for the bound-vortex and free-vortex lattices for an extremely (X) high-altitude long-endurance (HALE) unmanned air vehicle (UAV). An aerodynamic grid $\mathcal{A}_i$ representing the lifting and nonlifting surfaces associated with a body i is a geometric decomposition of its boundary, $\partial\mathcal{B}_i$, into a finite set of cells (area elements, panels, or boundary elements) $\mathcal{A}_i = \{B_k^i\}$, such that, $\mathcal{A} = \bigcup_{i=1}^{N_B} \mathcal{A}_i$ and $\mathcal{A}_i = \bigcup_{k=1}^{N_{pb_i}} B_k^i$,

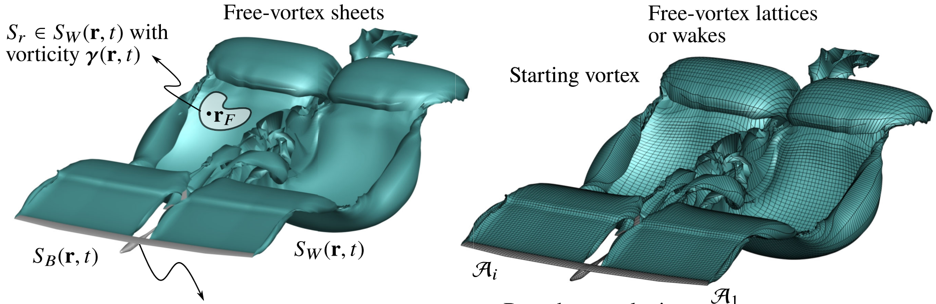

Fig. 1 Schematic representation of a bound- and free-vortex sheets/lattices.

where N_B is the number of bodies, and N_{pb_i} is the cardinality of $\mathcal{A}_i$, i.e., $\mathrm{card}(\mathcal{A}_i) = N_{pb_i}$. Then, the total number of panels used to discretize the whole surface of $\mathcal{B}$ is determined as $N_{pb} = \sum_{i=1}^{N_B} N_{pb_i}$. In addition, each pair of cells belonging to the ith grid must meet the following conditions:

1) If $B_k^i \cap B_j^i$ for $k \neq j$ is exactly one point, then it is a common vertex (node) of B_k^i and B_j^i.

2) If $B_k^i \cap B_j^i$ for $k \neq j$ is not exactly one point, then it is a common facet of B_k^i and B_j^i (edge in two dimensions).

Although quadrilateral elements (QE) are commonly used in VLM implementations [41], the use of triangles (TE) and combinations of QE and TE is spreading due to the versatility and potentiality provided by FEM meshers to generate geometric decompositions of very complex domains [15]. These area elements are used to impose the nonpenetration condition on their geometric centers (the so-called control or collocation points, CPs). It should be mentioned that here, nonlifting surfaces are only considered to set a constraint on the flowfield by means of the nonpenetration condition. In this regard, the extra distribution of vorticity on the nonlifting bodies will prevent the flow from penetrating the solid boundaries and, therefore, follow a path tangential to them. Furthermore, when nonlifting surfaces are closed bodies, it is important to note that having as many vortex rings as surface elements constitutes an ill-conditioned problem. Such an issue can be easily repaired either by removing at least one vortex ring or by using other boundary elements (see [41]).

As mentioned above, the edges of these boundary elements are represented by straight, finite vortex segments of circulation $\Gamma(t)$, whose contribution to the velocity field is computed through a discrete version of Eq. (11):

$$
\begin{aligned}
\boldsymbol{V}^d(\boldsymbol{r},t) &= \frac{\Gamma(t)}{4\pi}\frac{(\boldsymbol{r}_1\times\boldsymbol{r}_2)(\|\boldsymbol{r}_1\|+\|\boldsymbol{r}_2\|)}{\|\boldsymbol{r}_1\|\|\boldsymbol{r}_2\|(\|\boldsymbol{r}_1\|\|\boldsymbol{r}_2\|+\boldsymbol{r}_1\cdot\boldsymbol{r}_2)+(\delta_c\|\boldsymbol{u}\|)^2}\\
&= \frac{\Gamma(t)}{4\pi}\overline{B-S}(\boldsymbol{r}_1,\boldsymbol{r}_2)
\end{aligned}
\tag{17}
$$

where $\boldsymbol{r}_1$ and $\boldsymbol{r}_2$ are the position vectors of the point where the velocity is being evaluated relative to the ends of the straight vortex segment, $\boldsymbol{u} = \boldsymbol{r}_1 - \boldsymbol{r}_2$, and δ_c is a cutoff parameter, which is introduced to remove the singular kernel of Eq. (11). Although introducing the term $(\delta_c\|\cdot\|)$ into Eq. (17) is interpreted as essentially an ad hoc technique [57,58], it has been proven to work satisfactorily well in practice. According to Grasso et al. [59], some guides to select the δ_c-parameter are from 1 to 10% for wake roll-up computations and 0.01% for bound-vortex calculations. From now on, superscript d will represent a discretized scalar/vector field.

According to the theoretical description presented in Sec. II.A, it is clear that we have two PDEs associated with our problem: i) the Laplace equation together with Neumann BCs for the scalar potential $\varphi(\boldsymbol{r},t)$, and ii) Poisson's equation for the vector potential $\boldsymbol{\Psi}(\boldsymbol{r},t)$. However, most UVLM implementations consider the Laplace BVP, but they use the B-S law together with the Neumann BC for computing velocities and solving for the circulations on the lifting and nonlifting surfaces. To this end, the nonpenetration condition leads to a linear algebraic system regarding the unknown vortex circulations on the discretized surfaces of $\mathcal{B}$. Such an approach, where we avoid solving Laplace's equation and use Poisson's solution instead, is only possible at the discrete level due to the equivalence between doublets (or dipoles) and vortex loops of constant circulations [41,60].

1. Aerodynamic Influence Coefficients

The specification of the nonpenetration condition at each CP of $\mathcal{A}$ results in a linear system of algebraic equations (generally with time-varying coefficients). The unknowns are the circulations around the individual bound vortex segments; however, the linear system can be rewritten in terms of vortex ring circulations $G_j(t)$, which substantially reduces the size of the problem [51]. Such vortex rings are obtained by considering each panel to be enclosed by a closed loop of vortex segments having the same circulation. Hence, each straight segment is formed from two loops. Under these assumptions, the fore-introduced linear system takes the following form:

$$
\begin{aligned}
\boldsymbol{A}(t)\boldsymbol{G}(t)-\mathbf{RHS}(t) = \sum_{j=1}^{N_{pb}} a_{ij}(t)G_j(t) + [\boldsymbol{V}_\infty^d + \boldsymbol{V}_W^d(\boldsymbol{r}_i,t) - \boldsymbol{V}_S^d(\boldsymbol{r}_i,t)]\\
\cdot\hat{\boldsymbol{n}}_i(t) = 0, \quad i = 1,2,\ldots,N_{pb}
\end{aligned}
\tag{18}
$$

where $a_{ij}(t)$ are the aerodynamic influence coefficients, $\hat{\boldsymbol{n}}_i$ is the unit vector normal at the ith control point, $\boldsymbol{A}(t)\in\mathbb{R}^{N_{pb}\times N_{pb}}$ is the aerodynamic influence matrix, $\boldsymbol{G}(t)\in\mathbb{R}^{N_{pb}\times 1}$, and $\mathbf{RHS}(t)\in\mathbb{R}^{N_{pb}\times 1}$ is the right-hand side, which collects the contributions of the wake, freestream, and body velocities along the normal direction at each CP. It should be stressed that the aerodynamic coefficient $a_{ij}(t)$ represents the normal velocity component at the control point of the ith element associated with a vortex ring around the jth element having unit circulation.

Because mechanical/aeronautical systems are generally modeled as a collection of flexible and rigid bodies, the aerodynamic influence matrix can be split into different submatrices according to the following: i) the influence between panels belonging to the same aerodynamic grid $\mathcal{A}_p$, and ii) the influence between panels belonging to different aerodynamic grids, e.g., $\mathcal{A}_p$ and $\mathcal{A}_q$. Each aerodynamic coefficient in Eq. (18) can then be calculated by means of the function $In(B_i^p, B_j^q): \mathcal{A}_p\times\mathcal{A}_q\to\mathbb{R}$ for $p,q = 1,\ldots,N_b$,

$$
In(B_i^p,B_j^q) = \left[\frac{1}{4\pi}\sum_{k=1}^{4}\overline{B-S}\Big(\boldsymbol{r}_{1,k}^j,\boldsymbol{r}_{2,k}^j\Big)\right]\cdot\hat{\boldsymbol{n}}_i = \boldsymbol{In}(B_i^p,B_j^q)\cdot\hat{\boldsymbol{n}}_i
\tag{19}
$$

where $\boldsymbol{In}(B_i^p,B_j^q): \mathcal{A}_p\times\mathcal{A}_q\to\mathbb{R}^3$, and $\boldsymbol{r}_{1,k}^j$ and $\boldsymbol{r}_{2,k}^j$ are the position vectors of the control point of the ith panel $B_i^p\in\mathcal{A}_p$, where the velocity is being evaluated relative to the ends of the kth straight vortex segment $\boldsymbol{u}_k^j = \boldsymbol{r}_{1,k}^j - \boldsymbol{r}_{2,k}^j$ belonging to the jth panel $B_j^q\in\mathcal{A}_q$. It should be noted that generally $In(B_i^p,B_j^q)\neq In(B_j^q,B_i^p)$ for $p,q = 1,\ldots,N_B$. Consequently, the matrix $\boldsymbol{A}(t)$ is nonsymmetric. Additionally, empirical evidence suggests that such a matrix may lose its strictly diagonal dominant feature due to large motions/deformations that could lead to large off-diagonal values. In other words, panels that were relatively far apart in the initial configuration can become significantly closer together after large motions/deformations. In this regard, the linear algebraic system of equations (18) can be solved by using any direct method such as $\boldsymbol{LU}$ decomposition, Cholesky decomposition, or Gauss elimination. Iterative procedures like Jacobi and Gauss–Seidel (G-S) require, on the other hand, that certain conditions be satisfied on $\boldsymbol{A}(t)$ or their associated iterative matrices, $\boldsymbol{M}_J$ or $\boldsymbol{M}_{G-S}$. A sufficient condition for Jacobi and G-S to converge to a unique solution is that $\boldsymbol{A}(t)$ is strictly diagonally dominant. Unfortunately, as mentioned above, the matrix $\boldsymbol{A}(t)$ can lose this property due to large deformation of the lifting surfaces, and therefore this criterion can no longer be used. Another option is to check if the iterative matrices $\boldsymbol{M}_J$ or $\boldsymbol{M}_{G-S}$ are convergent (a necessary and sufficient condition), i.e., the spectral radius $\rho_s(\boldsymbol{M}) < 1$ or $\|\boldsymbol{M}\| < 1$ for any natural matrix norm. Due to the nature of the matrix $\boldsymbol{A}(t)$, there is no general result so far that allows the use of iterative methods for solving the linear system in UVLM-based implementations; therefore, this condition must be verified each time this matrix is updated. After solving the linear algebraic system for the unknown ring circulations $G_j(t)$, we can compute the velocity induced by all the bound-vortex lattices $\mathcal{A}j$ on an arbitrary point $\boldsymbol{r}_i$ as follows:

$$
\boldsymbol{V}_B^d(\boldsymbol{r}_i,t) = \sum_{j=1}^{N_{pb}}\frac{G_j(t)}{4\pi}\sum_{k=1}^{4}\overline{B-S}(\boldsymbol{r}_{1,k}^j,\boldsymbol{r}_{2,k}^j) = \sum_{j=1}^{N_{pb}} G_j(t)\boldsymbol{In}(\boldsymbol{r}_i,B_j)
\tag{20}
$$

2. Free-Vortex Lattice Convection

Let $\mathcal{V}_i$ for $i = 1, \ldots, N_W$ also be a set of cells $\mathcal{V}_i = \{L_k^i\}$ representing the wake shed from the sharp edges of $\mathcal{A}_j \in \mathcal{A}$, such that $\mathcal{V} = \bigcup_{i=1}^{N_W} \mathcal{V}_i$ and $\mathcal{V}_i = \bigcup_{k=1}^{N_{pw_i}(t)} L_k^i$, where $N_W \leq N_B$ is the number of lifting surfaces, and $N_{pw_i}(t) = \mathrm{card}(\mathcal{V}_i)$ is the cardinality of $\mathcal{V}_i$. Then, the total number of free-vortex rings at time t is determined as $N_{pw}(t) = \sum_{i=1}^{N_W} N_{pw_i}(t)$. It should be noted that the cardinality of each "wake set" increases with time at a constant rate, indicating in turn that the number of vortex rings in the free-vortex lattices increases with each time step (the shedding process). Once the circulations $G_j(t)$ are calculated, the wakes are convected to their new positions, and new vortex segments shed from the SZs are propagated into the free-vortex lattices. According to Sec. II.A.3, the spatial evolution of the corners of a vortex segment belonging to L_k^i is computed by evaluating the integral Eq. (12) at the local fluid velocity. For this purpose, the integral Eq. (12) is rewritten as a system of uncoupled ordinary differential equations (ODEs):

$$\left.\frac{d\boldsymbol{r}(t)}{dt}\right|_{\text{node}} = \boldsymbol{V}_{\text{node}}^d(t), \qquad \text{node} = 1, \ldots, N_{nw}(t) \tag{21}$$

where the subscript "node" was introduced to refer to the corners of a vortex segment, $N_{nw}(t)$ is the number of aerodynamic nodes in $\mathcal{V}$, and $\boldsymbol{V}_{\text{node}}^d(t) = \boldsymbol{V}_B^d(\boldsymbol{r}_{\text{node}}, t) + \boldsymbol{V}_W^d(\boldsymbol{r}_{\text{node}}, t) + \boldsymbol{V}_\infty^d$. The vector $\boldsymbol{V}_{\text{node}}^d(t)$ collects the contributions from all surface vortex rings B_k^i, all free-vortex rings L_j^i, and the freestream velocity. Because all the quantities involved in Eq. (21) are functions of time, the question of which instantaneous quantities to use in the approximation is raised. There are several options; for example, one can use the quantities that were calculated at the previous time step, the present time step, or their averaged values for the two-time steps. In all cases except the first, iterations are needed, which increase the computational cost. Kandil et al. [61] showed that explicit one-step methods are stable, and there are few differences in the computed results when compared with higher-order procedures. In this respect, here we use an explicit first-order method to propagate the wake:

$$\boldsymbol{r}_{\text{node}}(t + \Delta t) \approx \boldsymbol{r}_{\text{node}}(t) + \boldsymbol{V}_{\text{node}}^d(t)\Delta t \tag{22}$$

where Δt is the time step. From a computational point of view, the convection of the wakes is the most expensive step in any UVLM-based code implementation. Specifically, the velocity $\boldsymbol{V}_W^d$ at each L_k^i node is obtained by adding the contributions of each element in $\mathcal{V}$. As a consequence, the number of operations performed by the B-S law during the wake convection is $O(N_{pw}(t)^2)$. In this regard, we can say that the $O(N^2)$ nature of the problem and the time-dependent cardinality of $\mathcal{V}$ are directly responsible for the wake convection becoming a very time-consuming step.

3. Aerodynamic Loads (Discretization)

Here, we present the discrete version of Eq. (15) and how its different terms are handled to be computed in a simple way. For a detailed explanation of Joukowski's approach, the reader is referred to [62].

First, we recall that the pressure jump given by Eq. (15) is expressed in terms of a scalar potential $\varphi^d(\boldsymbol{r}, t)$ and the vector potential $\boldsymbol{\Psi}^d(\boldsymbol{r}, t)$. Without loss of generality, we have assumed that the velocity field is mainly split into two parts: $\boldsymbol{V}_B^d + \boldsymbol{V}_\infty^d$ associated with $\nabla\varphi^d$, and $\boldsymbol{V}_W^d$ associated with $\nabla \times \boldsymbol{\Psi}^d$. However, the unsteady term due to the vector potential $\int \partial_t(\nabla \times \boldsymbol{\Psi}^d) \cdot \hat{\boldsymbol{T}}(s)\, \mathrm{d}s$ is extremely difficult to handle in this form. By invoking the equivalence between a doublet and a vortex ring of constant circulation, we can consider the contribution of the free-vortex lattice as an analogous contribution of a discrete distribution of doublets (or dipoles) [63], then,

$$\begin{aligned}\int_L^U \partial_t(\nabla \times \boldsymbol{\Psi}^d) \cdot \hat{\boldsymbol{T}}(s)\, \mathrm{d}s &= \int_L^U \partial_t[\nabla\psi^d(\boldsymbol{r}(s), t)]|_{\text{wake}} \cdot \hat{\boldsymbol{T}}(s)\, \mathrm{d}s \\ &= \partial_t \int_L^U \nabla\psi^d(\boldsymbol{r}(s), t)|_{\text{wake}} \cdot \mathrm{d}\boldsymbol{r}(s) \\ &= \partial_t\psi^d(\boldsymbol{r}, t)|_U - \partial_t\psi^d(\boldsymbol{r}, t)|_L \end{aligned} \tag{23}$$

where $\nabla\psi^d$ is a discrete scalar potential and $\nabla\psi^d$ is simply the velocity due to the wakes. After some algebraic manipulations, the discrete version of the unsteady Bernoulli equation can be expressed as

$$\begin{aligned}\frac{Dp^d}{\rho_F} &= [(\partial_t\varphi^d + \partial_t\psi^d)|_U - (\partial_t\varphi^d + \partial_t\psi^d)|_L] \\ &\quad + \frac{1}{2}(\boldsymbol{V}_\varphi^d + \boldsymbol{V}_\psi^d) \cdot (\boldsymbol{V}_\varphi^d + \boldsymbol{V}_\psi^d)|_U - \frac{1}{2}(\boldsymbol{V}_\varphi^d + \boldsymbol{V}_\psi^d) \cdot (\boldsymbol{V}_\varphi^d + \boldsymbol{V}_\psi^d)|_L, \\ &= [(\partial_t\varphi^d + \partial_t\psi^d)|_U - (\partial_t\varphi^d + \partial_t\psi^d)|_L] + \frac{1}{2}(\boldsymbol{V}_U^d \cdot \boldsymbol{V}_U^d - \boldsymbol{V}_L^d \cdot \boldsymbol{V}_L^d)\end{aligned} \tag{24}$$

where Dp^d is the discrete pressure jump, $\boldsymbol{V}_U^d = (\boldsymbol{V}_\varphi^d + \boldsymbol{V}_\psi^d)|_U$, and $\boldsymbol{V}_L^d = (\boldsymbol{V}_\varphi^d + \boldsymbol{V}_\psi^d)|_L$. Evaluation of $\boldsymbol{V}_\varphi$ requires using the equivalence relationship between doublets (or dipoles) and vortex rings of constant circulation [60]. Such equivalence allows us to compute the velocity contribution of each discrete vortex element $B_k \in \mathcal{A}_i \subset \mathcal{A}$ by using the B-S law. To keep the notation as compact and clear as possible, from now on, we will drop the superscript "i" and refer to a kth vortex element in $\mathcal{A}$ and $\mathcal{V}$ as B_k and L_k, respectively.

Because the nonpenetration condition must be satisfied at each control point CP_k, the fluid velocities computed relative to the lifting surfaces at the bound lattices do not have normal components. Therefore, there is a jump in the tangential velocity across each B_k equal to its circulation per unit length. As a result, the last term on the right-hand side of Eq. (24) can be computed at a control point CP_k as follows:

$$(\boldsymbol{V}_U^d \cdot \boldsymbol{V}_U^d - \boldsymbol{V}_L^d \cdot \boldsymbol{V}_L^d)_k = 2\boldsymbol{V}_{m,k}^d \cdot \Delta\boldsymbol{V}_k^d \tag{25}$$

where $\boldsymbol{V}_{m,k}^d = \boldsymbol{V}_{B,k}^d + \boldsymbol{V}_{W,k}^d + \boldsymbol{V}_{\infty,k}^d$ is the "mean" velocity, which does not recognize the presence of the local vorticity, and $\Delta\boldsymbol{V}_k^d$ represents the jump in the tangential velocity across B_k. The last term can be evaluated by considering three cases: a rectangular panel, a parallelogram panel, and a general panel (see Ref. [51]). For a general aerodynamic panel B_k, the jump in the tangential velocity $\Delta\boldsymbol{V}_k^d$ is given by

$$\Delta\boldsymbol{V}_k^d = -\frac{1}{A_k}[\hat{\boldsymbol{n}}_k \times \Gamma_k] \tag{26}$$

where A_k is the panel area, $\hat{\boldsymbol{n}}_k$ is the unit normal vector to panel B_k, and $\boldsymbol{\Gamma}_k = 0.5\sum_{j=1}^4 \Gamma_j \boldsymbol{\omega}_j$ (see Fig. 2). Different definitions for vector $\boldsymbol{\Gamma}_k$ are possible depending on the approach adopted. Here, we mostly follow the implementation proposed by researchers at Virginia Tech, where vectors $\boldsymbol{\omega}_j$ traverse the panel in a clockwise direction (same as G_k), and the circulation Γ_j associated with each $\boldsymbol{\omega}_j$ is determined as the difference between the ring circulations of the panels sharing such a segment.

On the other hand, the first term on the right-hand side of Eq. (24) is derived from a multivariable Taylor expansion of $\varphi^d(\boldsymbol{r}, t)$ and $\psi^d(\boldsymbol{r}, t)$ around $\boldsymbol{r}$ and t, i.e.,

$$\begin{aligned}\varphi^d(\boldsymbol{r} + \Delta\boldsymbol{r}, t + \Delta t) &= \varphi^d(\boldsymbol{r}, t) + \nabla\varphi^d(\boldsymbol{r}, t) \cdot \Delta\boldsymbol{r} + \partial_t\varphi^d(\boldsymbol{r}, t)\Delta t \\ &\quad + \mathcal{O}(\|\Delta\boldsymbol{r}\|^2, \|\Delta\boldsymbol{r}\|\Delta t, \Delta t^2)\end{aligned} \tag{27}$$

where $\Delta\boldsymbol{r}$ is an arbitrary but small displacement vector. In what follows, we present a procedure to find an expression for $\partial_t\varphi^d|_L^U$, and the same procedure applies for $\partial_t\psi^d|_L^U$. Without loss

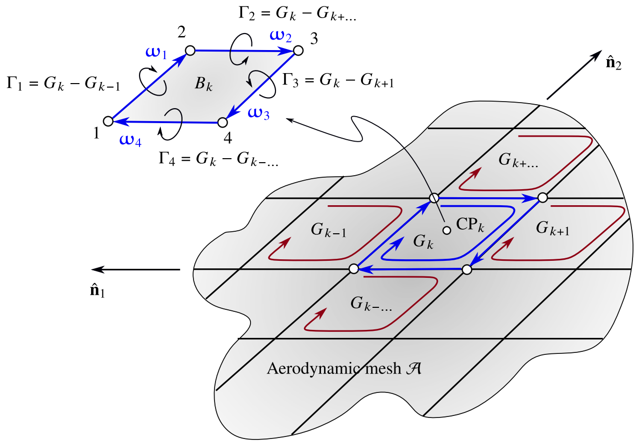

Fig. 2 Definition of ω_j and Γ_j for $j = 1, \ldots, 4$ associated with a generic aerodynamic panel $B_k \in \mathcal{A}$.

of generality, let us assume $\Delta\boldsymbol{r} = \boldsymbol{V}\Delta t$ for a fluid particle moving from a point $\boldsymbol{r}$ to $\boldsymbol{r} + \Delta\boldsymbol{r}$ during a time step Δt. Then it follows from Eq. (27) that

$$\partial_t\varphi^d(\boldsymbol{r},t) = \frac{\varphi^d(\boldsymbol{r}+\Delta\boldsymbol{r}, t+\Delta t) - \varphi^d(\boldsymbol{r},t)}{\Delta t} - \nabla\varphi^d(\boldsymbol{r},t)\cdot\frac{\Delta\boldsymbol{r}}{\Delta t} + \frac{1}{\Delta t}\mathcal{O}(\|\Delta\boldsymbol{V}\Delta t\|^2, \|\Delta\boldsymbol{V}\Delta t\|\Delta t, \Delta t^2) \tag{28}$$

Taking the limit for $\Delta t \to 0$ and considering a convenient choice for $\Delta\boldsymbol{r}$ (a point fixed either just below or just above a CP_k in $\mathcal{A}$), Eq. (28) becomes

$$\begin{aligned}\partial_t\varphi^d(\boldsymbol{r},t) &= \lim_{\Delta t\to 0}\frac{\varphi^d(\boldsymbol{r}+\Delta\boldsymbol{r}, t+\Delta t) - \varphi^d(\boldsymbol{r},t)}{\Delta t} - \lim_{\Delta t\to 0}\nabla\varphi^d(\boldsymbol{r},t)\\ &\quad\cdot\frac{\Delta\boldsymbol{r}}{\Delta t} + \lim_{\Delta t\to 0}\mathcal{O}(\|\boldsymbol{V}\|^2\Delta t, \|\boldsymbol{V}\|\Delta t, \Delta t),\\ &= \left.\frac{\text{Đ}\varphi^d}{\text{Đ}t}\right|_P - \boldsymbol{V}^d_\varphi(\boldsymbol{r},t)\cdot\boldsymbol{V}_P\end{aligned} \tag{29}$$

where P represents the point attached to the moving lattice $\mathcal{A}$, $\text{Đ}/\text{Đ}(\cdot)$ is the "substantial derivative" of $\varphi^d(\boldsymbol{r},t)$ following a point fixed to $\mathcal{A}$ (not a fluid particle), and $\boldsymbol{V}_P$ is the velocity of the point P fixed to $\mathcal{A}$. In a similar fashion, $\partial_t\psi^d(\boldsymbol{r},t)$ is found to be

$$\partial_t\psi^d(\boldsymbol{r},t) = \left.\frac{\text{Đ}\psi^d}{\text{Đ}t}\right|_P - \boldsymbol{V}^d_\psi(\boldsymbol{r},t)\cdot\boldsymbol{V}_P \tag{30}$$

Next, let us define the two points fixed to $\mathcal{A}$, one just above (U) and the other just below (L) the control point CP_k (see Fig. 3a). Such two points have the same velocity as the control point itself [i.e., $\boldsymbol{V}^d_U(\boldsymbol{r}_P) = \boldsymbol{V}^d_L(\boldsymbol{r}_P)$]. However, as mentioned before, there is a jump in the tangential velocity of the air flowing across the bound vortex lattice; hence, the fluid velocities at these two points differ. Recalling that $(\boldsymbol{V}^d_\varphi + \boldsymbol{V}^d_\psi)|_U = \boldsymbol{V}^d_U$ and $(\boldsymbol{V}^d_\varphi + \boldsymbol{V}^d_\psi)|_L = \boldsymbol{V}^d_L$, we can now compute $(\partial_t\varphi^d + \partial_t\psi^d)|^U_L$ as follows:

$$\begin{aligned}\partial_t(\varphi^d+\psi^d)|_U - \partial_t(\varphi^d+\psi^d)|_L &= \frac{\text{Đ}}{\text{Đ}t}[(\varphi^d+\psi^d)|_U\\ &\quad - (\varphi^d+\psi^d)|_L] - \Delta\boldsymbol{V}^d\cdot\boldsymbol{V}_P\end{aligned} \tag{31}$$

The first term on the right-hand side in Eq. (31) can be estimated with the help of Stokes's theorem. However, we need to be careful about its use here because any path that goes from a point (L), just below the CP_k, to another point (U), just above CP_k, encloses a domain with a discontinuous interface, i.e., the *bound-vortex lattice*. Following the same procedure used by Xia and Mohseni [64], it can be shown that Stokes's theorem for a domain containing a discontinuous surface, like the one we have here, keeps its original form. On this basis and recalling that $\varphi^d(\boldsymbol{r},t)$ and $\psi^d(\boldsymbol{r},t)$ are scalar potential functions, it follows that

$$(\varphi^d+\psi^d)|_U - (\varphi^d+\psi^d)|_L = \oint_{C(s)}\nabla(\varphi^d+\psi^d)\cdot\mathrm{d}\boldsymbol{C}(s) = \Gamma(t) \tag{32}$$

where $C(s)$ is a curve that goes from the point on the lower side of the vortex lattice around the leading edge to the same point on the upper side of the surface (see Fig. 3a). If there is no wake shedding from the leading edge, circulation $\Gamma(t)$ in Eq. (32) has the same value as the circulation $G(t)$ for the loop enclosing the control point; hence, at CP_k, we obtain

$$[\partial_t(\varphi^d+\psi^d)|_U - \partial_t(\varphi^d+\psi^d)|_L]_k = \frac{\text{Đ}}{\text{Đ}t}G_k(t) - \Delta\boldsymbol{V}^d_k\cdot\boldsymbol{V}_k \tag{33}$$

In most of the UVLM-based codes, the "substantial" derivative $(\text{Đ}/\text{Đ}t)G_k(t)$ is approximated by a first-order finite difference as follows [13,18,51]:

$$\frac{\text{Đ}}{\text{Đ}t}G_k(t) \approx \frac{G_k(t) - G_k(t-\Delta t)}{\Delta t} \tag{34}$$

where Δt is the time step to obtain the numerical solution.

If there is flow separation from the leading edge of the wing, the curve $C(s)$ in Eq. (32) also has to enclose the wake that is being shed from the LEs (see Fig. 3b). At this point, we must distinguish

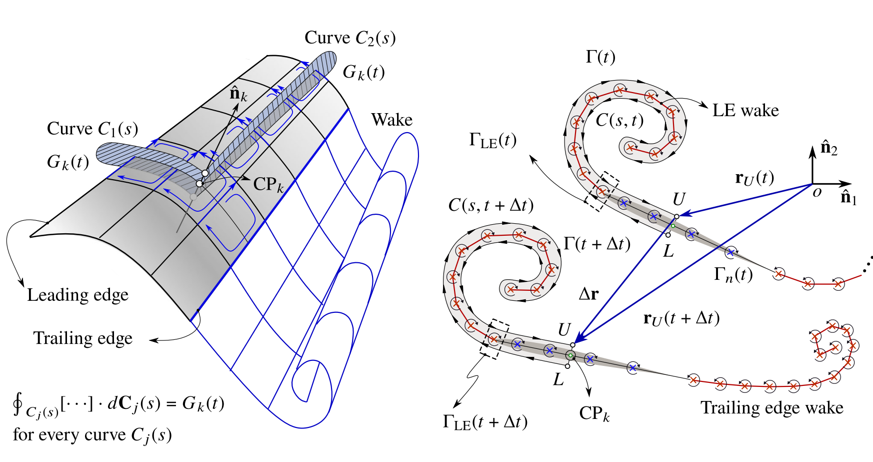

Fig. 3 a) Schematic of different paths used for computing $\text{Đ}/\text{Đ}t[(\varphi^d+\psi^d)|_U - (\varphi^d+\psi^d)|_L]$. b) Leading-edge wake treatment in two-dimensional flows.

between two- or three-dimensional flows. For two-dimensional problems, the intensity of the discrete vortices shed from the LEs can be estimated as $\Gamma_{\mathrm{LE}}(t) = (1/2)KV_u^2\Delta t$. K is a user-defined reduction parameter used to fit experimental results, and V_u is the velocity of a fluid particle located at the separation zone, known from the previous time step. Since the intensity of the vortices within the wake does not change with time, the only vortex that contributes to the substantial derivative is the one located on the leading edge at time t:

$$\frac{\text{Đ}}{\text{Đ}t}\Gamma_k(t) \approx \frac{\Gamma_k(t) - \Gamma_k(t-\Delta t)}{\Delta t} = \frac{\Gamma_{\mathrm{LE}}(t)}{\Delta t} + \sum_{j=1}^{k}\frac{\Gamma_j(t) - \Gamma_j(t-\Delta t)}{\Delta t} \tag{35}$$

where $\Gamma_j(t)$ is the circulation of the jth vortex belonging to $\mathcal{A}$ and enclosed by the curve $C(s)$, and $\Gamma_{\mathrm{LE}}(t)$ is the circulation of the last vortex shed from the LE $\in \mathcal{A}$ (see Fig. 3b).

In three-dimensional flows, the LE vortex system can be represented by discrete vortex lines similar to those used for the trailing edge wakes [13]. The circulation $G_{\mathrm{LE},j}(t)$ at time t of each new panel shed from the leading edge comes from its adjacent panel B_k on the bound vortex lattice, i.e., $G_{\mathrm{LE},j}(t) = G_k(t)$. Once the vortices are part of the wake, their intensity no longer changes with time. Since we are using a representation based on vortex rings of constant intensity, it can be shown that $\Gamma(t)$ in Eq. (32) has again the same value $G_k(t)$ for any path $C(s)$ going from a point below CP_k to another point above CP_k (see Fig. 3a).

Introducing Eq. (25) and Eq. (33) into Eq. (24), we obtain the pressure jump for the panel B_k as

$$\begin{aligned} Dp_k^d &= \rho_F \boldsymbol{V}_{m,k}^d \cdot \Delta \boldsymbol{V}_k^d + \rho_F \frac{\text{Đ}}{\text{Đ}t} G_k(t) - \rho_F \boldsymbol{V}_k \cdot \Delta \boldsymbol{V}_k^d \\ &= \rho_F[\boldsymbol{V}_{m,k}^d - \boldsymbol{V}_k] \cdot \Delta \boldsymbol{V}_k^d + \rho_F \frac{\text{Đ}}{\text{Đ}t} G_k(t) \end{aligned} \tag{36}$$

Finally, the vector force on the boundary element B_k is calculated as the product of Eq. (36) times the element area times the normal unit vector located at CP_k:

$$\boldsymbol{f}_k = Dp_k^d A_k \hat{\boldsymbol{n}}_k \tag{37}$$

C. Linearization of the Aerodynamic Loads

This subsection presents a procedure to linearize the aerodynamic loads equation (36). The computation of $D\boldsymbol{f}_k$ is fundamental to carry out several complex studies, such as nonlinear aeroelastic analysis considering implicit time integrators, sensibility analysis, and flight dynamic studies, among others.

In this work, we use a standard approach based on a Taylor expansion of Eq. (36) to obtain the tangent or sensitivity matrix associated with $\boldsymbol{f}_k$. To this end, Taylor's approximation for $\boldsymbol{f}_k$ on control point CP_k of $B_k \in \mathcal{A}$ is given by

$$\begin{aligned} \boldsymbol{f}_k(\boldsymbol{q}_k + \Delta\boldsymbol{q}_k, \boldsymbol{s}_k + \Delta\boldsymbol{s}_k) &= \boldsymbol{f}_k(\boldsymbol{q}_k, \boldsymbol{s}_k) + D\boldsymbol{f}_k(\boldsymbol{q}_k, \boldsymbol{s}_k) \cdot (\Delta\boldsymbol{q}_k, \Delta\boldsymbol{s}_k) \\ &\quad + D^2\boldsymbol{f}_k(\boldsymbol{q}_k, \boldsymbol{s}_k) : ((\Delta\boldsymbol{q}_k, \Delta\boldsymbol{s}_k) \otimes (\Delta\boldsymbol{q}_k, \Delta\boldsymbol{s}_k)) \\ &\quad + O\left(\sum_{j=0}^{3} \|\Delta\boldsymbol{q}_k\|^{3-j} \|\Delta\boldsymbol{s}_k\|^j\right) \end{aligned} \tag{38}$$

where $\boldsymbol{q}_k = (\boldsymbol{r}_k^T, \boldsymbol{X}^T)^T$; $\boldsymbol{s}_k = (\boldsymbol{V}_k^T, \boldsymbol{U}^T)^T$; $\boldsymbol{r}_k$ and $\boldsymbol{V}_k$ are the position and velocity vectors of control point CP_k; $\boldsymbol{X} = (\boldsymbol{x}_1^T, \ldots, \boldsymbol{x}_N^T)^T \in \mathbb{R}^{3N_n(t)}$ collects the coordinates of all the aerodynamic nodes in $\mathcal{A} \cup \mathcal{V}$; $\boldsymbol{U} = (\boldsymbol{u}_1^T, \ldots, \boldsymbol{u}_N^T)^T \in \mathbb{R}^{3N_n(t)}$ collects the nodal velocities of all the aerodynamic nodes in $\mathcal{A} \cup \mathcal{V}$; $D^i(\cdot)$ for $i = 1, 2, \ldots,$ is a $(i+1)$-order tensor of type $(0, i)$; $\Delta\boldsymbol{q}_k, \Delta\boldsymbol{s}_k \in \mathcal{T}_{\boldsymbol{q}_k}\mathbb{R}^{3+3N_n(t)}$ are tangent vectors; ":" indicates double-contraction tensor operation; $\otimes$ stands for tensor product; and $N_n(t) = N_{nb} + N_{nw}(t)$ is the total number of aerodynamic nodes in the bound- and free-vortex lattices at time t.

To make the linearization procedure for $\boldsymbol{f}_k$ as clear as possible while setting the expressions up for an eventual computational implementation, the following is assumed:

1) All vectors (position, velocities, accelerations, forces, etc.) are expressed with respect to a global (inertial) reference frame $\mathcal{E} = \{\hat{\boldsymbol{E}}_1, \hat{\boldsymbol{E}}_2, \hat{\boldsymbol{E}}_3\}$.

2) The coordinates of each control point are interpolated from the aerodynamic nodes of the panel to which it belongs via the transformation $\boldsymbol{r}_k = \mathcal{F}_k(\boldsymbol{Z}_k)$, where $\mathcal{F}_k: \mathbb{R}^{12} \to \mathbb{R}^3$ is a surjective linear mapping represented by a constant matrix $\boldsymbol{B}_k \in \mathbb{R}^{3\times 12}$, and $\boldsymbol{Z}_k = (\boldsymbol{z}_{k,1}^T, \boldsymbol{z}_{k,2}^T, \boldsymbol{z}_{k,3}^T, \boldsymbol{z}_{k,4}^T)^T \in \mathbb{R}^{12\times 1}$ collects the aerodynamic node coordinates of panel B_k (see Fig. 4).

3) The velocity vector of each control point CP_k^i is also interpolated by means of the linear mapping $\mathcal{F}_k$ as $\boldsymbol{V}_k = \boldsymbol{B}_k\dot{\boldsymbol{Z}}_k$, where $\dot{\boldsymbol{Z}}_k = (\dot{\boldsymbol{z}}_{k,1}^T, \dot{\boldsymbol{z}}_{k,2}^T, \dot{\boldsymbol{z}}_{k,3}^T, \dot{\boldsymbol{z}}_{k,4}^T)^T$ collects the velocity vectors of the aerodynamic nodes of panel B_k.

4) Position or velocity vectors of the aerodynamic nodes associated with a panel k are obtained from the global vectors $\boldsymbol{X}$ and $\boldsymbol{U}$ via the mapping $\boldsymbol{Z}_k = \mathcal{L}_k(\boldsymbol{X})$ and $\dot{\boldsymbol{Z}}_k = \mathcal{L}_k(\boldsymbol{U})$, where $\mathcal{L}_k: \mathbb{R}^{3N_n(t)} \to \mathbb{R}^{12}$ is represented by a constant Boolean matrix $\boldsymbol{L}_k \in \mathbb{R}^{12\times 3N_n(t)}$.

5) The expansion Eq. (38) is performed at frozen time, so the overall shape of the wakes does not change during this process, except for those free-vortex segments located at the separation zones. Consequently, a linearization of the free-vortex segments at the separation edges is required.

Since the aerodynamic force on CP_k depends on the velocity induced by all the panels belonging to either the bound-vortex lattices or the wakes, it is clear that the tensor $D^i\boldsymbol{f}_k$ depend on both the state of the panel k as well as the state of all the panels in $\mathcal{A} \cup \mathcal{V}$. Therefore, we must consider both the variation in the coordinates and velocities associated with CP_k (Case 1, Fig 4) as well as the variation in the coordinates and velocities of the aerodynamic nodes associated with all the panels in $\mathcal{A} \cup \mathcal{V}$ (Case 2, Fig. 4). However, due to assumption 5, the state of panels L_k belonging to $\mathcal{V}$ is considered frozen during Taylor's expansion, and thus their coordinate/velocity variations are identically zero. Under these assumptions, the dimension of vector $\Delta\boldsymbol{q}_k(\Delta\boldsymbol{s}_k)$ and Boolean matrix $\boldsymbol{L}_k$ is reduced from $(3 + 3N_n(t))$ to $(3 + 3N_{nb})$ and from $(12 \times 3N_n(t))$ to $(12 \times 3N_{nb})$, respectively. According to the above, and neglecting higher order terms, expansion Eq. (38) can be recast as follows:

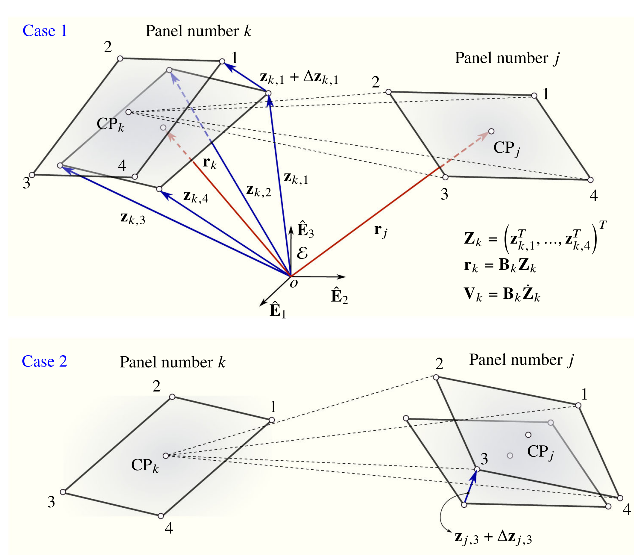

Fig. 4 Cases to take into account to compute $D\boldsymbol{f}_k(\boldsymbol{q}, \boldsymbol{s})$ associated with B_k.

$$
\begin{aligned}
\boldsymbol{f}_k(\boldsymbol{q}_k+\Delta\boldsymbol{q}_k,\boldsymbol{s}+\Delta\boldsymbol{s}_k) &\approx \boldsymbol{f}_k(\boldsymbol{q}_k,\boldsymbol{s}_k)+D\boldsymbol{f}_k(\boldsymbol{q}_k,\boldsymbol{s}_k)\cdot\Delta\boldsymbol{q}_k \\
&+ D\boldsymbol{f}_k(\boldsymbol{q}_k,\boldsymbol{s}_k)\cdot\Delta\boldsymbol{s}_k = \boldsymbol{f}_k(\boldsymbol{q}_k,\boldsymbol{s}_k)+\partial_{\boldsymbol{q}}\boldsymbol{f}_k(\boldsymbol{q}_k,\boldsymbol{s}_k)\cdot\Delta\boldsymbol{q}_k \\
&+ \partial_{\boldsymbol{s}}\boldsymbol{f}_k(\boldsymbol{q}_k,\boldsymbol{s}_k)\cdot\Delta\boldsymbol{s}_k
\end{aligned} \tag{39}
$$

where $\partial_{\boldsymbol{q}}\boldsymbol{f}_k, \partial_{\boldsymbol{s}}\boldsymbol{f}_k \in \mathbb{R}^{3\times(3N_{pb}+3N_{nb})}$ are second-order covariant tensors. Introducing Eq. (36) into Eq. (39) along with the definitions for $\boldsymbol{r}_k$ and $\boldsymbol{V}_k$ given in assumptions 2, 3, and 4, tensors $\partial_{\boldsymbol{q}}\boldsymbol{f}_k$ and $\partial_{\boldsymbol{s}}\boldsymbol{f}_k$ can be split and expressed as follows:

$$
\begin{aligned}
\partial_{\boldsymbol{q}}\boldsymbol{f}_k\cdot\Delta\boldsymbol{q}_k &= [\partial_{\boldsymbol{q}}(Dp_k^d A_k\hat{\boldsymbol{n}}_k)]\cdot\Delta\boldsymbol{q}_k \\
&= [\partial_{\boldsymbol{r}}(Dp_k^d A_k\hat{\boldsymbol{n}}_k)]\partial_{\boldsymbol{x}}(\boldsymbol{r}_k)\cdot\Delta\boldsymbol{X}+[\partial_{\boldsymbol{x}}(Dp_k^d A_k\hat{\boldsymbol{n}}_k)]\cdot\Delta\boldsymbol{X} \\
\partial_{\boldsymbol{s}}\boldsymbol{f}_k\cdot\Delta\boldsymbol{s}_k &= [\partial_{\boldsymbol{s}}(Dp_k^d A_k\hat{\boldsymbol{n}}_k)]\cdot\Delta\boldsymbol{s}_k \\
&= [\partial_{\boldsymbol{v}}(Dp_k^d A_k\hat{\boldsymbol{n}}_k)]\partial_{\boldsymbol{u}}(\boldsymbol{V}_k)\cdot\Delta\boldsymbol{U}+[\partial_{\boldsymbol{u}}(Dp_k^d A_k\hat{\boldsymbol{n}}_k)]\cdot\Delta\boldsymbol{U}
\end{aligned} \tag{40}
$$

where $\partial_{\boldsymbol{r}}(\cdot)\in\mathbb{R}^{3\times3}$, $\partial_{\boldsymbol{v}}(\cdot)\in\mathbb{R}^{3\times3}$, $\partial_{\boldsymbol{x}}(\cdot)\in\mathbb{R}^{3\times3N_{nb}}$, $\partial_{\boldsymbol{u}}(\cdot)\in\mathbb{R}^{3\times3N_{nb}}$, $\partial_{\boldsymbol{x}}(\boldsymbol{r}_k)=\boldsymbol{B}_k\boldsymbol{L}_k$, and $\partial_{\boldsymbol{u}}(\boldsymbol{V}_k)=\boldsymbol{B}_k\boldsymbol{L}_k$. Introducing such a definitions into Eq. (40), we obtain the following expressions for $\partial_{\boldsymbol{q}}\boldsymbol{f}_k$ and $\partial_{\boldsymbol{s}}\boldsymbol{f}_k$:

$$
\begin{aligned}
\partial_{\boldsymbol{q}}\boldsymbol{f}_k\cdot\Delta\boldsymbol{q}_k &= [\partial_{\boldsymbol{r}}(Dp_k^d A_k\hat{\boldsymbol{n}}_k)]\boldsymbol{B}_k\boldsymbol{L}_k\cdot\Delta\boldsymbol{X}+[\partial_{\boldsymbol{x}}(Dp_k^d A_k\hat{\boldsymbol{n}}_k)]\cdot\Delta\boldsymbol{X} \\
&= \boldsymbol{k}_{\boldsymbol{x}}^k\cdot\Delta\boldsymbol{X} \\
\partial_{\boldsymbol{s}}\boldsymbol{f}_k\cdot\Delta\boldsymbol{s}_k &= [\partial_{\boldsymbol{v}}(Dp_k^d A_k\hat{\boldsymbol{n}}_k)]\boldsymbol{B}_k\boldsymbol{L}_k\cdot\Delta\boldsymbol{U}+[\partial_{\boldsymbol{u}}(Dp_k^d A_k\hat{\boldsymbol{n}}_k)]\cdot\Delta\boldsymbol{U} \\
&= \boldsymbol{k}_{\boldsymbol{u}}^k\cdot\Delta\boldsymbol{U}
\end{aligned} \tag{41}
$$

where $\boldsymbol{k}_{\boldsymbol{x}}^k, \boldsymbol{k}_{\boldsymbol{u}}^k \in \mathbb{R}^{3\times3N_{nb}}$ are identified as the tangent matrices associated with the aerodynamic load $\boldsymbol{f}_k$ on panel B_k. Recalling that $\partial_{\boldsymbol{r}(\boldsymbol{v})}(\cdot)=\sum_{i=1}^{3}\partial_{r^i(v^i)}(\cdot)\otimes\hat{\boldsymbol{E}}_i$ and $\partial_{\boldsymbol{x}(\boldsymbol{u})}(\cdot)=\sum_{i=1}^{3N_{nb}}\partial_{x^i(u^i)}(\cdot)\otimes\hat{\boldsymbol{G}}_i$, with $\{\hat{\boldsymbol{G}}_1,\ldots,\hat{\boldsymbol{G}}_{3N_{nb}}\}$ being an orthonormal basis for $\mathbb{R}^{3N_{nb}}$, tangent matrices $\boldsymbol{k}_{\boldsymbol{x}}^k$ and $\boldsymbol{k}_{\boldsymbol{u}}^k$ are furthered split as

$$
\boldsymbol{k}_{\boldsymbol{x}}^k=\boldsymbol{k}_{\boldsymbol{x}p}+\boldsymbol{k}_{\boldsymbol{x}a}+\boldsymbol{k}_{\boldsymbol{x}n}, \quad \text{and} \quad \boldsymbol{k}_{\boldsymbol{u}}^k=\boldsymbol{k}_{\boldsymbol{u}p}+\boldsymbol{k}_{\boldsymbol{u}a}+\boldsymbol{k}_{\boldsymbol{u}n} \tag{42}
$$

where

$$
\begin{aligned}
\boldsymbol{k}_{\boldsymbol{x}p} &= \left[\sum_{i=1}^{3}[\partial_{r^i}(Dp_k^d)A_k\hat{\boldsymbol{n}}_k]\otimes\hat{\boldsymbol{E}}_i\right]\boldsymbol{B}_k\boldsymbol{L}_k+\sum_{i=1}^{3N_{nb}}[\partial_{x^i}(Dp_k^d)A_k\hat{\boldsymbol{n}}_k]\otimes\hat{\boldsymbol{G}}_i, \\
\boldsymbol{k}_{\boldsymbol{u}p} &= \left[\sum_{i=1}^{3}[\partial_{v^i}(Dp_k^d)A_k\hat{\boldsymbol{n}}_k]\otimes\hat{\boldsymbol{E}}_i\right]\boldsymbol{B}_k\boldsymbol{L}_k+\sum_{i=1}^{3N_{nb}}[\partial_{u^i}(Dp_k^d)A_k\hat{\boldsymbol{n}}_k]\otimes\hat{\boldsymbol{G}}_i, \\
\boldsymbol{k}_{\boldsymbol{x}a} &= \sum_{i=1}^{3N_{nb}}[Dp_k^d\partial_{x^i}(A_k)\hat{\boldsymbol{n}}_k]\otimes\hat{\boldsymbol{G}}_i, \quad \text{and} \\
\boldsymbol{k}_{\boldsymbol{x}n} &= \sum_{i=1}^{3N_{nb}}[Dp_k^d A_k\partial_{x^i}(\hat{\boldsymbol{n}}_k)]\otimes\hat{\boldsymbol{G}}_i
\end{aligned} \tag{43}
$$

The most complicated matrices to evaluate in Eq. (43) are those related to the derivative of the pressure jump, while $\boldsymbol{k}_{\boldsymbol{x}a}$ and $\boldsymbol{k}_{\boldsymbol{x}n}$ are straightforward to evaluate because they depend only on the nodal coordinates of panel B_k. It should be noted that $\boldsymbol{k}_{\boldsymbol{u}a}$ and $\boldsymbol{k}_{\boldsymbol{u}n}$ are null matrices due to area panels, and unit normal vectors do not depend on velocity. Next, we focus on the term $\partial_{r^i}(Dp_k^d)$; the reader can obtain $\partial_{x^i}(Dp_k^d)$, $\partial_{v^i}(Dp_k^d)$, and $\partial_{u^i}(Dp_k^d)$ by performing a similar procedure. For this purpose, let us consider Eq. (36), so $\partial_{r^i}(Dp_k^d)$ can be expanded as follows:

$$
\begin{aligned}
\partial_{r^i}(Dp_k^d) &= \rho_F[\partial_{r^i}\boldsymbol{V}_{m,k}^d-\partial_{r^i}\boldsymbol{V}_k]\cdot\Delta\boldsymbol{V}_k^d+\rho_F[\boldsymbol{V}_{m,k}^d-\boldsymbol{V}_k]\cdot\partial_{r^i}(\Delta\boldsymbol{V}_k^d) \\
&+\frac{\rho_F}{\Delta t}\partial_{r^i}(G_k(t)) \\
&= \rho_F[\partial_{r^i}(\boldsymbol{V}_{B,k}^d)+\partial_{r^i}(\boldsymbol{V}_{W,k}^d)-\partial_{r^i}(\boldsymbol{V}_k)]\cdot\Delta\boldsymbol{V}_k^d \\
&+\rho_F[\boldsymbol{V}_{B,k}^d+\boldsymbol{V}_{W,k}^d+\boldsymbol{V}_{\infty,k}^d-\boldsymbol{V}_k]\cdot\partial_{r^i}(\Delta\boldsymbol{V}_k^d)+\frac{\rho_F}{\Delta t}\partial_{r^i}(G_k(t))
\end{aligned} \tag{44}
$$

where $\partial_{r^i}(G_k(t-\Delta t))$ is zero because $G_k(t-\Delta t)$ is a quantity computed in a previous time step and therefore constant. By using Eq. (20), the terms $\partial_{r^i}(\boldsymbol{V}_{B,k}^d)$ and $\partial_{r^i}(\boldsymbol{V}_{W,k}^d)$ can be rewritten as

$$
\begin{aligned}
\partial_{r^i}(\boldsymbol{V}_{B,k}^d) &= \sum_{j=1}^{N_{pb}}\partial_{r^i}(\boldsymbol{In}(\boldsymbol{r}_k,B_j))G_j(t)+\sum_{j=1}^{N_{pb}}\boldsymbol{In}(\boldsymbol{r}_k,B_j)\partial_{r^i}(G_j(t)) \\
\partial_{r^i}(\boldsymbol{V}_{W,k}^d) &= \sum_{j=1}^{N_{pw}}\partial_{r^i}(\boldsymbol{In}(\boldsymbol{r}_k,L_j))G_j^w(t)
\end{aligned} \tag{45}
$$

where $G_j^w(t)$ is the constant ring circulation associated with the jth panel belonging to $\mathcal{V}$, and thus its derivative with respect to space coordinates or nodal velocities is zero, and $\partial_{r^i}(\boldsymbol{In}(\cdot))$ implies to compute the partial derivative of the B-S law with respect to the coordinates of the control point CP_k. Here, the partial derivative of the ring circulation $G_j(t)$ is computed implicitly by using the nonpenetration condition Eq. (18), i.e.,

$$
\begin{aligned}
&\partial_{r^i}\left(\sum_{j=1}^{N_{pb}}In(\boldsymbol{r}_k,B_j)G_j(t)\right)=\partial_{r^i}(\boldsymbol{V}_{W,k}^d\cdot\hat{\boldsymbol{n}}_k) \\
&\sum_{j=1}^{N_{pb}}In(\boldsymbol{r}_k,B_j)\partial_{r^i}(G_j(t))=\partial_{r^i}(\boldsymbol{V}_{W,k}^d)\cdot\hat{\boldsymbol{n}}_k+\boldsymbol{V}_{W,k}^d\cdot\partial_{r^i}(\hat{\boldsymbol{n}}_k) \\
&\qquad -\sum_{j=1}^{N_{pb}}\partial_{r^i}(In(\boldsymbol{r}_k,B_j))G_j(t)
\end{aligned} \tag{46}
$$

Equation (46) can be reformulated in matrix form by letting the index i go from 1 to N_{pb}, thus obtaining the following expression for the partial derivative of all the ring circulations with respect to r^i in $\mathcal{A}$:

$$
\partial_{r^i}(\boldsymbol{G}(t))=\boldsymbol{A}(t)^{-1}[\mathbf{RHS}_0^i(t)-\partial_{r^i}(\boldsymbol{A}(t))\boldsymbol{G}(t)] \tag{47}
$$

where

$$
\begin{aligned}
\mathbf{RHS}_0^i(t) = (&\partial_{r^i}(\boldsymbol{V}_{W,1}^d)\cdot\hat{\boldsymbol{n}}_1,\ldots,\partial_{r^i}(\boldsymbol{V}_{W,k}^d)\cdot\hat{\boldsymbol{n}}_k,\ldots, \\
&\partial_{r^i}(\boldsymbol{V}_{W,N_{pb}}^d)\cdot\hat{\boldsymbol{n}}_{N_{pb}})^T
\end{aligned} \tag{48}
$$

The last term left to deal with is $\partial_{r^i}(\Delta\boldsymbol{V}_k^d)$. Considering Eq. (26), the partial derivative of the jump in the tangential velocity across panel B_k with respect to r^i is given by

$$
\begin{aligned}
\partial_{r^i}(\Delta\boldsymbol{V}_k^d) &= -\frac{[\hat{\boldsymbol{n}}_k\times\boldsymbol{\Gamma}_k]}{A_k^2}\partial_{r^i}(A_k)-\frac{[\partial_{r^i}(\hat{\boldsymbol{n}}_k)\times\boldsymbol{\Gamma}_k]}{A_k}-\frac{[\hat{\boldsymbol{n}}_k\times\partial_{r^i}(\boldsymbol{\Gamma}_k)]}{A_k} \\
&= -\frac{1}{2A_k}\left[\hat{\boldsymbol{n}}_k\times\sum_{j=1}^{4}\partial_{r^i}(\Gamma_j)\boldsymbol{\omega}_j\right]
\end{aligned} \tag{49}
$$

where $\partial_{r^i}(A_k)$, $\partial_{r^i}(\hat{\boldsymbol{n}}_k)$, and $\partial_{r^i}(\boldsymbol{\omega}_j)$ are zero because they do not depend on coordinates of CP_k. On the other hand, as Γ_j is calculated by subtracting the vortex ring circulations of adjacent panels, its derivative with respect to r^i is straightforward to obtain once Eq. (47) is solved. As an example, let us consider $\Gamma_1=G_k-G_{k-1}$ (see Fig. 2), then its derivative is directly $\partial_{r^i}(\Gamma_1)=\partial_{r^i}(G_k)-\partial_{r^i}(G_{k-1})$.

The equations listed above [Eqs. (45–49)] show the details behind the calculation of the derivative of the pressure jump across panel B_k with respect to the control point coordinates CP_k. Similarly, to calculate the derivative of Dp_k^d with respect to x^i, v^i, and u^i, we need first to compute the following quantities:

$$\begin{aligned}
&\partial_{x^i}(\boldsymbol{V}_{W,k}^d \cdot \hat{\boldsymbol{n}}_k) = \boldsymbol{V}_{W,k}^d \cdot \partial_{x^i}(\hat{\boldsymbol{n}}_k), \quad \partial_{v^i}(\boldsymbol{V}_{W,k}^d \cdot \hat{\boldsymbol{n}}_k) = 0,\\
&\partial_{u^i}(\boldsymbol{V}_{W,k}^d \cdot \hat{\boldsymbol{n}}_k) = 0,\\
&\quad \partial_{x^i}(\boldsymbol{V}_k^d \cdot \hat{\boldsymbol{n}}_k) = \boldsymbol{V}_k^d \cdot \partial_{x^i}(\hat{\boldsymbol{n}}_k), \quad \partial_{v^i}(\boldsymbol{V}_k^d \cdot \hat{\boldsymbol{n}}_k) = \hat{\boldsymbol{E}}_i \cdot \hat{\boldsymbol{n}}_k, \quad \text{and}\\
&\quad \partial_{u^i}(\boldsymbol{V}_k^d \cdot \hat{\boldsymbol{n}}_k) = 0
\end{aligned} \tag{50}$$

which in turn allows us to obtain $\partial_{(\cdot)}(\boldsymbol{G}(t))$ by means of the following formulas:

$$\begin{aligned}
&\partial_{x^i}(\boldsymbol{G}(t)) = \boldsymbol{A}(t)^{-1}[\mathbf{RHS}_1^i(t) - \mathbf{RHS}_2^i(t) - \partial_{x^i}(\boldsymbol{A}(t))\boldsymbol{G}(t)],\\
&\partial_{v^i}(\boldsymbol{G}(t)) = \boldsymbol{A}(t)^{-1}[\mathbf{RHS}_3^i(t)], \quad \text{and} \quad \partial_{u^i}(\boldsymbol{G}(t)) = \mathbf{0}
\end{aligned} \tag{51}$$

where

$$\begin{aligned}
&\mathbf{RHS}_1^i(t) = (\boldsymbol{V}_{W,1}^d \cdot \partial_{x^i}(\hat{\boldsymbol{n}}_1), \ldots, \boldsymbol{V}_{W,k}^d \cdot \partial_{x^i}(\hat{\boldsymbol{n}}_k), \ldots, \boldsymbol{V}_{W,N_{pb}}^d \cdot \partial_{x^i}(\hat{\boldsymbol{n}}_{N_{pb}}))^T\\
&\mathbf{RHS}_2^i(t) = (\boldsymbol{V}_1^d \cdot \partial_{x^i}(\hat{\boldsymbol{n}}_1), \ldots, \boldsymbol{V}_k^d \cdot \partial_{x^i}(\hat{\boldsymbol{n}}_k), \ldots, \boldsymbol{V}_{N_{pb}}^d \cdot \partial_{x^i}(\hat{\boldsymbol{n}}_{N_{pb}}))^T\\
&\mathbf{RHS}_3^i(t) = -(\hat{\boldsymbol{n}}_1 \cdot \hat{\boldsymbol{E}}_i, \ldots, \hat{\boldsymbol{n}}_k \cdot \hat{\boldsymbol{E}}_i, \ldots, \hat{\boldsymbol{n}}_{N_{pb}} \cdot \hat{\boldsymbol{E}}_i)^T
\end{aligned} \tag{52}$$

Finally, we obtain the value of all the necessary derivatives to compute the tangent matrices associated with $\boldsymbol{f}_k$. They are listed below:

$$\begin{aligned}
&\partial_{x^i}(\boldsymbol{V}_{B,k}^d) = \sum_{j=1}^{N_{pb}} \partial_{x^i}(\boldsymbol{In}(\boldsymbol{r}_k, B_j))G_j(t) + \sum_{j=1}^{N_{pb}} \boldsymbol{In}(\boldsymbol{r}_k, B_j)\partial_{x^i}(G_j(t)),\\
&\partial_{v^i}(\boldsymbol{V}_{B,k}^d) = \sum_{j=1}^{N_{pb}} \boldsymbol{In}(\boldsymbol{r}_k, B_j)\partial_{v^i}(G_j(t)),\\
&\partial_{u^i}(\boldsymbol{V}_{B,k}^d) = \mathbf{0},\\
&\partial_{x^i}(\Delta \boldsymbol{V}_k^d) = -\frac{1}{A_k^2}[\hat{\boldsymbol{n}}_k \times \boldsymbol{\Gamma}_k]\partial_{x^i}(A_k) - \frac{1}{A_k}[\partial_{x^i}(\hat{\boldsymbol{n}}_k) \times \boldsymbol{\Gamma}_k],\\
&\qquad\qquad - \frac{1}{2A_k}\left[\hat{\boldsymbol{n}}_k \times \sum_{j=1}^{4}(\partial_{x^i}\Gamma_j)\boldsymbol{\omega}_j + \hat{\boldsymbol{n}}_k \times \sum_{j=1}^{4}\Gamma_j \partial_{x^i}(\boldsymbol{\omega}_j)\right],\\
&\partial_{v^i}(\Delta \boldsymbol{V}_k^d) = -\frac{1}{2A_k}\left[\hat{\boldsymbol{n}}_k \times \sum_{j=1}^{4}\partial_{v^i}(\Gamma_j)\boldsymbol{\omega}_j\right],\\
&\partial_{u^i}(\Delta \boldsymbol{V}_k^d) = \mathbf{0}
\end{aligned} \tag{53}$$

The linearization procedure presented above to evaluate the local tangent matrices associated with a panel $B_k \in \mathcal{A}$ must be applied for each panel on the lifting surfaces of $\mathcal{B}$. Then, two global tangent matrices are obtained by assembling the local tangent contributions as

$$\boldsymbol{K}_{\boldsymbol{x}} = \mathbb{A}(\boldsymbol{k}_{\boldsymbol{x}}^k) \tag{54}$$

$$\boldsymbol{K}_{\boldsymbol{u}} = \mathbb{A}(\boldsymbol{k}_{\boldsymbol{u}}^k) \tag{55}$$

where $\mathbb{A}(\cdot)$ represents the assembly operator. It should be noted that both the calculations described throughout this section and the assembling procedure depend on the available data structure and programming paradigm. Algorithm 1 is a general algorithm for computing the global tangent matrices associated with the aerodynamic loads acting on $\mathcal{B}$.

Algorithm 1: Standard algorithm for computing $\boldsymbol{K}_x$ and $\boldsymbol{K}_u$

```
for k = 1 to N_pb (consider only the lifting surfaces ∈ A_i if any)
  for i = 1 to N_nb
    Compute ∂_{x^i}(A_k),
    Compute ∂_{x^i}(n̂_k),
    Compute ∂_{x^i}(ω_j) for j = 1, …, 4 associated with B_k,
    Compute ∂_{x^i}(In(r_k, B_j)) for j = 1, …, N_pb,
  end
  for i = 1 to 3 (Consider only control point coordinates of panel k)
    Compute ∂_{r^i}(In(r_k, B_j)) for j = 1, …, N_pb,
    Compute ∂_{r^i}(In(r_k, L_j)) for j = 1, …, N_pw(t),
  end
end
Compute RHS_0^i(t) [Eq. (48)]
Compute RHS_1^i(t), RHS_2^i(t), and RHS_3^i(t) [see Eq. (52)]
Solve the linear algebraic systems Eqs. (47) and (51)
for k = 1 to N_pb
  for i = 1 to N_nb
    Compute ∂_{x^i}(V^d_{B,k}) [see Eq. (53)]
    Compute ∂_{x^i}(V^d_{W,k}) [see Eq. (50)]
    Compute ∂_{x^i}(V^d_k) [see Eq. (50)]
    Compute ∂_{x^i}(ΔV^d_k) [see Eq. (53)]
  end
  for i = 1 to 3
    Compute ∂_{r^i}(V^d_{B,k}) [see Eq. (45)]
    Compute ∂_{v^i}(V^d_{B,k}) [see Eq. (53)]
    Compute ∂_{r^i}(V^d_{W,k}) [see Eq. (45))
    Compute ∂_{r^i}(ΔV^d_k) [see Eq. (49)]
    Compute ∂_{v^i}(ΔV^d_k) [see Eq. (53)]
  end
  Compute ∂_{r^i}(Dp^d_k), ∂_{x^i}(Dp^d_k), and ∂_{v^i}(Dp^d_k)
  Compute local tangent matrices k^k_x and k^k_u [see Eq. (42)]
end
Assembling global tangent matrices K_x and K_u
```

III. Aeroelastic Model

One possible application of the presented aerodynamic linearization is the calculation of aerodynamic tangent matrices within a strongly coupled aeroelastic framework. Therefore, this section presents the implementation of the linearized aerodynamic loads into our aeroelastic framework, which relies on the combination of a state-of-the-art nonlinear structural model developed by the authors [30,65–67] and the UVLM [16]. The nonlinear governing equations are then iteratively solved with Newton's method, which requires the computation of the Jacobian matrix for the system's equations. This includes not only the derivatives of the structural loads but also those from the aerodynamic loads. Our proposed approach for calculating linearized aerodynamic loads, i.e., computing Eq. (42), is, in general, suitable for any nonlinear aeroelastic framework using gradient-based solution procedures. In the following, we briefly summarize the main ideas and the governing equations of the resulting aeroelastic problem. Further and more extensive details of our formulation, including theoretical aspects, are still ongoing work and, therefore, will be published in the future.

Our structural model is intended for nonlinear static and dynamic analysis of mechanical systems consisting of rigid and flexible structures made of single- or composite multilayer and hyperelastic materials. The formulation relies on a rotation-free multibody system formalism and the finite element method (FEM), which is presented in the total Lagrangian description, and builds upon a primal-dual formulation, including generalized coordinates and velocities. Moreover, our approach can easily handle nonconservative systems that arise in the presence of dissipation mechanisms, nonholonomic (nonintegrable) constraints, and nonconservative loads.

The adopted variational formulation for rigid and flexible bodies is given by

$$\int_{\mathcal{B}_0} [\delta \boldsymbol{v} \cdot [\boldsymbol{l}(\boldsymbol{v};t) - \boldsymbol{l}(\dot{\boldsymbol{x}};t)] + \delta \boldsymbol{x} \cdot [\boldsymbol{f}^{\text{int}}(\boldsymbol{x};t) - \boldsymbol{f}^{\text{ext}}(t) + \dot{\boldsymbol{l}}(\boldsymbol{v};t) + \boldsymbol{H}^T(\boldsymbol{x};t) \cdot \boldsymbol{\lambda}(t)] + \delta \boldsymbol{\lambda} \cdot \boldsymbol{h}(\boldsymbol{x};t)] d\mathcal{B}_0 \tag{56}$$

which comprises the momentum compatibility equation, the dynamic equilibrium equation, and the constraint equation. The first one is required for relating the state variables, i.e., position and velocity. Note that $\boldsymbol{x}(\boldsymbol{\theta};t) \in \mathcal{X} \subseteq \mathbb{R}^3$ is the spatial position vector, and $\boldsymbol{v}(\boldsymbol{\theta};t) \in \mathcal{V} \subseteq \mathbb{R}^3$ is the velocity vector of any material point. These specific quantities depend on the chosen canonical model; $\delta \boldsymbol{x} \in T_{\boldsymbol{x}}\mathcal{X}$ and $\delta \boldsymbol{v} \in T_{\boldsymbol{v}}\mathcal{V}$ are their admissible variations. $\mathcal{B}_0$ is an open subset of $\mathbb{R}^3$ described by reference coordinates $\boldsymbol{\theta} = \{\theta^1, \theta^2, \theta^3\}$; $\boldsymbol{f}^{\text{int}}$ is the vector of internal force density defined through the identity $\int_{\mathcal{B}_0} \delta \boldsymbol{x} \cdot \boldsymbol{f}^{\text{int}}(\boldsymbol{x};t)\, d\mathcal{B}_0 = \int_{\mathcal{B}_0} \delta \boldsymbol{E}(\boldsymbol{x};t) : \boldsymbol{S}(\boldsymbol{E};t)\, d\mathcal{B}_0$, with $\boldsymbol{E}$ standing for the Green–Lagrange strain (tensor) measure and $\boldsymbol{S}$ representing the second Piola–Kirchhoff stress (tensor) measure. Both are related through the internal energy functional $\boldsymbol{\mathcal{W}}^{\text{int}}$ by $\boldsymbol{S}(\boldsymbol{E};t) = \partial_{\boldsymbol{E}} \boldsymbol{\mathcal{W}}_{\text{int}}(\boldsymbol{E};t)$ for any conservative (hyperelastic) material model. Logically, the internal force density for rigid bodies vanishes. The vector of conservative external body force density is indicated by $\boldsymbol{f}^{\text{ext}}$. $\boldsymbol{l}(\boldsymbol{v};t)$ is the velocity-based momentum density and $\boldsymbol{l}(\dot{\boldsymbol{x}};t)$ is the corresponding position-based momentum density; $\dot{\boldsymbol{l}}(\boldsymbol{v};t)$ describes the time rate of the velocity-based momentum density and represents inertia forces/moments; $\boldsymbol{\lambda} \in \mathbb{R}^{n_c}$ is the vector of Lagrange multipliers required to enforce the holonomic kinematic constraints given by $\boldsymbol{h} \in \mathbb{R}^{n_c}$ and $\delta\boldsymbol{\lambda}$ is its admissible variation. Finally, $\boldsymbol{H} \in \mathbb{R}^{n_c \times 3}$ is the Jacobian of the constraint equation.

For the present work, we consider two canonical models, i.e., the rigid body and the geometrically exact beam, whose kinematics is entirely described by a director-based parameterization and, thus, avoiding the typical singularities of rotational degrees of freedom. Moreover, we describe the governing equations in terms of generalized coordinates $\boldsymbol{q}(t) \in Q$ and generalized velocities $\boldsymbol{s}(t) \in S$, with the base manifold $Q \times S \cong \mathbb{R}^n \times \mathbb{R}^n$. Thus, it is necessary to define a constraint map $\boldsymbol{h}: Q \to \mathbb{R}^m$ such that $\boldsymbol{h}(\boldsymbol{q};t) = 0$ to restrict the dynamic to the submanifold $Q^h \subset \mathbb{R}^{n-m} \subset Q \cong \mathbb{R}^n$. In combination with the total Lagrangian description adopted here, this setting allows to maintain important physical features, i.e., the objectivity of the continuous/discrete strain measure under rigid space transformations and the path independence of the continuous/discrete formulation under the action of conservative loading [29,30,68–70].

The first canonical model, which is very rich in kinematic concepts, is the rigid body whose spatial position and velocity maps are given by $\boldsymbol{x}_{rb}(\boldsymbol{\theta};t) = \bar{\boldsymbol{x}}(t) + \theta^1 \boldsymbol{d}_1(t) + \theta^2 \boldsymbol{d}_2(t) + \theta^3 \boldsymbol{d}_3(t)$, and $\boldsymbol{v}_{rb}(\boldsymbol{\theta};t) = \bar{\boldsymbol{v}}(t) + \theta^1 \boldsymbol{w}_1(t) + \theta^2 \boldsymbol{w}_2(t) + \theta^3 \boldsymbol{w}_3(t)$, in which $\boldsymbol{d}_i \in \mathbb{R}^3$ for $i \in \{1,2,3\}$, the directors, are three mutual orthonormal unit vectors. On that basis, any orientation can be described by the rotation tensor $\boldsymbol{R} = \boldsymbol{d}_i \otimes \hat{\boldsymbol{E}}^i \in \text{SO}(3)$, in which $\hat{\boldsymbol{E}}^i$ for $i \in \{1,2,3\}$ is the standard Euclidean cobasis. Note that $\bar{\boldsymbol{x}} \in \mathbb{R}^3$ is the position vector of a reference point. The velocity is defined by the translational velocity of the reference point, $\bar{\boldsymbol{v}} \in \mathbb{R}^3$, and three director velocity vectors $\boldsymbol{w}_i \in \mathbb{R}^3$. The set of parameters $\boldsymbol{\theta} = \{\theta^1, \theta^2, \theta^3\}$ is chosen in such a way that $\bar{\boldsymbol{\theta}} = \theta^1 \boldsymbol{d}_1 + \theta^2 \boldsymbol{d}_2 + \theta^3 \boldsymbol{d}_3$ describes the position of any point of the body with a reference volume $\mathcal{B}_0$ relative to $\bar{\boldsymbol{x}}$. The generalized coordinate and velocity maps for the rigid body are $\boldsymbol{q}_{rb}(t) = (\bar{\boldsymbol{x}}(t), \boldsymbol{d}_1(t), \boldsymbol{d}_2(t), \boldsymbol{d}_3(t)) \in Q_{rb} \cong \mathbb{R}^{12}$, and $\boldsymbol{s}_{rb}(t) = (\bar{\boldsymbol{v}}(t), \boldsymbol{w}_1(t), \boldsymbol{w}_2(t), \boldsymbol{w}_3(t)) \in Q_{rb} \cong \mathbb{R}^{12}$, and the required constraint map is defined by the following conditions on the three directors $\boldsymbol{h}_{rb}(\boldsymbol{q}_{rb};t) = (\{\|\boldsymbol{d}_i(t)\|_2^2 - 1\}_{i=1}^3, \langle \boldsymbol{d}_1(t), \boldsymbol{d}_2(t) \rangle, \langle \boldsymbol{d}_2(t), \boldsymbol{d}_3(t) \rangle, \langle \boldsymbol{d}_1(t), \boldsymbol{d}_3(t) \rangle)$.

The second canonical model is the geometrically exact beam whose spatial position and velocity maps are given by $\boldsymbol{x}_{\text{geb}}(\boldsymbol{\theta};t) = \bar{\boldsymbol{x}}(\theta^3;t) + \theta^1 \boldsymbol{d}_1(\theta^3;t) + \theta^2 \boldsymbol{d}_2(\theta^3;t)$, and $\boldsymbol{v}_{\text{geb}}(\boldsymbol{\theta};t) = \bar{\boldsymbol{v}}(\theta^3;t) + \theta^1 \boldsymbol{w}_1(\theta^3;t) + \theta^2 \boldsymbol{w}_2(\theta^3;t)$, in which the set of parameters $\boldsymbol{\theta} = \{\theta^1, \theta^2, \theta^3\}$ is chosen in such a way that $\bar{\boldsymbol{\theta}} = \theta^1 \boldsymbol{d}_1 + \theta^2 \boldsymbol{d}_2$ describes the position of any point relative to reference point $\bar{\boldsymbol{x}} \in \mathbb{R}^3$ on the cross section A_0 with the length coordinate $\theta^3 \in [0, L_0]$, where L_0 stands for the initial arc length of the beam. Despite that the kinematical description leads to a two-director formulation, we use a three-director formulation, which simplifies the derivation of the governing equations and facilitates defining connections among beams and rigid bodies. The generalized coordinate and velocity maps for the geometrically exact beam are $\boldsymbol{q}_{\text{geb}}(\theta^3;t) = (\bar{\boldsymbol{x}}(\theta^3;t), \boldsymbol{d}_1(\theta^3;t), \boldsymbol{d}_2(\theta^3;t), \boldsymbol{d}_3(\theta^3;t)) \in Q_{\text{geb}} \cong \mathbb{R}^{12}$, and $\boldsymbol{s}_{\text{geb}}(\theta^3;t) = (\bar{\boldsymbol{v}}(\theta^3;t), \boldsymbol{w}_1(\theta^3;t), \boldsymbol{w}_2(\theta^3;t), \boldsymbol{w}_3(\theta^3;t)) \in Q_{\text{geb}} \cong \mathbb{R}^{12}$. Similarly to the rigid body, the orthonormality condition for the directors must be satisfied $\boldsymbol{h}_{\text{geb}}(\boldsymbol{q}_{\text{geb}};t) = (\{\|\boldsymbol{d}_i(\theta^3;t)\|_2^2 - 1\}_{i=1}^3, \langle \boldsymbol{d}_1(\theta^3;t), \boldsymbol{d}_2(\theta^3;t) \rangle, \langle \boldsymbol{d}_2(\theta^3;t), \boldsymbol{d}_3(\theta^3;t) \rangle, \langle \boldsymbol{d}_1(\theta^3;t), \boldsymbol{d}_3(\theta^3;t) \rangle)$.

To handle Eq. (56) numerically, we discretize the governing equations by spatially approximating the state variables (generalized coordinates and velocities) by means of the finite element method. Particularly, we adopt a low-order isoparametric approach with low-order Lagrangian functions. The semidiscrete equations are then temporally discretized using an implicit time integration method based on discrete derivatives [30,31]. This integration method ensures the preservation of linear and angular momenta as well as the preservation of total energy in the absence of external loads. In essence, the time integration scheme relies on the midpoint rule and the "average vector field" method. Then, the contributions due to the momentum equivalence and the dynamic equilibrium are evaluated at the time instant $t = t_{n+(1/2)}$ whereas the contribution due to the constraint is evaluated at the time instant $t = t_{n+1}$. Concomitantly, the admissible discrete variations are $(\delta \boldsymbol{s}_{n+(1/2)}, \delta \boldsymbol{q}_{n+(1/2)}, \delta \boldsymbol{\lambda}_{n+1})$. The final discrete form of Eq. (56) is given by

$$\begin{aligned} \delta \hat{S}_{n+(1/2)} = {} & \delta \hat{\boldsymbol{s}}_{n+(1/2)} \cdot [\hat{\boldsymbol{l}}(\hat{\boldsymbol{s}}_n, \hat{\boldsymbol{s}}_{n+1}) - \hat{\boldsymbol{l}}(\hat{\boldsymbol{q}}_n, \hat{\boldsymbol{q}}_{n+1})] + \delta \hat{\boldsymbol{q}}_{n+(1/2)} \\ & \cdot [\dot{\hat{\boldsymbol{l}}}(\hat{\boldsymbol{s}}_n, \hat{\boldsymbol{s}}_{n+1}) + \hat{\boldsymbol{f}}^{\text{int}}(\hat{\boldsymbol{q}}_n, \hat{\boldsymbol{q}}_{n+1}) \\ & - \{\hat{\boldsymbol{f}}^{\text{ext},c} + \hat{\boldsymbol{f}}^{\text{ext,nc}}(\hat{\boldsymbol{q}}_n, \hat{\boldsymbol{q}}_{n+1}, \hat{\boldsymbol{s}}_n, \hat{\boldsymbol{s}}_{n+1})\} + \hat{\boldsymbol{H}}^T(\hat{\boldsymbol{q}}_n, \hat{\boldsymbol{q}}_{n+1}) \\ & \cdot \hat{\boldsymbol{\lambda}}_{n+(1/2)}] + \delta \hat{\boldsymbol{\lambda}}_{n+1} \cdot \hat{\boldsymbol{h}}(\hat{\boldsymbol{q}}_{n+1}, \hat{\boldsymbol{q}}_n) = 0 \end{aligned} \tag{57}$$

which is solved for the unknowns at the time instant t_{n+1}. In Eq. (57), the discretized variables/terms are represented by the notation $\hat{(\cdot)}$. Furthermore, the mechanical model incorporates nonconservative external loads, $\hat{\boldsymbol{f}}^{\text{ext,nc}}$, which allows for the integration of aerodynamic loads, to encompass the adopted UVLM.

A crucial aspect of combining numerical structural and aerodynamic models lies in the strategy employed for the information transfer between their meshes. In this work, we transfer the aerodynamic loads coming from the UVLM, see Eq. (37), into our structural model, stating that for any time t_n the virtual work done by the aerodynamic loads, $\boldsymbol{f}_k$, at the control points on the aerodynamic mesh, $\boldsymbol{r}_k$, should be equal to the virtual work done on the nodes of the structural mesh through the discrete generalized aerodynamic forces $\hat{\boldsymbol{f}}^{\text{ext},ae} \in \mathbb{R}^{n_q}$:

$$\sum_{k=1}^{N_{pb}} \delta \boldsymbol{r}_k \cdot \boldsymbol{f}_k(\boldsymbol{X}, \boldsymbol{U}; t_n) - \delta \hat{\boldsymbol{q}} \cdot \hat{\boldsymbol{f}}^{\text{ext},ae}(\hat{\boldsymbol{q}}, \hat{\boldsymbol{s}}, t_n) = 0 \tag{58}$$

Furthermore, the spatial coordinates of any point on the fluid domain can be mapped into the configuration space of the structural model using a linear surjective vector-valued mapping function $\boldsymbol{\psi}^r$, i.e., $\boldsymbol{\psi}^r : \boldsymbol{q} \to \boldsymbol{r}$, as

$$\boldsymbol{r}(t) = \boldsymbol{\psi}^r(\boldsymbol{q}(t)) \tag{59}$$

Applying Eq. (59) to both, the discretized aerodynamic and discretized structural domains enable us to represent the coordinates of each control point $\boldsymbol{r}_k$ with the discretized generalized coordinates of the canonical model using the subsequent weighted form:

$$\boldsymbol{\psi}^{r_k}(\hat{\boldsymbol{q}}(t_n)) = \sum_{i=1}^{N_{ns}} [w_i(\gamma_{k,i}) \boldsymbol{r}_{k,i}(\hat{\boldsymbol{q}}_i(t_n))] \tag{60}$$

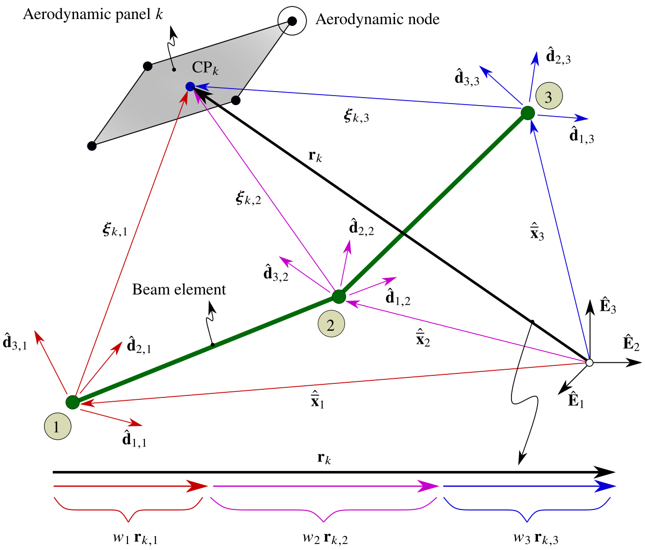

Fig. 5 Coordinate mapping taking into account geometrically exact beams.

in which $\boldsymbol{r}_{k,i} = \boldsymbol{r}_k$ is the control point k position vector in terms of the generalized coordinates $\hat{\boldsymbol{q}}_i$ of node i, and N_{ns} denotes the number of discrete nodes of the structural mesh. The rigid body and the geometrically exact beam element share a common configuration space based on a three-director formulation. In this context, $\boldsymbol{r}_{k,i}$ can be expressed as follows (see Fig. 5):

$$\begin{aligned}\boldsymbol{r}_{k,i}(\hat{\boldsymbol{q}}_i(t_n)) &= \hat{\hat{\boldsymbol{x}}}_i(t_n) + \xi^1_{i,k}\hat{\boldsymbol{d}}_{1,i}(t_n) + \xi^2_{i,k}\hat{\boldsymbol{d}}_{2,i}(t_n) + \xi^3_{i,k}\hat{\boldsymbol{d}}_{3,i}(t_n) \\ &= \hat{\hat{\boldsymbol{x}}}_i(t_n) + \boldsymbol{\xi}_{k,i}(t_n)\end{aligned} \tag{61}$$

where $\xi^j_{i,k} = (\boldsymbol{r}_k(0) - \hat{\hat{\boldsymbol{x}}}_i(0)) \cdot \boldsymbol{d}_{j,i}(0)$ for $j \in \{1,2,3\}$ are relative coordinate parameters that denote the distance between control point k and the reference point in the director system at time instant $t = 0$.

The weighting factor w_i in Eq. (60) accounts for the influence of the generalized coordinates to the aerodynamic control points based on the initial spatial distance between them, i.e., $\gamma_{k,i} = \|\boldsymbol{\xi}_{k,i}(0)\| = \|\boldsymbol{r}_k(0) - \hat{\hat{\boldsymbol{x}}}_i(0)\|$. To determine these weights, we utilize a radial-based bump function for all points and/or nodes on the fluid domain. The bump function is a compact support C^∞ function defined as $w(\gamma) = \exp[-(1/1 - x^2)]$ for $x = (\gamma/\gamma_{\text{ref}}) \in (-1, 1)$ and $w(\gamma) = 0$ otherwise. Note that γ_{ref} represents a user-defined fixed search radius that serves as a distance threshold, limiting the range of interest in transferring information among the models. Furthermore, incorporating Eq. (59) and Eq. (60) into Eq. (58), we obtain

$$\delta\hat{\boldsymbol{q}} \cdot \left[\sum_{k=1}^{N_{pb}}\left\{\left(\frac{\partial\boldsymbol{\psi}^{r_k}}{\partial\hat{\boldsymbol{q}}}\right)^T \cdot \boldsymbol{f}_k(\boldsymbol{X},\boldsymbol{U};t_n)\right\} - \hat{\boldsymbol{f}}^{\text{ext,ae}}(\hat{\boldsymbol{q}},\hat{\boldsymbol{s}};t_n)\right] = 0 \tag{62}$$

By applying the fundamental lemma of the calculus of variations, we can derive the following expression for the vector of discrete generalized aerodynamic forces:

$$\hat{\boldsymbol{f}}^{\text{ext},ae}(\hat{\boldsymbol{q}},\hat{\boldsymbol{s}};t_n) = \sum_{k=1}^{N_{pb}}\left\{\left(\frac{\partial\boldsymbol{\psi}^{r_k}}{\partial\hat{\boldsymbol{q}}}\right)^T \cdot \boldsymbol{f}_k(\boldsymbol{X},\boldsymbol{U};t_n)\right\} \tag{63}$$

Continuing with Eq. (57) and employing the fundamental lemma of variational calculus again, considering arbitrary nonzero variations $(\delta\hat{\boldsymbol{s}}, \delta\hat{\boldsymbol{q}}, \delta\hat{\boldsymbol{\lambda}})$ and reordering, we obtain a system of vector-valued nonlinear equations denoted by $\hat{\boldsymbol{g}}$ as follows:

$$\begin{aligned}&\hat{\boldsymbol{g}}(\hat{\boldsymbol{q}},\hat{\boldsymbol{s}},\hat{\boldsymbol{\lambda}})|_{n+1} \\ &= \begin{bmatrix} \dot{\hat{\boldsymbol{l}}}(\hat{\boldsymbol{s}}) + \hat{\boldsymbol{f}}^{\text{int}}(\hat{\boldsymbol{q}}) - \{\hat{\boldsymbol{f}}^{\text{ext},c} + \hat{\boldsymbol{f}}^{\text{ext,nc}}(\hat{\boldsymbol{q}}) + \hat{\boldsymbol{f}}^{\text{ext,ae}}(\hat{\boldsymbol{q}},\hat{\boldsymbol{s}})\} + \hat{\boldsymbol{H}}^T(\hat{\boldsymbol{q}})\cdot\hat{\boldsymbol{\lambda}} \\ \hat{\boldsymbol{l}}(\hat{\boldsymbol{s}}) - \hat{\boldsymbol{l}}(\hat{\boldsymbol{q}}) \\ \hat{\boldsymbol{h}}(\hat{\boldsymbol{q}}) \end{bmatrix}_{n+1} \\ &= \boldsymbol{0}\end{aligned} \tag{64}$$

where the first equation represents the discrete dynamic equilibrium, capturing the balance of forces acting on the system. The second equation corresponds to the momentum compatibility, and the third one represents the discrete constraints. While we do not explicitly express the specific dependencies arising from the employed time integration method, denoted as $(\hat{\boldsymbol{q}}_n, \hat{\boldsymbol{q}}_{n+1}, \hat{\boldsymbol{s}}_n, \hat{\boldsymbol{s}}_{n+1}, \hat{\boldsymbol{\lambda}}_{n+(1/2)})$, as outlined in Eq. (57), we remind the reader to consider them in Eq. (64) and the equations herein. The subscript "$n+1$" indicates that the unknowns are solved at time step t_{n+1}. Equation (64) is solved iteratively using Newton's method, requiring the Taylor expansion neglecting higher-order terms obtaining the following linearized form:

$$\hat{\boldsymbol{g}}(\hat{\boldsymbol{q}},\hat{\boldsymbol{s}},\hat{\boldsymbol{\lambda}})|^{i+1}_{n+1} = \hat{\boldsymbol{g}}(\hat{\boldsymbol{q}},\hat{\boldsymbol{s}},\hat{\boldsymbol{\lambda}})|^{i}_{n+1} + \Delta\hat{\boldsymbol{g}}(\hat{\boldsymbol{q}},\hat{\boldsymbol{s}},\hat{\boldsymbol{\lambda}})|^{i}_{n+1} = \boldsymbol{0} \tag{65}$$

where the superscript i denotes the iteration step within the Newton iteration process, and $\Delta\hat{\boldsymbol{g}}$ represents the discrete increment of $\hat{\boldsymbol{g}}$ obtained by calculating the partial derivatives with respect to the discrete generalized variables and the Lagrange multiplier, that is to say,

$$\begin{aligned}\Delta\hat{\boldsymbol{g}}(\hat{\boldsymbol{q}},\hat{\boldsymbol{s}},\hat{\boldsymbol{\lambda}})|^{i}_{n+1} &= \left.\frac{\partial\hat{\boldsymbol{g}}}{\partial\hat{\boldsymbol{q}}}\right|^{i}_{n+1} \cdot \Delta\hat{\boldsymbol{q}} + \left.\frac{\partial\hat{\boldsymbol{g}}}{\partial\hat{\boldsymbol{s}}}\right|^{i}_{n+1} \cdot \Delta\hat{\boldsymbol{s}} + \left.\frac{\partial\hat{\boldsymbol{g}}}{\partial\hat{\boldsymbol{\lambda}}}\right|^{i}_{n+1} \cdot \Delta\hat{\boldsymbol{\lambda}} \\ &= \hat{\boldsymbol{K}}(\hat{\boldsymbol{q}},\hat{\boldsymbol{s}},\hat{\boldsymbol{\lambda}})|^{i}_{n+1} \cdot \Delta\hat{\boldsymbol{X}}\end{aligned} \tag{66}$$

with $\hat{\boldsymbol{K}} \in \mathbb{R}^{(n_q+n_s+n_c)\times(n_q+n_s+n_c)}$ in Eq. (66) is denoted as the global system's tangent matrix of Eq. (64) and is called the iteration matrix within the context of Newton's method. In our aeroelastic framework, the matrix consists of two constituents: the Jacobian of the structural model, denoted as $\hat{\boldsymbol{K}}^s$, which is computed based on the partial derivatives of the discrete structural forces, the discrete equivalence of linear momentum, and the constraint equations; and the Jacobian of the discrete generalized aerodynamic forces, denoted as $\hat{\boldsymbol{K}}^{ae}$ as follows:

$$\hat{\boldsymbol{K}}(\hat{\boldsymbol{q}},\hat{\boldsymbol{s}},\hat{\boldsymbol{\lambda}})|^{i}_{n+1} = \hat{\boldsymbol{K}}^s(\hat{\boldsymbol{q}},\hat{\boldsymbol{s}},\hat{\boldsymbol{\lambda}})|^{i}_{n+1} - \hat{\boldsymbol{K}}^{ae}(\hat{\boldsymbol{q}},\hat{\boldsymbol{s}},\hat{\boldsymbol{\lambda}})|^{i}_{n+1} \tag{67}$$

The definitions for these constituents are given by

$$\begin{aligned}\hat{\boldsymbol{K}}^s(\hat{\boldsymbol{q}},\hat{\boldsymbol{s}},\hat{\boldsymbol{\lambda}})|^{i}_{n+1} &= \begin{bmatrix} \hat{\boldsymbol{K}}_{\hat{q}\hat{q}}(\hat{\boldsymbol{q}},\hat{\boldsymbol{s}},\hat{\boldsymbol{\lambda}}) & \hat{\boldsymbol{K}}_{\hat{q}\hat{s}} & \hat{\boldsymbol{H}}^T(\hat{\boldsymbol{q}}) \\ \hat{\boldsymbol{K}}_{\hat{s}\hat{q}} & \hat{\boldsymbol{K}}_{\hat{s}\hat{s}}(\hat{\boldsymbol{s}},\hat{\boldsymbol{\pi}}) & \boldsymbol{0} \\ \hat{\boldsymbol{H}}(\hat{\boldsymbol{q}}) & \boldsymbol{0} & \boldsymbol{0} \end{bmatrix}^{i}_{n+1}, \\ \hat{\boldsymbol{K}}^{ae}(\hat{\boldsymbol{q}},\hat{\boldsymbol{s}})|^{i}_{n+1} &= \begin{bmatrix} \hat{\boldsymbol{K}}^{ae}_{\hat{q}\hat{q}}(\hat{\boldsymbol{q}},\hat{\boldsymbol{s}}) & \hat{\boldsymbol{K}}^{ae}_{\hat{q}\hat{s}}(\hat{\boldsymbol{q}},\hat{\boldsymbol{s}}) & \boldsymbol{0} \\ \boldsymbol{0} & \boldsymbol{0} & \boldsymbol{0} \\ \boldsymbol{0} & \boldsymbol{0} & \boldsymbol{0} \end{bmatrix}^{i}_{n+1}\end{aligned} \tag{68}$$

To maintain focus on the linearization of the aerodynamic loads, we will abstain from providing a detailed explanation of the tangent matrix $\hat{\boldsymbol{K}}^s$. Interested readers are referred to [30,67] for a comprehensive understanding of this aspect. Subsequently, we proceed to outline the computation of $\hat{\boldsymbol{K}}^{ae}$, which is obtained from the incremental form of the discrete generalized aerodynamic forces in Eq. (64):

$$\Delta \hat{\boldsymbol{f}}^{\text{ext},ae} = \frac{\partial \hat{\boldsymbol{f}}^{\text{ext},ae}}{\partial \hat{\boldsymbol{q}}} \cdot \Delta \hat{\boldsymbol{q}} + \frac{\partial \hat{\boldsymbol{f}}^{\text{ext},ae}}{\partial \hat{\boldsymbol{s}}} \cdot \Delta \hat{\boldsymbol{s}} = \hat{\boldsymbol{K}}^{ae}_{\hat{q}\hat{q}} \cdot \Delta \hat{\boldsymbol{q}} + \hat{\boldsymbol{K}}^{ae}_{\hat{q}\hat{s}} \cdot \Delta \hat{\boldsymbol{s}} \tag{69}$$

In Eq. (69), $\hat{\boldsymbol{K}}^{ae}_{\hat{q}\hat{q}} \in \mathbb{R}^{n_q \times n_q}$ and $\hat{\boldsymbol{K}}^{ae}_{\hat{q}\hat{s}} \in \mathbb{R}^{n_s \times n_s}$ are the tangent matrices of generalized aerodynamic forces that can be derived by considering the expression of the generalized aerodynamic forces in Eq. (63) in conjunction with the directional derivative of the aerodynamic loads from the aerodynamic model given in Eq. (41) and applying the linear coordinate mapping presented in Eq. (59) on the nodal position vector $\boldsymbol{X}$, defined by the mapping function $\boldsymbol{\psi}^x$, i.e., $\boldsymbol{\psi}^x : \hat{\boldsymbol{q}} \to \boldsymbol{x}, \hat{\boldsymbol{s}} \to \boldsymbol{u}$. These matrices are then computed as follows:

$$\hat{\boldsymbol{K}}^{ae}_{\hat{q}\hat{q}} = \sum_{k=1}^{N_{pb}} \left\{ \frac{\partial}{\partial \boldsymbol{\xi}} \left[\left(\frac{\partial \boldsymbol{\psi}^{r_k}(\boldsymbol{\xi})}{\partial \boldsymbol{\xi}} \right)^T \cdot \boldsymbol{f}_k(\boldsymbol{X}, \boldsymbol{U}; t_n) \right] \bigg|_{\xi = \hat{q}} \right\} + \sum_{k=1}^{N_{pb}} \left\{ \left(\frac{\partial \boldsymbol{\psi}^{r_k}}{\partial \hat{\boldsymbol{q}}} \right)^T \cdot \boldsymbol{k}^k_{\boldsymbol{x}} \right\} \cdot \frac{\partial \boldsymbol{\psi}^x(\hat{\boldsymbol{q}})}{\partial \hat{\boldsymbol{q}}} \tag{70}$$

and

$$\hat{\boldsymbol{K}}^{ae}_{\hat{q}\hat{s}} = \sum_{k=1}^{N_{pb}} \left\{ \left(\frac{\partial \boldsymbol{\psi}^{r_k}}{\partial \hat{\boldsymbol{q}}} \right)^T \cdot \boldsymbol{k}^k_{\boldsymbol{u}} \right\} \cdot \frac{\partial \dot{\boldsymbol{\psi}}^x(\hat{\boldsymbol{s}})}{\partial \hat{\boldsymbol{s}}} \tag{71}$$

The reader should note that the fluid–structure mapping $\boldsymbol{\psi}^r$ adopted in this work is linear in $\hat{\boldsymbol{q}}$, and therefore the first term in Eq. (70) vanishes. Due to the nature of the defined aeroelastic problem, the matrices in Eqs. (70) and (71) are nonsymmetric and, in general, may not be positive definite or semidefinite, particularly when nonlinear effects or unsteady phenomena are taken into account. $\hat{\boldsymbol{K}}^{ae}_{\hat{q}\hat{q}}$ captures the sensitivity of the aerodynamic forces to changes in the structural configuration. It represents the partial derivative of the aerodynamic forces with respect to the structural configuration parameters. The entries of this matrix quantify how small variations in the structural deformations or positions influence the resulting aerodynamic forces. The tangent matrix $\hat{\boldsymbol{K}}^{ae}_{\hat{q}\hat{s}}$ represents the sensitivity of the aerodynamic forces to changes in the structural velocity. The entries of this matrix indicate how small changes in the structural velocities affect the resulting aerodynamic forces. The information on both matrices is valuable for various applications, including aeroelastic analysis, aircraft design, control system development, and structural optimization.

In nonlinear aeroelastic approaches, incorporating aerodynamic tangent matrices poses notable advantages. In particular, for strong coupled nonlinear time-domain computations, the full linearization of Eq. (64) significantly improves the numerical convergence behavior while solving with Newton's method. In the neighborhood of the solution, the convergence of Newton's method exhibits quadratic behavior. Besides accelerated convergence, the numerical robustness is improved as well, which is crucial for addressing challenges associated with large displacements, rotations, and velocity gradients. While geometrically exact finite element models demonstrate exceptional robustness in handling large structural displacements and rotations, they are susceptible to result in ill-conditioned algebraic equations [71]. Such equations can significantly hinder the convergence behavior of the numerical solution. The examples presented next demonstrate that the incorporation of both aerodynamic and structural tangent matrices enhances the robustness of the convergence behavior and reduces the number of iteration steps required during the solution process. It is noteworthy that test simulations revealed that employing a quasi-Newton's method resulted in linear or sublinear convergence rates, which, in certain instances, can lead to divergence. Furthermore, calculating the aerodynamic tangent matrices offers another crucial benefit: it enables a precise investigation of aeroelastic stability by analyzing the algebraic characteristics of the linearized governing equations, a task that cannot be accurately accomplished without complete linearization. Specifically, the eigenvalues and the determinant of the system's Jacobian hold significant information about the structural and aeroelastic stability. On the one hand, tracking the determinant and eigenvalues during the solution of Eq. (64) serves as a valuable resource for identifying critical values, such as flutter and divergence speeds. On the other hand, it is possible to formulate eigenvalue problems around any equilibrium state to predict and narrow the range of such critical velocities without performing full nonlinear calculations.

IV. Numerical Results

This section presents two examples intended for verifying our approach of the analytical computation of tangent matrices, with the main focus on their applicability to nonlinear aeroelasticity. By considering the pure aerodynamic problem, we perform in the first subsection a plausibility check for a rigid-fixed wing with a homogeneous thin-flat airfoil. This involves determining the maximal absolute deviation between the tangent matrices obtained analytically and those computed numerically. Furthermore, we provide the numerical values associated with the tangent matrices computed for the sake of reproducibility. In the second subsection, we showcase the validity, effectiveness, and benefits of the proposed linearization framework within a strong coupled nonlinear aeroelastic simulation model. This is accomplished through nonlinear static and dynamic aeroelastic analyses conducted for a suspension bridge deck. We compare our results with those obtained with simplified analytical approaches and other more complex numerical models given in the existing literature. Finally, we show how our analytically computed tangent matrices for the aerodynamic loads can significantly enhance the robustness and improve the convergence behavior of the nonlinear solution procedure.

A. Example 1: Aerodynamic Matrices of a Rectangular Wing

In this subsection, we investigate the accuracy of our analytically computed tangent matrices presented in Eqs. (54) and (55) by comparing them with numerically computed matrices. To perform this verification, we consider a rigid-fixed wing with a homogeneous thin-flat airfoil. The wing under investigation has a span of 2.0 m and a chord of 1.0 m. The freestream velocity is constant, and the wind flows at an angle of attack $\alpha = 10^\circ$ with an intensity $V_\infty = 10.0$ m/s. We then calculate the aerodynamic tangent matrices at the specific time instant $t = 0.4$ s, taking into account as well those matrix components capturing effects due to the shedding wake and unsteady aerodynamic contributions. At this stage, the aerodynamic condition has not yet reached steady state. We consider a percentual cutoff radius $\delta_c = 1\%$, and the incremental simulation time considered is $\Delta t = 0.01$ s. Figure 6 depicts the vortex lattice, including node and vortex-ring numbering, and illustrates the free-wake at the time instant $t = 0.08$ s.

We calculate the maximal absolute errors of the tangent matrices associated with the linearized aerodynamic loads, $\boldsymbol{K}_{\boldsymbol{x}}$ and $\boldsymbol{K}_{\boldsymbol{u}}$, as well as with the linearized nonpenetration condition, namely, $\boldsymbol{K}_{\boldsymbol{G},\boldsymbol{x}}$ and $\boldsymbol{K}_{\boldsymbol{G},\boldsymbol{u}}$. Tangent matrices $\boldsymbol{K}_{\boldsymbol{G},\boldsymbol{x}}$ and $\boldsymbol{K}_{\boldsymbol{G},\boldsymbol{u}}$ can be obtained using expressions similar to Eq. (47) detailed in Sec. II.C to $\boldsymbol{K}_{\boldsymbol{G},\boldsymbol{x}} = [\partial_{\hat{r}^i} \boldsymbol{G}(t) \otimes \hat{\boldsymbol{W}}_i]\boldsymbol{H} + \partial_{x^i} \boldsymbol{G}(t) \otimes \hat{\boldsymbol{G}}_i$ and $\boldsymbol{K}_{\boldsymbol{G},\boldsymbol{u}} = [\partial_{\hat{v}^i} \boldsymbol{G}(t) \otimes \hat{\boldsymbol{W}}_i]\boldsymbol{H}$, where $\boldsymbol{K}_{\boldsymbol{G},\boldsymbol{x}}, \boldsymbol{K}_{\boldsymbol{G},\boldsymbol{u}} \in \mathbb{R}^{N_{pb} \times 3N_{nb}}$, $\{\hat{\boldsymbol{W}}_1, \ldots, \hat{\boldsymbol{W}}_{3N_{pb}}\}$ is an orthonormal basis for $\mathbb{R}^{3N_{pb}}$, and $\boldsymbol{H} \in \mathbb{R}^{N_{pb} \times 3N_{nb}}$ is a constant matrix representing a linear mapping $\mathcal{H} : \mathbb{R}^{3N_{nb}} \to \mathbb{R}^{N_{pb}}$ such as $\hat{\boldsymbol{r}} = \boldsymbol{H}\boldsymbol{X}$ and $\hat{\boldsymbol{v}} = \boldsymbol{H}\boldsymbol{U}$, $\hat{\boldsymbol{r}}$

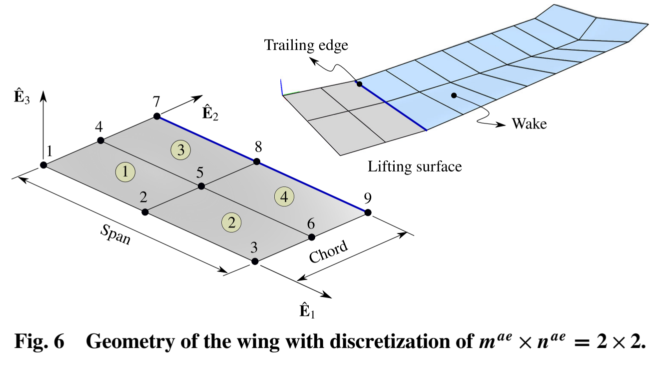

Fig. 6 Geometry of the wing with discretization of $m^{ae} \times n^{ae} = 2 \times 2$.

and $\hat{\boldsymbol{v}}$ collect the coordinates and velocities of all the control points on the lifting surface, and $\{\hat{\boldsymbol{G}}_1, \ldots, \hat{\boldsymbol{G}}_{3N_{pb}}\}$ was already defined in Sec. II.C. To determine the different errors, we are required to define an error function as

$$\varepsilon(\boldsymbol{K_x}) := \max_{i\in I, j\in J}\{|(K_x)_{ij} - (\overline{K}_x)_{ij}|\} \tag{72}$$

where $\varepsilon(\boldsymbol{K_x})$ is a scalar representing the maximal deviation between entities of the analytically computed matrices and the numerically computed ones. $I = \{1, \ldots, m^{ae}\}$ and $J = \{1, \ldots, n^{ae}\}$, with m^{ae} standing for the number of panels in spanwise direction and n^{ae} being the number of panels in chordwise direction. The bar notation in Eq. (72) indicates the numerical matrices. Finally, the errors are determined as

$$\varepsilon_{K_x} = \varepsilon(\boldsymbol{K_x}), \quad \varepsilon_{K_u} = \varepsilon(\boldsymbol{K_u}), \quad \varepsilon_{K_{G,x}} = \varepsilon(\boldsymbol{K_{G,x}}),$$
$$\varepsilon_{K_{G,u}} = \varepsilon(\boldsymbol{K_{G,u}}) \tag{73}$$

Table 1 Absolute error between analytical and numerical differentiation

$m^{ae} \times n^{ae}$	ε_{K_x}	ε_{K_u}	$\varepsilon_{K_{G,x}}$	$\varepsilon_{K_{G,u}}$
2×2	$1.8063 \cdot 10^{-8}$	$6.2274 \cdot 10^{-9}$	$6.5222 \cdot 10^{-10}$	$2.5087 \cdot 10^{-10}$
10×4	$3.3168 \cdot 10^{-9}$	$2.7949 \cdot 10^{-9}$	$2.0530 \cdot 10^{-9}$	$8.2402 \cdot 10^{-10}$
50×8	$1.8504 \cdot 10^{-9}$	$8.3710 \cdot 10^{-10}$	$3.2088 \cdot 10^{-9}$	$2.6551 \cdot 10^{-9}$
50×10	$1.9846 \cdot 10^{-9}$	$1.6312 \cdot 10^{-9}$	$4.2093 \cdot 10^{-9}$	$3.0596 \cdot 10^{-9}$

By introducing the finite-difference operator for the chosen scheme through

$$\mathcal{D}(F_i, x_j) = \frac{F_i(x_j + h, \boldsymbol{U}) - F_i(x_j - h, \boldsymbol{U})}{2h} \tag{74}$$

all required numerical matrices are computed as

$$(\overline{K}_x)_{ij} = \mathcal{D}(F_i, x_j), \quad (\overline{K}_u)_{ij} = \mathcal{D}(F_i, u_j), \quad (\overline{K}_{G,x})_{ij} = \mathcal{D}(G_i, x_j),$$
$$(\overline{K}_{G,u})_{ij} = \mathcal{D}(G_i, u_j) \tag{75}$$

To mitigate the impact of roundoff/truncation errors associated with Eq. (74), the step size h is normally selected according to $h_{\text{opt}} = \sqrt[3]{\varepsilon_M} \approx 10^{-6}$, where ε_M is the machine precision. If $h < h_{\text{opt}}$, then the roundoff error is sacrificed in favor of a decrease in the truncation error. Conversely, if $h > h_{\text{opt}}$, then the truncation error in $\mathcal{D}(F_i, \boldsymbol{x}_j)$ increases. We evaluate Eq. (73) for various mesh sizes. The results are summarized in Table 1. It can be concluded that the deviations between the analytically computed matrices and the numerically determined matrices are minimal, with a maximal deviation of 1.81×10^{-8}. Additionally, Figs. 7–10 provide interested readers with visual representations of the analytically computed tangent matrices for the mesh size $m^{ae} \times n^{ae} = 2 \times 2$, facilitating comparisons of numeric values for own implementations.

To further validate the accuracy of the analytically computed tangent matrices, it is crucial to assess their performance within a nonlinear framework. By applying our analytical linearization approach, the convergence behavior near the solution of a nonlinear equation can provide insights into the correctness of the computed

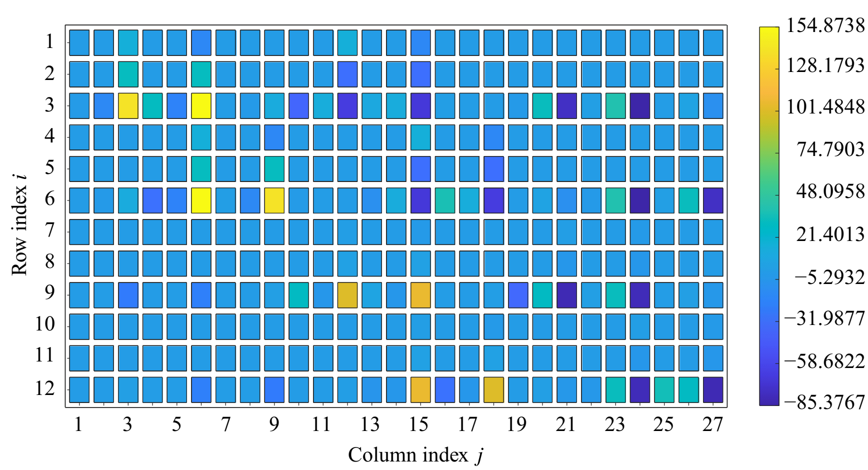

Fig. 7 Visual representation of $\boldsymbol{K_x}$ for $m^{ae} \times n^{ae} = 2 \times 2$.

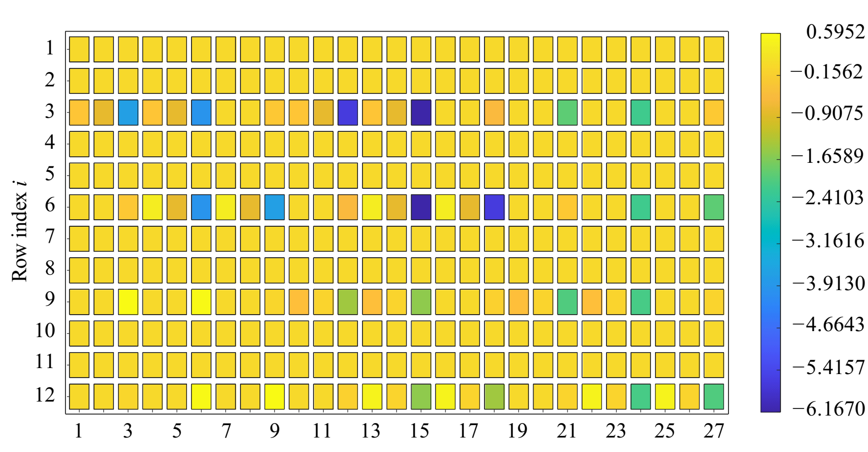

Fig. 8 Visual representation of $\boldsymbol{K_u}$ for $m^{ae} \times n^{ae} = 2 \times 2$.

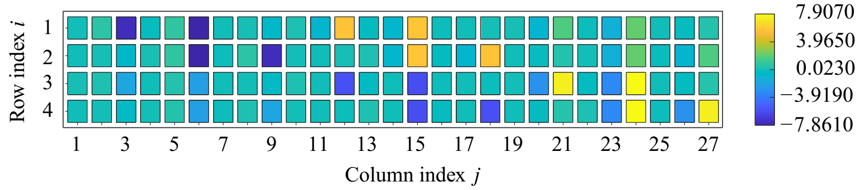

Fig. 9 Visual representation of $K_{G,x}$ for $m^{ae} \times n^{ae} = 2 \times 2$.

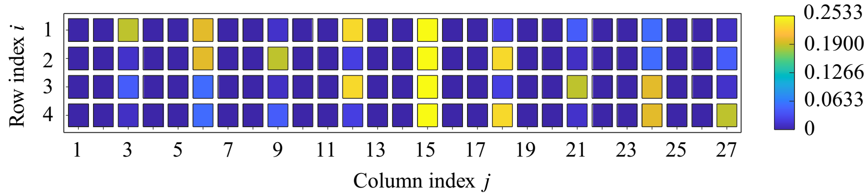

Fig. 10 Visual representation of $K_{G,u}$ for $m^{ae} \times n^{ae} = 2 \times 2$.

tangent matrices. In an aeroelastic context, if the linearization is done correctly, the convergence of the solution procedure should exhibit quadratic behavior. In the subsequent subsection, we employ our approach to solve implicitly the nonlinear aeroelastic governing equations, demonstrating the achievement of quadratic convergence behavior. This analysis serves as additional evidence for the accuracy and reliability of the analytically computed tangent matrices.

B. Example 2: Aeroelastic Analysis of a Suspension Bridge's Deck

In this subsection, we investigate the capability and validity of our proposed linearization framework within nonlinear aeroelasticity. Particularly, we conduct static and dynamic aeroelastic analyses for the case of a suspension's bridge deck given in [72]. We consider this example to validate our approach against its well-documented analytical solution. It is important to note, however, that we plan to apply our method to more complex nonlinear systems in the future, such as the Pazy wing [73–76]. Currently, we compute critical velocities, specifically divergence, and flutter by using two different methodologies: i) by solving eigenvalue problems formulated from the linearized aeroelastic model, and ii) by performing fully nonlinear static and dynamic simulations [Eq. (64) for static aeroelasticity, neglecting unsteady contributions]. The reader should be aware that the first approach clearly requires the aerodynamic tangent matrices previously computed. In addition, we perform a single nonlinear static aeroelastic deformation analysis in steady-state conditions under a constant freestream velocity, resulting in large displacements and rotations, and provide insights into computational performance. It is worth noting that for all static calculations presented here, the influence of the wake is taken into account in its steady-state configuration. To capture the final wake geometry accurately, we convect the wake within each simulation step until a steady state is reached. Therefore, the path leading to the static solution is solely of a numerical nature and does not represent a physical process.

1. *Model of the Bridge Deck*

Fung originally investigated the bridge deck's aeroelastic behavior using a structural model consisting of a linear elastic rotational and transversal spring combined with Theodorsen's aerodynamic method (see [72]). Based on the simplified model, Fung computed the aeroelastic stability problem for the flutter speed. The structural parameters used in the study are as follows: chord length $c = 60.0$ ft, squared gyration ratio $r_\alpha^2 = 0.6222$, mass density per unit length $m = 269.0$ slug/ft, natural bending frequency $\omega_h = 0.88$ rad/s, and natural torsion frequency $\omega_\alpha = 1.55$ rad/s. To adapt Fung's model to our aeroelastic model (UVLM + three-dimensional geometrically exact beams), we determine the elastic properties to achieve a cantilever's identical torsional and bending eigenfrequencies. We employed a constant rectangular cross section with isotropic linear elastic material properties, specifically Young's modulus $E = 1.936 \times 10^7$ lbf/ft^2, a shear modulus $G = 7.840 \times 10^4$ lbf/ft^2, and a material density $\rho = 8.027 \times 10^{-2}$ slug/ft^3. This yields a cross-sectional dimension with a chord length $c = 60.0$ ft and a thickness of $t = 55.85$ ft. It is worth noting that the resulting thickness t does not correspond to a thin plate. However, this choice allows us to reproduce the desired structural behavior, focusing primarily on involving flapwise and torsional motions while minimizing edgewise motion. As Fung's mechanical formulations do not account for shear deformations, and our model does, we need to mitigate their influence by incorporating sufficiently large shear stiffness ($GA_1 = GA_2 = 1.0 \times 10^{12}$ lbf ft^2). Additionally, a cantilever length $L = 1000.0$ ft is chosen. The air density is given by $\rho_F = 2.378 \times 10^{-3}$ slug/m^3. All geometry and material input data for both the structural and aerodynamic models are provided in Table 2. The first six natural eigenfrequencies, belonging to in-plane bending (IPB), out-of-plane bending (OPB), and torsional mode shapes calculated from our structural model, are presented in Table 3. Among these eigenfrequencies, the first and third eigenfrequencies are of particular importance. They correspond to the first bending and first torsion eigenmodes, respectively, and are expected to match the values proposed by Fung in his study [72].

The accuracy of the results and computational cost are influenced by the mesh discretization. Even provided that midfidelity methods, such as the UVLM, are less time-consuming than high-fidelity methods (e.g., CFD-like techniques), the computation time increases significantly with higher mesh densities. In this respect, we first

Table 2 Geometry and material input data parameter for aeroelastic model

Parameter	Value	Unit
Length, L	1000.0	ft
Chord, c	60.0	ft
Thickness, t	55.85	ft
Fluid density, ρ_F	$2.378 \cdot 10^{-3}$	slug/m^3
Young's modulus, E	$1.936 \cdot 10^{7}$	lbf/ft^2
Shear modulus, G	$7.840 \cdot 10^{4}$	lbf/ft^2
Material density, ρ	$8.027 \cdot 10^{-2}$	slug/ft^3

Table 3 Natural eigenfrequencies in rad/s of the beam model

No.	ω_n	Mode
1	0.880	1st IPB
2	0.945	1st OPB
3	1.552	1st torsional
4	4.659	2nd torsional
5	5.498	2nd IPB
6	5.902	2nd OPB

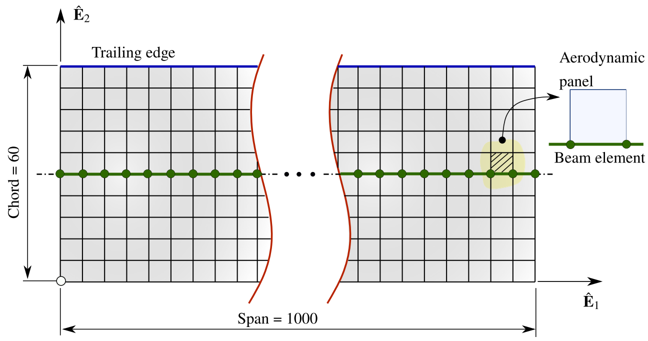

Fig. 11 Final mesh, $m^{ae} \times n^{ae} \times m^s = 40 \times 10 \times 40$.

conduct a convergence analysis by considering different mesh densities. Specifically, the parameters that can be optimized are the number of vortex rings in the spanwise direction m^{ae}, chordwise direction n^{ae}, and the number of finite beam elements m^s along the spanwise direction. To simplify the analysis, we assume $m^s = m^{ae}$. The mesh convergence analysis consists of performing full nonlinear aeroelastic simulations until steady-state regime is reached. The freestream velocity is set to 190 ft/s with an angle of attack $\alpha = 5°$. We evaluate the coordinates of the aerodynamic center at the aerodynamic mesh $\boldsymbol{x}^{AC} = [x_1^{AC} \quad x_2^{AC} \quad x_3^{AC}]$ and the torsion angle ϕ_1 of the plate tip on the structural mesh. The converged mesh is depicted in Fig. 11, where the green line indicates the beam elements and the blue line represents the flow separation edge. It consists of $m^{ae} \times n^{ae} = 40 \times 10 = 400$ vortex rings and $m^s = 40$ beam elements. The resulting coordinates of the aeroelastic center are $\boldsymbol{x}^{AC} = [513.9 \quad 14.4 \quad 0.0]$ ft.

2. *Static Aeroelasticity: Divergence Analysis*

One important problem in steady-state aeroelasticity is the computation of the torsional divergence speed V_c. Generally, aeroelastic divergence occurs when the elastic stiffness of a lifting surface under lift moments is barely sufficient to keep the structure in an undisturbed position. For a specific free-field velocity, the divergence speed, an infinitesimally small perturbation of the geometry, or the angle of attack can trigger a sudden transition from a stable equilibrium configuration to an unstable one, resulting in a substantial torsion angle [72].

To obtain an initial prediction for the divergence speed of a flat plate, we can solve the second-order linear homogeneous differential equation that governs the behavior of a torsional bar. The equation takes the following form [72,77]:

$$GI_T \frac{\partial^2 \phi_1(x_1)}{\partial^2 x_1} - \frac{dC_L}{d\alpha} q c x_2^{AC} \phi_1(x_1) = 0 \tag{76}$$

Here, x_1 represents the coordinate along the spanwise direction, q denotes the dynamic pressure, GI_T represents the torsional stiffness, c is the chord length, and x_2^{AC} corresponds to the coordinate of the aerodynamic center in the chordwise direction. The lift slope coefficient $dC_L/d\alpha$ can be analytically determined for elliptic wings with finite length using the finite wing theory. It is defined by $(dC_L/d\alpha) = 2\pi(AR/AR + 2)$, where AR represents the wing's aspect ratio. The torsional divergence speed can be obtained as the smallest nontrivial solution of Eq. (76), given by $V_c = \sqrt{2q_c/\rho_{\mathrm{F}}}$, with $q_c = (\pi/2L)^2[GI_T/(dC_L/d\alpha)cx_2^{AC}]$. By considering the specific material and geometrical data of the bridge deck and using $x_2^{AC} = 14.4$ ft (obtained above), the analytical solution for the torsional divergence speed is $V_c = 252.0$ ft/s.

In the following, we present two numerical methods to determine the critical velocity using our nonlinear aeroelastic model, both relying on the linearized aerodynamic loads. The first approach involves linearizing the static form of the governing equations [Eq. (64) by neglecting velocity-dependent terms] around an equilibrium point, i.e., $\boldsymbol{g} = \boldsymbol{0}$. The linearization process results in a homogeneous system of equations, which can be solved as a linear eigenvalue problem. Since Bernoulli's equation Eq. (24) states that the aerodynamic loads $\boldsymbol{F}$ depend on the square of the velocity (V_∞^2), the eigenvalue problem can be formulated as follows:

$$\begin{bmatrix} \hat{\boldsymbol{K}}_{\hat{q}\hat{q}}(\hat{\boldsymbol{q}}, \hat{\boldsymbol{\lambda}}) - \omega \hat{\boldsymbol{K}}^{ae}_{\hat{q}\hat{q}}(\hat{\boldsymbol{q}}; V_\infty) & \hat{\boldsymbol{H}}^T(\hat{\boldsymbol{q}}) \\ \hat{\boldsymbol{H}}(\hat{\boldsymbol{q}}) & \boldsymbol{0} \end{bmatrix} \cdot \begin{bmatrix} \Delta\hat{\boldsymbol{q}} \\ \Delta\hat{\boldsymbol{\lambda}} \end{bmatrix} = \boldsymbol{0} \tag{77}$$

with $\omega \in \mathbb{C}$ can be characterized in terms of V_∞ by $\omega = (V_c/V_\infty)^2$. As our structural model operates with director-based kinematics (a primal-dual approach), it is convenient to transform Eq. (77) into the minimal solution space according to the null-space projection approach presented in [67] for the static case. We obtain the following reduced linear eigenvalue problem:

$$[\tilde{\boldsymbol{K}}(\hat{\boldsymbol{q}}, \hat{\boldsymbol{\lambda}}) - \tilde{\omega} \tilde{\boldsymbol{K}}^{ae}(\hat{\boldsymbol{q}}; V_\infty)] \cdot \Delta\Phi = \boldsymbol{0} \tag{78}$$

with $\tilde{\boldsymbol{K}}$ is the reduced structural tangent matrix, $\tilde{\boldsymbol{K}}^{ae}$ is the reduced tangent matrix due to the discrete aerodynamic forces, and $\tilde{\omega} \in \mathbb{C}$ is the eigenvalue corresponding to the reduced linear eigenvalue problem.

For the problem at hand, we solve Eq. (78) around the initial undeformed configuration (load step $T_n = 0$) by assuming a constant free-field velocity of $V_\infty = 1$ ft/s and an angle of attack $\alpha = 0°$. It should be noted that such an eigenvalue problem can be solved for any predeformed or prestressed configuration, thus showing the versatility of our approach in terms of structural conditions. When solving the eigenvalue problem, which is rooted in a homogeneous Cauchy–Euler equation, only the positive real eigenvalues have a physical interpretation since they indicate the presence of unstable modes. The first five positive eigenvalues and their corresponding critical velocities are listed in Table 4. The smallest one is decisive, as it represents the first singular point in the stability problem and corresponds to a divergence speed of $V_c = 252.2$ ft/s.

The second approach to numerically determine the divergence speed is to track the determinant of the Jacobian matrix and identify singular points by evaluating the condition $\det(\hat{\boldsymbol{K}}(\hat{\boldsymbol{q}}, \hat{\boldsymbol{\lambda}}); V_\infty)|_{n+1}^i = 0$. To this end, we consider a small perturbation in the angle of attack, $\alpha = 1 \cdot 10^{-8}$, a freestream velocity ranging from 50 to 260 ft/s, and a characteristic length $\Delta L = 12.25$ ft. All simulations are performed until a steady-state regime is reached. Therefore, unsteady effects in the aerodynamic tangent matrices associated with the wake convection and temporal changes in circulation can be neglected without affecting the precision of the procedure. Test calculations conducted without considering the linearized aerodynamic forces revealed significant challenges in converging to a reliable solution for the divergence speed. All important parameters for these static aeroelastic simulations are summarized in Table 5.

We examine the determinant of the iteration matrix for each velocity at each load step and each Newton iteration. The velocity at which the transition between stable and unstable equilibrium occurs represents a singularity point and is associated with divergence instability. To track the determinant of the Jacobian in a reasonable order of magnitude, we monitor its logarithmic form given by

Table 4 Natural eigenfrequencies in $\mathrm{rad}^2/\mathrm{s}^2$ and critical velocities in ft/s

No.	$\Re(\tilde{\omega})$	V_c in ft/s
1	$6.362 \cdot 10^4$	$2.522 \cdot 10^2$
2	$5.816 \cdot 10^5$	$7.626 \cdot 10^2$
3	$1.660 \cdot 10^6$	$1.288 \cdot 10^3$
4	$3.370 \cdot 10^6$	$1.836 \cdot 10^3$
5	$5.808 \cdot 10^6$	$2.410 \cdot 10^3$

Table 5 Simulation parameter used in nonlinear static aeroelastic simulations determining divergence speed

Parameter	Value	Unit
Characteristic length, ΔL	12.25	ft
Structural incremental time step, Δt_n^s	Δt_n^{ae}	s
Cutoff radius, δ	0.01	— —
Aeroelastic influence radius, r_L	30.1	ft
Angle of attack, α	$1.0 \cdot 10^{-8}$	°
Free-field velocity, V_∞	[50,260]	ft/s
Newton convergence tolerance, tol_N	$1 \cdot 10^{-6}$	— —

$$\eta(\det(\hat{\boldsymbol{K}})) = \operatorname{sign}(m)\Re(\log_{10}\det(\hat{\boldsymbol{K}})) = \operatorname{sign}(m)\Re(\log_{10} m 10^e) = \operatorname{sign}(m)(\log_{10}|m| + e) \tag{79}$$

where $m \in \mathbb{R}$ is the mantissa and $e \in \mathbb{Z}$ stands for the exponent with base 10 of the determinant of the iteration matrix. The diagram in Fig. 12 illustrates the evaluation of Eq. (79) for each free-field velocity V_∞. It shows that the first singular point occurs at a velocity of $V_\infty = V_c = 249.4$ ft/s and reveals that the static equilibrium configurations in simulations with velocities below the divergence speed exhibit stable equilibrium, i.e., $\det(\hat{\boldsymbol{K}}) > 0$. Differently, calculations with velocities above the critical speed result in unstable equilibrium configurations, i.e., $\det(\hat{\boldsymbol{K}}) \leq 0$, leading to the divergence of the simulations. The transition from stable to unstable equilibrium is captured in Fig. 13, which evaluates the minimum magnitude of Eq. (79). In Table 6, we compare the calculated divergence speeds obtained from our numerical model and the

Table 6 Summary of calculated divergence speeds

Method	V_c, ft/s	Relative error, %
Analytically [Eq. (76)]	252.0	— —
Linear generalized eigenvalue problem [Eq. (78)]	252.2	0.08
Fully nonlinear static aeroelastic analysis	249.4	1.03

analytical solution of the homogeneous differential equation. The results show excellent agreement, with a maximal deviation of 1%. Solving the nonlinear static aeroelastic equations requires applying a series of small geometrical perturbations. As the system approaches a bifurcation point, geometric nonlinearities affect the structural and aerodynamic contributions to the structural stiffness, thereby affecting the divergence speed. In this sense, this approach yields a more accurate estimation of the divergence speed.

3. *Static Aeroelasticity: Deformation Analysis*

In this subsection, we present a nonlinear static aeroelastic deformation analysis of the bridge deck subject to an inflow at an angle of attack $\alpha = 10°$ and a freestream velocity $V_\infty = 600$ ft/s. The goal is to examine the convergence behavior of our proposed linearization framework within the context of nonlinear static aeroelasticity, particularly concerning large displacements and rotations. The aeroelastic divergence speed for $\alpha = 10°$ is approximately $V_c = 259.4$ ft/s ($< V_\infty$). To simulate large displacements and rotations while maintaining the conditions where the UVLM remains applicable, we have increased the initial beam torsional stiffness to $GA = 1.47 \cdot 10^{13}$ lbf. This adjustment elevates the critical speed to a larger value ($V_c = 2527.4$ ft/s). Furthermore, we employ a linear factorization of the vector of generalized aerodynamic forces for an impulsive start

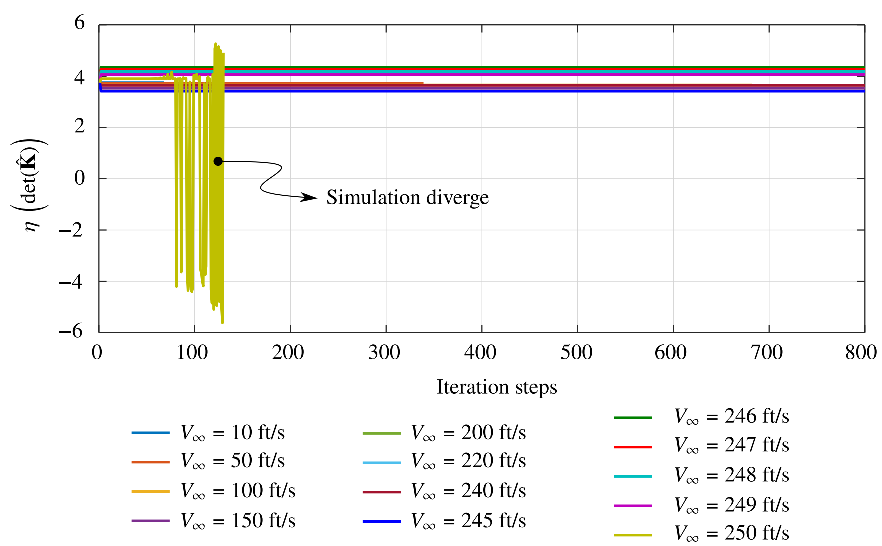

Fig. 12 Evaluation of Eq. (79) for each V_∞.

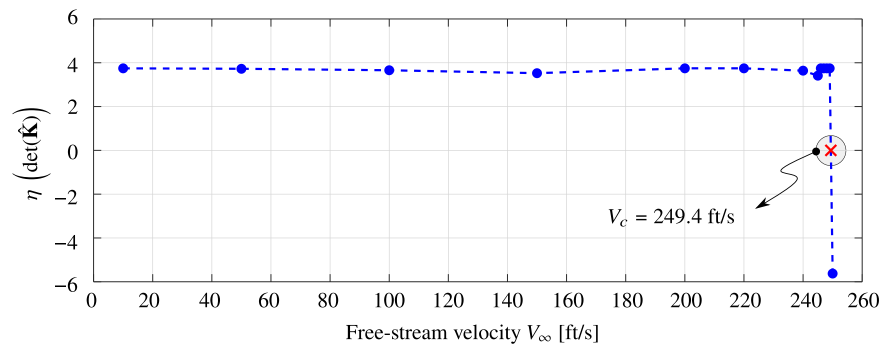

Fig. 13 Transition from stable to unstable equilibrium.

Table 7 Simulation parameter used in nonlinear static aeroelastic deformation analysis

Parameter	Value	Unit
Total number of load steps, T_n	200.0	——
Characteristic length, ΔL	12.25	ft
Cutoff radius, δ	0.01	——
Aeroelastic influence radius, r_L	30.1	ft
Angle of attack, α	10.0	°
Intensity of free-field velocity, V_∞	600	ft/s
Newton convergence tolerance, tol_N	$1 \cdot 10^{-10}$	——

Table 8 Displacements and rotations in steady state

Parameter	Value	Unit
u_1	−17.80	ft
u_2	1.29	ft
u_3	175.83	ft
ϕ_1	−0.74	°
ϕ_2	−13.41	°
ϕ_3	0.02	°

Table 9 Reaction forces and moments in steady state

Parameter	Value	Unit
F_1	$-4.35 \cdot 10^6$	lbf
F_2	$2.15 \cdot 10^5$	lbf
F_3	$2.38 \cdot 10^7$	lbf
M_1	$-3.80 \cdot 10^8$	ft-lbf
M_2	$-1.21 \cdot 10^{10}$	ft-lbf
M_3	$6.30 \cdot 10^7$	ft-lbf

of free-field velocity to improve the convergence behavior at the beginning of the nonlinear calculation. Specifically, we linearly increase the magnitude of the aerodynamic forces until reaching load step $T_d = 50$. Afterward, the forces are consistently applied without alteration throughout the remaining simulation. The simulation runs up to $T_n = 200$ steps to ensure a steady-state solution. All simulation parameters are listed in Table 7.

The results of the steady-state displacements and rotations are summarized in Table 8. Given that our director-based approach does not yield the rotation parameters directly, we ascertain the rotations through the cumulative summation of incremental rotations at each time step [69]. It can be observed that the cantilever beam undergoes a deflection of 17.6% compared with its length, with a maximal vertical displacement of 175.83 ft and a torsion of 0.74°. The steady-state values for the reaction forces and moments at the fixed end of the cantilever beam are summarized in Table 9. To assess the computational performance of our approach, we analyze the convergence behavior while solving the nonlinear governing equations and compare the solution obtained from solving the fully linearized equilibrium equations (full Newton's method) with the solution obtained with the quasi-Newton's method, which neglects the linearization of the vector of generalized aerodynamic forces. Figure 14 illustrates the number of required iteration steps until reaching the convergence tolerance. It can be observed that, overall, the full Newton's method requires fewer iteration steps to converge compared to the quasi-Newton's method. In simulation steps where high deformation gradients occur (step 50), the quasi-Newton's method requires a maximum of 19 iterations. In comparison, the full Newton's method only requires, on average, four iterations. This results in a total of 802 iterations for the full Newton's method and 3437 iterations for the quasi-Newton's method (see Fig. 15), representing an 80% improvement in the number of iteration steps. Figure 16 displays the relative residuum of $\boldsymbol{g}$. The diagram clearly shows that in the almost steady state (steps 150–200), the number of iterations for the full Newton's method is reduced to three, while the quasi-Newton's method still requires 17 iterations.

4. *Dynamic Aeroelasticity: Flutter Analysis*

Flutter is another aeroelastic stability phenomenon that is characterized by self-sustained oscillations involving interaction among the

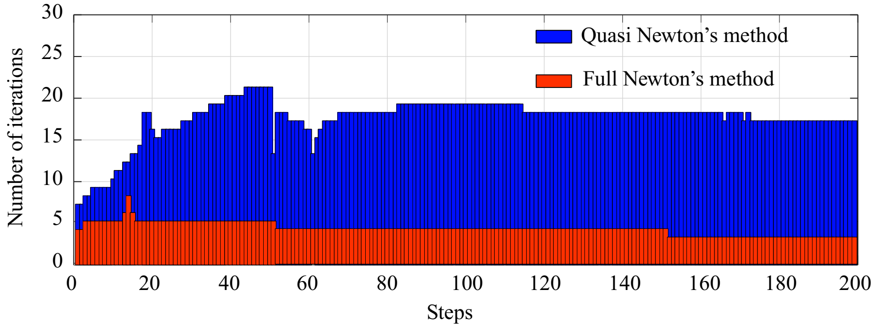

Fig. 14 Number of convergence iterations per time step.

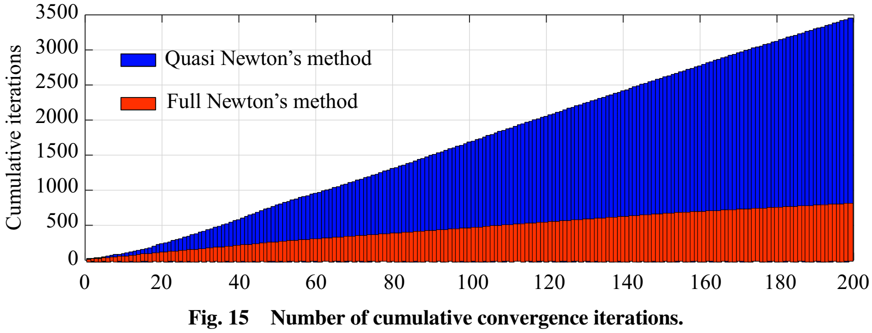

Fig. 15 Number of cumulative convergence iterations.

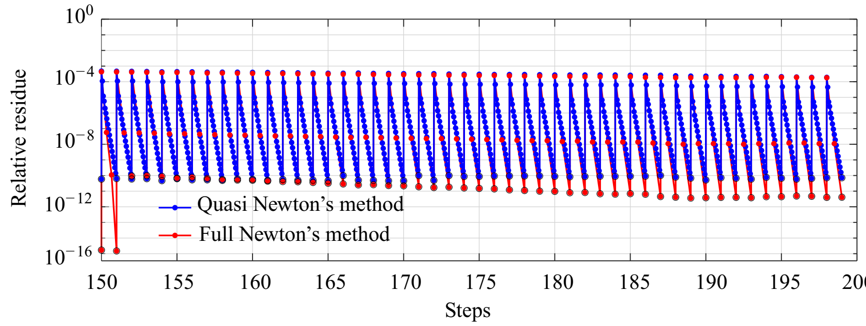

Fig. 16 Relative residuum of static equilibrium.

inertia, elastic and damping forces present at the vibrating structure, and aerodynamic forces acting on the associated lifting surface. To verify our framework under subcritical, critical, and super-critical conditions, we reproduce the problem initially analyzed by [72]. As mentioned, Fung computes the aeroelastic stability problem by means of a simplified analytical model. A more complex model of that bridge can be found in [18]. Those authors also present an aeroelastic model combining the FEM with the UVLM. The finite element model consists of nonlinear Bernoulli finite beam elements reduced by employing an assumed-modes approach. The discrete governing equations of the aeroelastic model are solved numerically using Hamming's fourth-order modified time integration scheme. In the subsequent discussion, we present two ways of calculating the flutter velocity V_F by using the current approach.

First, we determine V_F by solving a quadratic generalized eigenvalue problem derived from the linearized aeroelastic governing equations Eq. (65). As mentioned above, analyzing the algebraic nature of the linearized equations in a director-based approach requires operating in a minimal solution space, which is obtained by applying the null-space projection approach presented in [66] for the dynamic case. Without any loss of generality, we obtain the following reduced quadratic generalized eigenvalue problem for any equilibrium state (with $\hat{\boldsymbol{s}} = \dot{\hat{\boldsymbol{q}}}$):

$$[\tilde{\boldsymbol{K}}_{\hat{q}\hat{q}}(\hat{\boldsymbol{q}}, \hat{\boldsymbol{\lambda}}) - \tilde{\boldsymbol{K}}^{ae}_{\hat{q}\hat{q}}(\hat{\boldsymbol{q}}, \dot{\hat{\boldsymbol{q}}}; V_\infty) - \tilde{\omega}\tilde{\boldsymbol{K}}^{ae}_{\hat{q}\hat{s}}(\hat{\boldsymbol{q}}; \dot{\hat{\boldsymbol{q}}}; V_\infty) + \tilde{\omega}^2 \tilde{\boldsymbol{K}}_{\hat{q}\hat{s}}] \cdot \Delta\Phi = \boldsymbol{0} \tag{80}$$

where $\tilde{\boldsymbol{K}}_{\hat{q}\hat{q}}$ is the reduced structural tangent matrix of the discrete generalized internal forces, $\tilde{\boldsymbol{K}}^{ae}_{\hat{q}\hat{q}}$ and $\tilde{\boldsymbol{K}}^{ae}_{\hat{q}\hat{s}}$ are the reduced tangent matrices due to the discrete generalized aerodynamic forces, $\tilde{\boldsymbol{K}}_{\hat{q}\hat{s}}$ is the reduced tangent matrices of the discrete generalized inertia forces (see [78]), and $\tilde{\omega} \in \mathbb{C}$ is the eigenvalue corresponding to the reduced quadratic generalized eigenvalue problem. Here, $\Re(\tilde{\omega})$ characterizes the aerodynamic damping, and $\Im(\tilde{\omega})$ is the system's oscillatory eigenfrequency. Naturally, we ascertain V_F as the freestream velocity at which $\Re(\tilde{\omega}) = 0$, defining the transition between stable and unstable aeroelastic regimes. The procedure for identifying V_F requires to solve Eq. (80) across a range of freestream velocities, here $V_\infty = \{120, 140, 160, 170\}$ ft/s. Figure 17 illustrates the variation of the eigenvalues for the first five eigenvectors as a function of the freestream velocity. The upper chart reveals that the first transition from a stable to an unstable region occurs for the first torsional mode at a freestream velocity of $V_F = 164.7$ ft/s (interpolated). The corresponding torsional eigenfrequency is given by $\omega_F = 1.26$ rad/s (see Fig. 17, lower diagram).

Another way and more accurate one to compute V_F is to perform full transient calculations solving the nonlinear aeroelastic equations Eq. (64) for several freestream velocities. Then, V_F can be identified as the velocity at which the first bending and first torsional eigenvalues coincide. The magnitude of the investigated free-field velocities is chosen in the validity of the UVLM, and the wake will be only shed from the trailing edge. To excite the flutter motion, the bridge deck is initially predeformed in a torsion angle $\phi_1 = 10°$ at the free end of the cantilever beam. Each simulation runs with a total simulation time of $T = 600.0$ s. The incremental time Δt^{ae}, which drives the aerodynamic load computation, is chosen such that at each time instant, the wake nodes are approximately convected with the order of magnitude close to the characteristic length $\Delta L = \sqrt{(cL/n^{ae}m^{ae})} = 12.25$ ft. Singularity effects due to the vortex-induced velocities are mitigated considering a cutoff $\delta = 0.01$. Moreover, no structural damping is assumed to obtain the largest lower bound of the flutter speed. The simulation data are listed in Table 10.

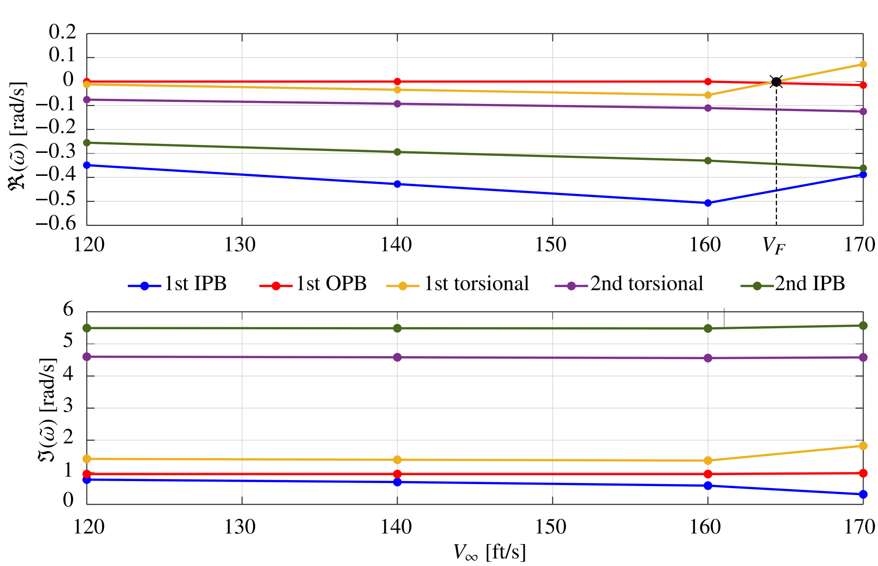

Fig. 17 $\Re(\tilde{\omega})$ and $\Im(\tilde{\omega})$ vs free-field velocities.

Table 10 Simulation parameter used in nonlinear dynamic aeroelastic analyses

Parameter	Value	Unit
Total simulation time, T	600.0	s
Characteristic length, ΔL	12.25	ft
Cutoff radius, δ	0.01	— —
Aeroelastic-influence radius, r_L	30.1	ft
Initial torsion, ϕ_1	10.0	°
Intensity of free-field velocity, V_∞	[120, 200]	ft/s
Newton convergence tolerance, tol_N	$1 \cdot 10^{-6}$	— —

The frequencies are obtained by transforming the flapwise and torsional responses into their frequency spectra using Fourier's transformation. Figure 18 shows that the flapwise and torsional frequencies merge at $V_F = 162$ ft/s, and their corresponding frequency is $\omega_F = 1.27$ rad/s.

Table 11 provides a comparison of our results with those obtained by Gebhardt and Roccia [18] and Fung [72]. Using the results presented by Fung as a reference, our findings show excellent agreement. The slight difference in the frequency can be attributed to the different mechanical models, as commented previously. The model presented by Fung is the simplest, representing the bridge as a reduced-order two-dimensional system with linear springs. It captures only coupled pitching and transversal motion and does not account for other modes or any further unsteady interactions. The model by Gebhardt and Roccia employs nonshearable finite elements and a quasi-modal order reduction to represent the slow bending and torsional motions. While it allows for large nonlinear motions and unsteady nonlinear aerodynamic behavior, it is not able to deal with moderate or large nonlinear deformations. In contrast, our structural model is not limited to specific modes or motions. It is based on a three-dimensional geometrically exact beam theory that considers large rotations and displacements as well as nonlinear deformations. This allows for a more comprehensive representation of the aeroelastic behavior.

The structural displacement signals in subcritical (at $V_\infty = 120$ ft/s), critical (at $V_\infty = 162$ ft/s), and super-critical (at $V_\infty = 170$ ft/s) conditions are presented in Fig. 19. For the sake of clarity, we present the data for the first 300 s. The corresponding phase diagrams are shown in Fig. 20. From these results, we can draw several conclusions:

At the subcritical velocity of $V_\infty = 120$ ft/s, the bridge deck exhibits small amplitude oscillations. The displacement history shows a damped vibrating motion, where the oscillations exponentially diminish over time. The phase diagram depicts a stable response tending towards zero. For all velocities below the critical velocity, the total structural energy sinks, which means that the flow takes energy from the structure. At the critical velocity of $V_\infty = 162$ ft/s, the bridge deck enters into a limit cycle oscillation (LCO). The bending and torsional frequencies have merged into a single frequency, and the displacement history exhibits sustained oscillations with a constant energy level. At all velocities exceeding the critical velocity, the fluid acts as an energy source, transferring energy to the structure. The magnitude of this energy transfer depends on the inflow velocity, leading to a substantial increase in the motion's amplitude.

Table 11 Summary of flutter velocity and flutter frequency

Method/source	V_c, ft/s	Relative error of V_c, %	ω_F, rad/s	Relative error of ω_F, %
Fung [72]	162.0	— —	1.25	— —
Gebhardt and Roccia [18]	161.0	0.62	1.29	3.20
Eigenvalue problem [Eq. (80)]	164.7	1.67	1.26	0.80
Aeroelastic simulations [Eq. (64)]	162.0	0.00	1.27	1.60

Figure 21 presents a comparison of the number of iterations required for the simulation with and without linearized aerodynamic forces, considering the case of $V_\infty = 120$ ft/s. As expected, it can be observed that the simulation with linearized aerodynamic forces significantly reduces the number of iterations compared to the simulation with incomplete linearization. Specifically, the total cumulative number of iterations decreases from 8644 iterations to 6826 iterations, resulting in a reduction of ≈21%.

Through the nonlinear simulations, we have observed that our proposed approach exhibits robust solution behavior when solving the governing equations without encountering any convergence issues in the conducted simulations. It should be noted that calculating the aerodynamic tangent matrices according Algorithm 1 incurs an increased computational effort. To briefly address this issue, we suggest employing complete code parallelization to perform multiple operations simultaneously (OMP and MPI), sparse implementations, and model-specific improvements, e.g., effectively clustering the aerodynamic model by applying multilevel fast-multipole algorithms [63,79,80]. Furthermore, adaptive solutions and time control techniques can be employed as well to decrease the computational effort. However, the efficient implementation is beyond the scope of this work, and therefore, this is not addressed here but planned for future work.

V. Conclusions

This paper presents the analytical linearization of aerodynamic loads (computed with the unsteady vortex-lattice method), which is formulated as tangent matrices with respect to the kinematic states of the aerodynamic grid. The corresponding aerodynamic loads and their linearization were mapped to a fully nonlinear structural model by means of a procedure for data transfer, while the kinematic description of the aerodynamic model was parameterized in terms of the kinematic description of the structural model. This enabled us to set up a bidirectional, strong interaction scheme for the resulting aeroelastic model. The structural model adopted considers geometrically exact beams that rely on a director-based total Lagrangian description, allowing for exact preservation of objectivity and path independence at the continuous/discrete levels, even after the spatial discretization with the finite element method. The resulting semi-discrete equations of motion were discretized in time by means of an

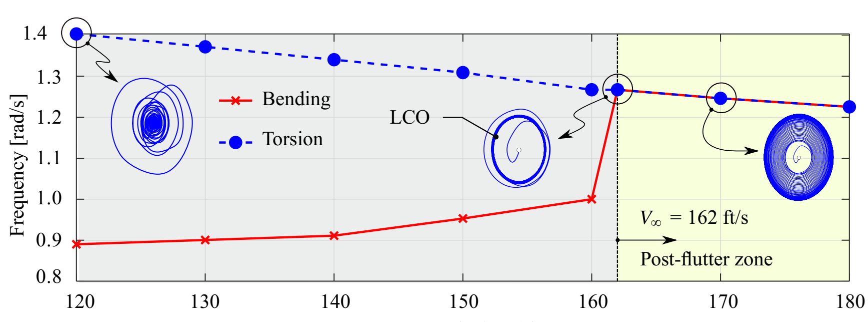

Fig. 18 First torsional and first bending eigenfrequencies vs freestream velocity.

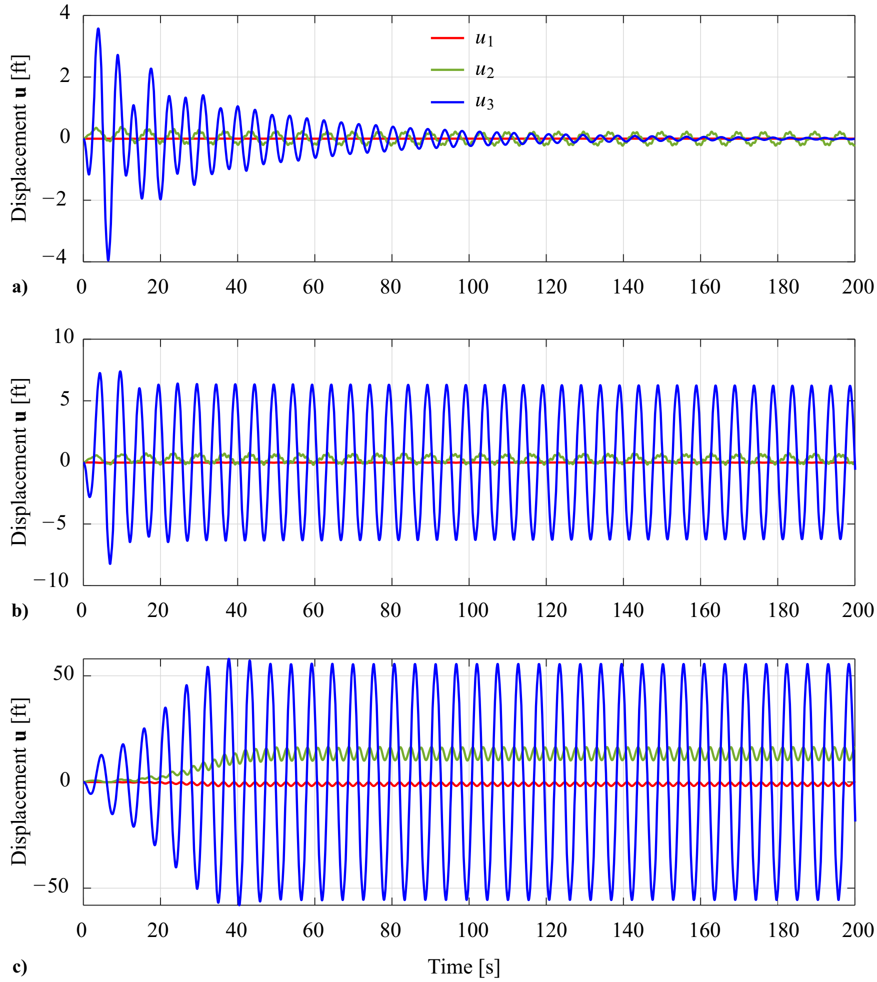

Fig. 19 Free-end displacements of the cantilever beam for freestream velocities: a) $V_\infty = 120$ ft/s, b) $V_\infty = 162$ ft/s, and c) $V_\infty = 200$ ft/s.

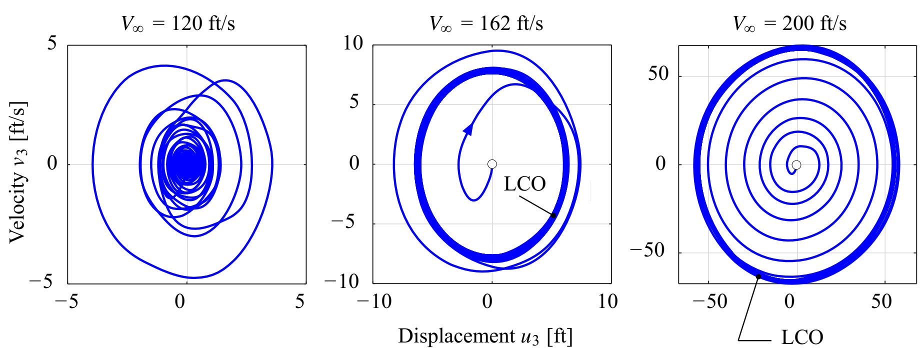

Fig. 20 Phase diagrams ($\bar{v}_3$ vs $\bar{u}_3$) at free end of the cantilever.

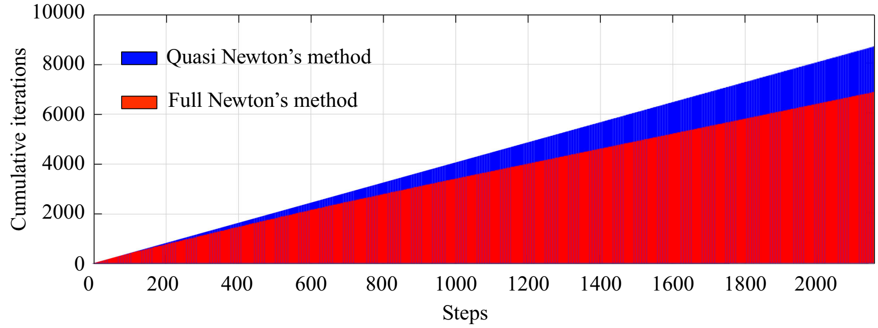

Fig. 21 Number of cumulative convergence iterations for $V_\infty = 120$ ft/s.

implicit time integration scheme based on discrete derivatives, which preserves identically momenta and energy. We showed the correctness of the linearized loads by comparing them against those obtained numerically. In addition, we employed fully coupled aerodynamic and structural models to investigate the static and dynamic nonlinear aeroelastic behavior of a suspension bridge. In this way, we investigated the excellent numerical features of the aeroelastic model as well as the divergence and flutter behavior that were also verified against results available in the literature.

Overall, this paper contributes to the further development of a midfidelity aeroelastic framework capable of capturing geometric nonlinearities present in both the aerodynamic and structural models. Nevertheless, the results presented here are just a solid starting point for more interdisciplinary applications requiring gradient-based methods. Therefore, our approach may have a large range of applicability within aeroservoelasticity and aeroelastic optimal design, just to name a few areas of research.

Acknowledgments

This study has been partially carried out within the DFG-collaboration *SFB 1463—Offshore Megastructures—"Integrated Design and Operation Methodology for Offshore Megastructures,"* financially supported by the Deutsche Forschungsgemeinschaft (DFG, German Research Foundation; Project-ID 434502799). C. Gebhardt and B. Roccia gratefully acknowledge the support from the European Research Council through the ERC Consolidator Grant "DATA-DRIVEN OFFSHORE" (Project ID 101083157).

References

[1] Voß, A., Handojo, V., Niemann, S., and Weiser, C., "Results from Loads and Aeroelastic Analyses of a High Altitude, Long Endurance, Solar Electric Aircraft," *Journal of Aeroelasticity and Structural Dynamics*, Vol. 8, No. 2, 2022, pp. 1–22.
https://doi.org/10.1109/taes.2018.2836598

[2] Shafaghat, S., Noorian, M., and Irani, S., "Nonlinear Aeroelastic Analysis of a HALE Aircraft with Flexible Components," *Aerospace Science and Technology*, Vol. 127, Aug. 2022, Paper 107663.
https://doi.org/10.1016/j.ast.2022.107663

[3] Dayhoum, A., Zakaria, M., and Abdelhamid, O., "Unsteady Aerodynamic Modeling and Analysis of Load Distribution for Helicopter Rotor Blades," *Journal of Aerospace Engineering*, Vol. 35, No. 1, 2022, Paper 04021106.
https://doi.org/10.1061/(asce)as.1943-5525.0001355

[4] Afonso, F., Coelho, M., Vale, J., Lau, F., and Suleman, A., "On the Design of Aeroelastically Scaled Models of High Aspect-Ratio Wings," *Aerospace*, Vol. 7, No. 11, 2020, p. 166.
https://doi.org/10.3390/aerospace7110166

[5] Bras, M., Warwick, S., and Suleman, A., "Aeroelastic Evaluation of a Flexible High Aspect Ratio Wing UAV: Numerical Simulation and Experimental Flight Validation," *Aerospace Science and Technology*, Vol. 122, March 2022, Paper 107400.
https://doi.org/10.1016/j.ast.2022.107400

[6] Hansen, M., "Aeroelastic Instability Problems for Wind Turbines," *Wind Energy: An International Journal for Progress and Applications in Wind Power Conversion Technology*, Vol. 10, No. 6, 2007, pp. 551–577.
https://doi.org/10.1002/we.242

[7] Hach, O., Verdonck, H., Polman, J., Balzani, C., Müller, S., Rieke, J., and Hennings, H., "Wind Turbine Stability: Comparison of State-of-the-Art Aeroelastic Simulation Tools," *Journal of Physics: Conference Series*, Vol. 1618, No. 5, 2020, Paper 052048.
https://doi.org/10.1088/1742-6596/1618/5/052048

[8] Wu, T., and Kareem, A., "Aerodynamics and Aeroelasticity of Cable-Supported Bridges: Identification of Nonlinear Features," *Journal of Engineering Mechanics*, Vol. 139, No. 12, 2013, pp. 1886–1893.
https://doi.org/10.1061/(asce)em.1943-7889.0000615

[9] Abbas, T., Kavrakov, I., and Morgenthal, G., "Methods for Flutter Stability Analysis of Long-Span Bridges: A Review," *Proceedings of the Institution of Civil Engineers-Bridge Engineering*, Vol. 170, No. 4, 2017, pp. 271–310.
https://doi.org/10.1680/jbren.15.00039

[10] Felippa, C., and Park, K.-C., "Staggered Transient Analysis Procedures for Coupled Mechanical Systems: Formulation," *Computer Methods in Applied Mechanics and Engineering*, Vol. 24, No. 1, 1980, pp. 61–111.
https://doi.org/10.1016/0045-7825(80)90040-7

[11] Stanford, B. K., and Beran, P. S., "Analytical Sensitivity Analysis of an Unsteady Vortex-Lattice Method for Flapping-Wing Optimization," *Journal of Aircraft*, Vol. 47, No. 2, 2010, pp. 647–662.
https://doi.org/10.2514/1.46259

[12] Gebhardt, C., Preidikman, S., and Massa, J., "Numerical Simulations of the Aerodynamic Behavior of Large Horizontal-Axis Wind Turbines," *International Journal of Hydrogen Energy*, Vol. 35, No. 11, 2010, pp. 6005–6011.
https://doi.org/10.1016/j.ijhydene.2009.12.089

[13] Roccia, B., Preidikman, S., Massa, J., and Mook, D., "Modified Unsteady Vortex-Lattice Method to Study Flapping Wings in Hover Flight," *AIAA Journal*, Vol. 51, No. 11, 2013, pp. 2628–2642.
https://doi.org/10.2514/1.J052262

[14] Verstraete, M., Preidikman, S., Roccia, B., and Mook, D., "A Numerical Model to Study the Nonlinear and Unsteady Aerodynamics of Bioinspired Morphing-Wing Concepts," *International Journal of Micro Air Vehicles*, Vol. 7, No. 3, 2015, pp. 327–345.
https://doi.org/10.1260/1756-8293.7.3.327

[15] Pérez Segura, M., Mook, D., and Preidikman, S., "General-Purpose Object-Oriented Framework for Vorticity-Dominated Flow Simulation," *Journal of Aerospace Information Systems*, Vol. 17, No. 10, 2020, pp. 562–580.
https://doi.org/10.2514/1.i010818

[16] Verstraete, M., Ceballos, L., Hente, C., Roccia, B., and Gebhardt, C., "Code-to-Code Benchmark for Simulation Tools Based on the Unsteady Vortex-Lattice Method," *Journal of Aerospace Information Systems*, Vol. 20, No. 11, 2023, pp. 719–746.
https://doi.org/10.2514/1.i011184

[17] Ghommem, M., Abdelkefi, A., Nuhait, A., and Hajj, M., "Aeroelastic Analysis and Nonlinear Dynamics of an Elastically Mounted Wing," *Journal of Sound and Vibration*, Vol. 331, No. 26, 2012, pp. 5774–5787.
https://doi.org/10.1016/j.jsv.2012.07.040

[18] Gebhardt, C., and Roccia, B., "Non-Linear Aeroelasticity: An Approach to Compute the Response of Three-Blade Large-Scale Horizontal-Axis Wind Turbines," *Renewable Energy*, Vol. 66, June 2014, pp. 495–514.
https://doi.org/10.1016/j.renene.2013.12.040

[19] Roccia, B., Preidikman, S., and Balachandran, B., "Computational Dynamics of Flapping Wings in Hover Flight: A Co-Simulation Strategy," *AIAA Journal*, Vol. 55, No. 6, 2017, pp. 1806–1822.
https://doi.org/10.2514/1.j055137

[20] Roccia, B., Verstraete, M., Ceballos, L., Balachandran, B., and Preidikman, S., "Computational Study on Aerodynamically Coupled Piezoelectric Harvesters," *Journal of Intelligent Material Systems and Structures*, Vol. 31, No. 13, 2020, pp. 1578–1593.
https://doi.org/10.1177/1045389x20930093

[21] Verstraete, M., Roccia, B., Mook, D., and Preidikman, S., "A Co-Simulation Methodology to Simulate the Nonlinear Aeroelastic Behavior of a Folding-Wing Concept in Different Flight Configurations," *Nonlinear Dynamics*, Vol. 98, Oct. 2019, pp. 907–927.
https://doi.org/10.1007/s11071-019-05234-9

[22] Beltramo, E., Pérez Segura, M., Roccia, B., Valdez, M., Verstraete, M., and Preidikman, S., "Constructive Aerodynamic Interference in a Network of Weakly Coupled Flutter-Based Energy Harvesters," *Aerospace*, Vol. 7, No. 12, 2020, p. 167.
https://doi.org/10.3390/aerospace7120167

[23] Tavares Pereira dos Santos, J., Begnini, G., and Marques, F., "Time Domain Aeroelastic Analysis of Clamped Wings and Determination of VGP Plots," *Revista Mundi Engenharia, Tecnologia e Gestão (ISSN: 2525-4782)*, Vol. 8, No. 1, 2023.
https://doi.org/10.2514/6.2006-1640

[24] Kleppenes, E., "Development of Advanced Tools in Computational Nonlinear Aeroelasticity," Master's Thesis, Geophysical Inst. and Bergen Offshore Wind Centre (BOW), Univ. of Bergen, Bergen, Norway, 2023.

[25] Shabana, A., "Flexible Multibody Dynamics: Review of Past and Recent Developments," *Multibody System Dynamics*, Vol. 1, June 1997, pp. 189–222.
https://doi.org/10.1007/bf02916141

[26] Shabana, A., *Dynamics of Multibody Systems*, Cambridge Univ. Press, Cambridge, England, U.K., 2020.

[27] Simo, J., and Vu-Quoc, L., "On the Dynamics in Space of Rods Undergoing Large Motions–A Geometrically Exact Approach," *Computer Methods in Applied Mechanics and Engineering*, Vol. 66, No. 2, 1988, pp. 125–161.
https://doi.org/10.1016/0045-7825(88)90073-4

[28] Cardona, A., and Geradin, M., "A Beam Finite Element Non-Linear Theory with Finite Rotations," *International Journal for Numerical Methods in Engineering*, Vol. 26, No. 11, 1988, pp. 2403–2438.
https://doi.org/10.1002/nme.1620261105

[29] Gebhardt, C., and Rolfes, R., "On the Nonlinear Dynamics of Shell Structures: Combining a Mixed Finite Element Formulation and a Robust Integration Scheme," *Thin-Walled Structures*, Vol. 118, Sept. 2017, pp. 56–72.
https://doi.org/10.1016/j.tws.2017.05.001

[30] Gebhardt, C., Hofmeister, B., Hente, C., and Rolfes, R., "Nonlinear Dynamics of Slender Structures: A New Object-Oriented Framework," *Computational Mechanics*, Vol. 63, Feb. 2018, pp. 219–252.
https://doi.org/10.1007/s00466-018-1592-7

[31] Gebhardt, C., Romero, I., and Rolfes, R., "A New Conservative/Dissipative Time Integration Scheme for Nonlinear Mechanical Systems," *Computational Mechanics*, Vol. 65, No. 2, 2020, pp. 405–427.
https://doi.org/10.1007/s00466-019-01775-3

[32] Mauermann, T., "Flexible Aircraft Modelling for Flight Loads Analysis of Wake Vortex Encounters," Ph.D. Thesis, DLR, Bibliotheks-und Informationswesen, Cologne, Germany, 2010.

[33] Murua, J., Palacios, R., and Graham, J., "Applications of the Unsteady Vortex-Lattice Method in Aircraft Aeroelasticity and Flight Dynamics," *Progress in Aerospace Sciences*, Vol. 55, Nov. 2012, pp. 46–72.
https://doi.org/10.1016/j.paerosci.2012.06.001

[34] Hesse, H., Palacios, R., and Murua, J., "Consistent Structural Linearization in Flexible Aircraft Dynamics with Large Rigid-Body Motion," *AIAA Journal*, Vol. 52, No. 3, 2014, pp. 528–538.
https://doi.org/10.2514/1.j052316

[35] Hesse, H., and Palacios, R., "Reduced-Order Aeroelastic Models for Dynamics of Maneuvering Flexible Aircraft," *AIAA Journal*, Vol. 52, No. 8, 2014, pp. 1717–1732.
https://doi.org/10.2514/1.j052684

[36] Hilger, J., and Ritter, M., "Nonlinear Aeroelastic Simulations and Stability Analysis of the Pazy Wing Aeroelastic Benchmark," *Aerospace*, Vol. 8, No. 10, 2021, p. 308.
https://doi.org/10.3390/aerospace8100308

[37] Maraniello, S., and Palacios, R., "State-Space Realizations and Internal Balancing in Potential-Flow Aerodynamics with Arbitrary Kinematics," *AIAA Journal*, Vol. 57, No. 6, 2019, pp. 2308–2321.
https://doi.org/10.2514/1.j058153

[38] Maraniello, S., and Palacios, R., "Parametric Reduced-Order Modeling of the Unsteady Vortex-Lattice Method," *AIAA Journal*, Vol. 58, No. 5, 2020, pp. 2206–2220.
https://doi.org/10.2514/1.J058894

[39] Roccia, B., Verstraete, M., Dimitriadis, G., Bruls, O., and Preidikman, S., "Unsteady Aerodynamics and Nonlinear Dynamics of Freefalling Rotating Seeds," *International Conference on Noise and Vibration Engineering, ISMA 2018*, KUL, Leuven, Belgium, 2018.
https://doi.org/10.2514/2.1853

[40] Maza, M., Preidikman, S., and Flores, F. G., "A Cost-Effective Algorithm for the Co-Simulation of Unsteady and Non-Linear Aeroelastic Phenomena," *Journal of Fluids and Structures*, Vol. 118, April 2023, Paper 103838.
https://doi.org/10.1016/j.jfluidstructs.2023.103838

[41] Katz, J., and Plotkin, A., *Low-Speed Aerodynamics*, Vol. 13, Cambridge Univ. Press, Cambridge, England, U.K., 2001, p. 11.

[42] Karamcheti, K., *Principles of Ideal Fluid Aerodynamics*, Kreiger Publ., FL, 1966, pp. 54–55.

[43] Bhatia, H., Norgard, G., Pascucci, V., and Bremer, P.-T., "The Helmholtz-Hodge Decomposition—A Survey," *IEEE Transactions on Visualization and Computer Graphics*, Vol. 19, No. 8, 2012, pp. 1386–1404.
https://doi.org/10.1109/tvcg.2012.316

[44] McDonald, K. T., *The Helmholtz Decomposition and the Coulomb Gauge*, Joseph Henry Lab., Princeton Univ., Princeton, NJ, Vol. 8544, 2020, pp. 1–13.
https://doi.org/10.1017/cbo9781107785281.005

[45] Lee, C.-S., "Predicton of Steady and Unsteady Performance of Marine Propellers with or Without Cavitation by Numerical Lifting-Surface Theory," Ph.D. Dissertation, Massachusetts Inst. of Technology, Cambridge, MA, 1979.

[46] D'Alascio, A., Visingardi, A., and Renzoni, P., "Explicit Kutta Condition Correction for Rotary Wing Flows," *Proceedings of the 19th World Conference on the Boundary Element Method*, Wessex Inst. of Technology, Rome, Italy, 1997.
https://doi.org/10.1016/s0093-6413(98)00054-8

[47] Giesing, J., "Vorticity and Kutta Condition for Unsteady Multienergy Flows," *ASME Journal of Applied Mechanics*, Vol. 36, No. 3, 1969, pp. 608–613.
https://doi.org/10.1115/1.3564724

[48] von Karman, T., and Sears, W., "Airfoil Theory for Non-Uniform Motion," *Journal of the Aeronautical Sciences*, Vol. 5, No. 10, 1938, pp. 379–390.
https://doi.org/10.2514/8.674

[49] Van de Vooren, A., and Van de Vel, H., "Unsteady Profile Theory in Incompressible Flow," *Fluid Dynamics Transactions*, Elsevier, New York, 1965, pp. 477–503.
https://doi.org/10.1016/b978-0-08-011860-4.50036-7

[50] Katz, J., and Maskew, B., "Unsteady Low-Speed Aerodynamic Model for Complete Aircraft Configurations," *Journal of Aircraft*, Vol. 25, No. 4, 1988, pp. 302–310.
https://doi.org/10.2514/6.1986-2180

[51] Preidikman, S., "Numerical Simulations of Interactions Among Aerodynamics," Ph.D. Dissertation, Dept. of Engineering Science and Mechanics, Virginia Polytechnic Inst. and State Univ., Blacksburg, VA, 1998.

[52] Nguyen, A. T., Kim, J.-K., Han, J.-S., and Han, J.-H., "Extended Unsteady Vortex-Lattice Method for Insect Flapping Wings," *Journal of Aircraft*, Vol. 53, No. 6, 2016, pp. 1709–1718.
https://doi.org/10.2514/1.c033456

[53] Phillips, W., and Snyder, D., "Modern Adaptation of Prandtl's Classic Lifting-Line Theory," *Journal of Aircraft*, Vol. 37, No. 4, 2000, pp. 662–670.
https://doi.org/10.2514/2.2649

[54] Mook, D., and Maddox, S., "Extension of a Vortex-Lattice Method to Include the Effects of Leading-Edge Separation," *Journal of Aircraft*, Vol. 11, No. 2, 1974, pp. 127–128.
https://doi.org/10.2514/3.60336

[55] Konstadinopoulos, P., Thrasher, D., Mook, D., Nayfeh, A., and Watson, L., "A Vortex-Lattice Method for General, Unsteady Aerodynamics," *Journal of Aircraft*, Vol. 22, No. 1, 1985, pp. 43–49.
https://doi.org/10.2514/3.45078

[56] Katz, J., "A Discrete Vortex Method for the Non-Steady Separated Flow over an Airfoil," *Journal of Fluid Mechanics*, Vol. 102, Jan. 1981, pp. 315–328.
https://doi.org/10.1017/s0022112081002668

[57] Chorin, A., *Vorticity and Turbulence*, Springer–Verlag, New York, 1994, p. 8.

[58] Van Garrel, A., "Development of a Wind Turbine Aerodynamics Simulation Module," ECN-C–03-079, Energy Research Centre, The Netherlands, 2003.
https://doi.org/10.1002/pamm.200700521

[59] Grasso, F., van Garrel, A., and Schepers, G., "Development and Validation of Generalized Lifting Line Based Code for Wind Turbine Aerodynamics," *49th AIAA Aerospace Sciences Meeting Including the New Horizons Forum and Aerospace Exposition*, AIAA Paper 2011-0146, 2011.
https://doi.org/10.2514/6.2011-146

[60] Lee, J., "A Potential Based Panel Method for the Analysis of Marine Propellers in Steady Flow," Ph.D. Dissertation, Massachusetts Inst. of Technology, Cambridge, MA, 1987.

[61] Kandil, O., Mook, D., and Nayfeh, A., "Nonlinear Prediction of Aerodynamic Loads on Lifting Surfaces," *Journal of Aircraft*, Vol. 13, No. 1, 1976, pp. 22–28.
https://doi.org/10.2514/3.58625

[62] Simpson, R., Palacios, R., and Murua, J., "Induced-Drag Calculations in the Unsteady Vortex Lattice Method," *AIAA Journal*, Vol. 51, No. 7, 2013, pp. 1775–1779.
https://doi.org/10.2514/1.j052136

[63] Willis, D., Peraire, J., and White, J., "A Combined pFFT-Multipole Tree Code, Unsteady Panel Method with Vortex Particle Wakes," *International Journal for Numerical Methods in Fluids*, Vol. 53, No. 8, 2007, pp. 1399–1422.
https://doi.org/10.2514/6.2005-854

[64] Xia, X., and Mohseni, K., "Unsteady Aerodynamics and Vortex-Sheet Formation of a Two-Dimensional Airfoil," *Journal of Fluid Mechanics*, Vol. 830, Nov. 2017, pp. 439–478.
https://doi.org/10.1017/jfm.2017.513

[65] Gebhardt, C., Steinbach, M., and Rolfes, R., "Understanding the Nonlinear Dynamics of Beam Structures: A Principal Geodesic Analysis Approach," *Thin-Walled Structures*, Vol. 140, July 2019, pp. 357–372.
https://doi.org/10.1016/j.tws.2019.03.009

[66] Hente, C., Gebhardt, C., Pache, D., and Rolfes, R., "On the Modal Analysis of Nonlinear Beam and Shell Structures with Singular Mass and Stiffness Matrices," *Thin-Walled Structures*, Vol. 144, Nov. 2019, Paper 106310.
https://doi.org/10.1016/j.tws.2019.106310

[67] Hente, C., Gebhardt, C., and Rolfes, R., "On the Static Analysis of Nonlinear Beam and Shell Structures with Singular Stiffness Matrices Due to Redundant Coordinates," *Thin-Walled Structures*, Vol. 161,

April 2021, Paper 107496.
https://doi.org/10.1016/j.tws.2021.107496

[68] Betsch, P., and Steinmann, P., "Frame-Indifferent Beam Finite Elements Based Upon the Geometrically Exact Beam Theory," *International Journal for Numerical Methods in Engineering*, Vol. 54, No. 12, 2002, pp. 1775–1788.
https://doi.org/10.1002/nme.487

[69] Eugster, S., Hesch, C., Betsch, P., and Glockner, C., "Director-Based Beam Finite Elements Relying on the Geometrically Exact Beam Theory Formulated in Skew Coordinates," *International Journal for Numerical Methods in Engineering*, Vol. 97, No. 2, 2013, pp. 111–129.
https://doi.org/10.1002/nme.4586

[70] Romero, I., and Armero, F., "An Objective Finite Element Approximation of the Kinematics of Geometrically Exact Rods and Its Use in the Formulation of an Energy-Momentum Conserving Scheme in Dynamics," *International Journal for Numerical Methods in Engineering*, Vol. 54, No. 12, 2002, pp. 1683–1716.
https://doi.org/10.1002/nme.486

[71] Betsch, P., and Leyendecker, S., "The Discrete Null Space Method for the Energy Consistent Integration of Constrained Mechanical Systems. Part II: Multibody Dynamics," *International Journal for Numerical Methods in Engineering*, Vol. 67, No. 4, 2006, pp. 499–552.
https://doi.org/10.1002/nme.1639

[72] Fung, Y., *An Introduction to the Theory of Aeroelasticity*, Dover, New York, 1955, pp. 235–245.

[73] Avin, O., Raveh, D., Drachinsky, A., Ben-Shmuel, Y., and Tur, M., "Experimental Aeroelastic Benchmark of a Very Flexible Wing," *AIAA Journal*, Vol. 60, No. 3, 2022, pp. 1–24.
https://doi.org/10.2514/1.j060621

[74] Fehrs, M., Ritter, M., Helm, S., and Mertens, C., "CFD Simulations of the PAZY Wing in Support of the Third Aeroelastic Prediction Workshop," AIAA Paper 2024-0419, 2022.
https://doi.org/10.2514/6.2024-0419

[75] Stanford, B., Chwalowski, P., and Jacobson, K., "Aeroelastic Analysis of Highly Flexible Wings with Linearized Frequency Domain Aerodynamics," American Inst. of Aeronautics and Astronautics, San Diego, CA, 2022.
https://doi.org/10.2514/6.2022-2188.vid

[76] Ritter, M., Hilger, J., Ribeiro, A., Öngüt, A. E., Righi, M., Raveh, D. E., Drachinsky, A., Riso, C., Cesnik, C. E., Stanford, B., et al., "Collaborative Pazy Wing Analyses for the Third Aeroelastic Prediction Workshop," AIAA Paper 2024-0419, 2024.
https://doi.org/10.2514/6.2024-0419

[77] Weisshaar, T., *Aeroelasticity–A One Semester Course*, Independently Published, 2022.

[78] Gebhardt, C., Schillinger, D., Steinbach, M., and Rolfes, R., "A Framework for Data-Driven Structural Analysis in General Elasticity Based on Nonlinear Optimization: The Static Case," *Computer Methods in Applied Mechanics and Engineering*, Vol. 365, June 2020, Paper 112993.
https://doi.org/10.1016/j.cma.2020.112993

[79] van Garrel, A., Venner, C., and Hoeijmakers, H. W., "Fast Multilevel Panel Method for Wind Turbine Rotor Flow Simulations," AIAA Paper 2017-2001, 2017.
https://doi.org/10.2514/6.2017-2001

[80] Deng, S., Jiang, C., Wang, Y., and Wang, H., "Acceleration of Unsteady Vortex Lattice Method via Dipole Panel Fast Multipole Method," *Chinese Journal of Aeronautics*, Vol. 34, No. 2, 2021, pp. 265–278.
https://doi.org/10.1016/j.cja.2020.06.029

S. Ricci
Associate Editor